Lehrstuhl für elektrische Antriebssysteme und Leistungselektronik
der Technischen Universität München

Model Predictive Torque Control for Electrical Drive Systems with and without an Encoder

Fengxiang Wang

Vollstaendiger Abdruck der von der Fakultät für Elektrotechnik und Informationstechnik der Technischen Universität München zur erlangung des Grades eines

Doktor-Ingenieur

genehmigten Dissertation.

Vorsitzender: Univ.-Prof. Dr.-Ing. Hans-Georg Herzog
Prüfer der Dissertation:
1. Univ.-Prof. Dr.-Ing. Ralph Kennel
2. Prof. Dr.-Ing. José Rodríguez Pérez,
Universidad Técnica Federico Santa Maria,
Valparaiso, Chile

Die Dissertation wurde am 19.03.2014 bei der Technischen Universität München eingereicht und durch die Fakultät für Elektrotechnik und Informationstechnik am 15.07.2014 angenommen.

Acknowledgement

This dissertation is to my wife Mrs. Huiling Du and my parents Mr. Zhonghua Wang and Mrs. Deyuan Zhang.

The work in this dissertation is based on research carried out at the Institute for Electrical Drive Systems and Power Electronics, Technische Universität München (TUM) supervised by Prof.-Ing. Ralph Kennel. No part of this dissertation has been submitted elsewhere for any other degree or qualification and it is all my own work unless referenced to the contrary in the text.

My deepest gratitude goes first and foremost to Prof.-Ing. Ralph Kennel, my supervisor, for his constant encouragement and guidance. He has walked me through all the stages of the work of my Ph.D project. I have ever met a lot of problems in laboratory. I had many experiences of failure. Fortunately, Prof. Kennel can alway keep a positive attitude on my work, which gives me great encouragement. Without his consistent and illuminating instruction, this dissertation could not have reached its present form.

I would like to express my heartfelt gratitude to Prof.-Ing. José Rodríguez. He is the specialist in the filed of power electronics and electrical drives. I am very lucky to cooperate with him during my PhD study. Under his supervision, as a result of our cooperation, we have already had two papers accepted by IEEE transactions on Industrial Electronics and on Industrial Informatics, respectively. Furthermore, we still have over 3 papers under review in some prestigious journal in our field. Remarkable is the fact that Prof. José Rodríguez works in Valparaiso, Chile. The distance has not been a problem for the joint work. I sincerely hope that his supervision can be with me for my whole life.

I am also greatly indebted to my colleagues. Peter Stolze is a very important partner in my research life in TUM. He helped me a lot on my research work, especially at the stage of the beginning. Without his kind cooperation I am afraid that I cannot complete my dissertation now. Alireza Davari has ever worked with me on my test bench and we published my 1st Journal paper, which is a very good

start of my research. Jean-Francois Stumper and Dirk Paulus have also helped me on my work. I also appreciate the co-work from Esteban Fuentes, Peter Landsmann, Reza Fotouhi and all my colleagues in EAL, TU Muenchen.

I would like to highly appreciate the cooperation work from the Chinese group in our laboratory. They are Jianbo Gao, Zhixun Ma, Zhenbin Zhang, Zhe Chen, Xiaocan Wang, Wei Xie, Guangye Si and Xuezhu Mei. Dr. Gao is a very nice man, who has given much support to all young PhD students. With his support, our young group have grown in research quickly. Zhenbin Zhang works with the topic of wind turbin technology. From the cooperation with him, I have learnt a lot from this subject, which is highly valuable. Zhe Chen works for sensorless control by using high-frequency injection method. We have co-authored two journal papers up to now. Xiaocan Wang and Wei Xie provide me also a lot of support both in work and in life. We are going to keep a long cooperation in our research life and aim to achieve more and more good results.

I acknowledge that all of my colleagues play important role during my Phd work and study. Without their supervision or cooperation, the dissertation cannot reach its present form.

Contents

CHAPTER 1

Introduction

The electric motor converts electrical energy to mechanical energy. The motors play a very essential role in industries. Manufacturing lines in industries typically require one or more than one variable speed motor drives which serve to power conveyor belts, robot arms, overhead cranes, steel process lines, paper mills and plastic and fiber processing lines, etc. [1].

1.1 DC and AC motors

Generally, electric motors could be classified into two categories: direct current (DC) motors and alternating current (AC) motors [2]. AC motors include induction motors and synchronous motors. In a DC motor, a mechanical commutator reverses the direction of the current flow in the armature coils whenever the pertinent conductors change position from one stator pole pitch to the other. Therefore, the commutator acts as a mechanical converter that arranges the magnetic axis of filed winding in quadrature with the armature winding. A DC motor has separate filed and armature windings. Thus, electromagnetic torque and flux can be controlled independently by the field and armature currents. However, a DC motor has two major disadvantages, the mechanical commutator and brush assembly. The presence of the commutator makes the speed of the DC motor inherently limited. The size and the weight of a DC motor are also large mainly because of the commutator. An induction motor (IM) is an asynchronous AC motor where power is transferred to the rotor by electromagnetic induction, much like transformer action. An induction motor resembles a rotating transformer, because the stator (stationary

part) is essentially the primary side of the transformer and the rotor (rotating part) is the secondary side. IM has many advantages compared to a DC motor. Neither commutator nor brush exists on squirrel cage induction motors. It means the higher speeds are possible with the equivalent induction machines. The efficiency of induction motors used for variable speed operation are generally comparable and frequently better than the equivalent DC motor efficiency, even though the presence of the rotor cage adds an additional loss component not encountered in a DC motor. Since the induction motor cage does not need to be designed to allow for a direct on line start when driven from a converter, the cage resistance can be selected solely to provide optimum running performance and minimum loss. Also, DC motor losses such as brush drop can be eliminated. An essential part of any economic comparison is the cost of keeping spares as well as the frequency of maintenance. A supply of brushes and brush holders are necessary stock items for DC motors. A DC motor must be regularly taken out of service to check or replace brushes and at less frequent intervals to resurface the commutator. Except for the bearings, an induction motor has low cost for maintenance. An induction machine has always smaller size and less weight than an equivalent DC machine. Prior to 1970s, the use of DC motors was popular since AC motors were not capable of true adjustable or smoothly varying speed [2, 3].

1.2 FOC and DTC control strategies

Field Oriented Control (FOC) was developed in the 1970s [4]. FOC is a technique which provides a method of decoupling the air-gap flux and the other producing the electromagnetic torque [5, 6]. Therefore, it provides independent control of torque and flux, similar to a separately excited DC machine. The magnitude and phase of the stator currents are controlled in such a way that flux and torque components of current remain decoupled during dynamic and static conditions. In FOC, the stator phase currents are transformed into a synchronously rotating reference. Field-orientation is achieved by aligning the rotor flux linkage vector along the d-axis of the reference frame. With this arrangement, the control dynamics of the highly coupled nonlinear structure of the induction machine becomes linearized and decoupled. FOC has been one of the most popular control methods since its introduction. It is also a main method used by Siemens. A main complexity in FOC is that a coordinate transformation is needed, it implies to obtain the angle of the rotor flux, which cannot be directly measured from the machine terminals. Thus, it is necessary to implement an encoder, estimators or observers, which are based on a model of the machine. Unfortunately, these estimations are very sen-

sitive to the parameters of the machine, like the stator resistance or the rotor time constant because they change their properties according to the temperature or the flux level. All these conditions impact on the rotor flux angle computation, thus a proper decoupled control between torque and flux cannot be performed.

Direct Torque Control (DTC) is a control method without a coordinate transformation [7,8]. DTC was published by Blaschke, Takahashi and Noguchi in the1970s and 1980s, respectively. The innovation led to a replacement of the linear PI controller by faster hysteresis controllers. DTC offers an excellent torque response using a less parameter sensitive model than FOC. Since its introduction, DTC have been used widely because of its simplicity and very fast torque and flux control response for high performance drive applications. DTC is a main control strategy used by ABB.

The standard DTC method [1] has a drawback: torque ripples are considerable. Many modified DTC schemes have been researched in order to reduce the ripples. In [9] the method minimizes the rms value of the torque ripple but has an unnecessary high switching frequency. Direct mean torque control (DMTC) was developed to maintain the torque within hysteresis limits and reached a constant switching frequency [10, 11]. Band-constrained technique for DTC was proposed in [12] and was verified to be a good approach. This method reduces the torque ripple while maintaing the structure of the standard scheme. The sliding mode control technique was used into DTC system [13]. The space vector modulation (SVM) based DTC was approved to be a useful solution [14–16]. These methods can abate the torque ripple successfully. However, they either increase the complexity of the standard DTC scheme or increase the switching frequencies. Recently, the reasons of the big ripples of the standard DTC were analyzed again and a time delay compensated DTC was verified effectively to lower ripples [17].

1.3 Model predictive control

Model Predictive Control (MPC) is an alternative control strategy. The basic idea of MPC is to pre-calculate the optimum values for the actuating variables based on a mathematical model of the system, the history of past control actions and an optimization of a cost function over a receding prediction horizon [18]. MPC has many advantages: the basic concept is easy to understand, the algorithm is simple to implement, it can handle multi-variable systems and constraints can be included. The main disadvantage of MPC is the big online calculation effort, especially with long horizons [19]. Since the 1970s it has been used in some slow dynamic applications such as petrochemical industry, where fast sampling frequencies are not

required [20]. Fortunately, the use of digital signal processing (DSP) and the development of Field Programmable Gate Arrays (FPGAs) have made it possible to use MPC in fast dynamic process industries such as power electronics and control of electrical drives [21–24]. MPC was introduced into the field of power electronics and electrical drives in the 1980s [25, 26].

1.4 Encoderless strategies

Encoderless strategies have been widely investigated. The absence of a speed encoder reduces the cost of the system and possibly improves the reliablity by removing the noise which injected by the cables, as well as lower the complex of the system [27]. Encoderless control of electrical drives has been achieved by various use of state observation techniques. A state observer is a real time model of a real process or system, which produces an approximation of the state vector of that system, and whose characteristics are somewhat free to be determined by the designer [28]. The state estimation for drives includes two categories: observers based on the models and observers based on high-frequency injection which use the anisotropic properties of the machine [29]. Unfortunately, the high-frequency injection methods require normally a modulator, which makes it not flexible for some direct control methods, i.e., DTC method. Model based observers have been developed widely and they have showen good accuracy and high relibilities. The model based methods include Luenberger observer [30], model reference adaptive system (MRAS) [31], kalman filters [32], sliding mode observer (SMO) [33], etc.

1.5 Main work of this thesis

By investigating widely the predictive control strategies in the field of electrical drives, the thesis concentrates on the application of the FCS-PTC method. The FCS-PTC method is carried out experimentally and analyzed both for IM amd for IPMSM by using a two-level voltage inverter. Different prediction horizons are considered by considering lower calculation time and lower switching frequency.

Furthermore, the FCS-PTC method is adapted to different encoderless strategies, i.e., MRAS and SMO. In PTC, not only an accurate estimated rotor speed is required, but also the fluxes in good quality are essential. Therefore, the observer must be sometimes compensated for qualified fluxes estimation. To find out a more comparable PTC method, an inherently encoderless PTC is proposed, with which the PTC method has same merit with DTC which is inherently encoderless controller.

Therefore, based on a two-level voltage source inverter, an encoder based and an encoderless FCS-PTC methods for electrical drive systems are the main interest of this thesis. All proposals are verified experimentally in this work.

CHAPTER 2

Models of AC motors and converter

2.1 Three-phase current system

To understand the operation of motor control, it is necessary to describe the three-phase current system. In power system, a three-phase current system can be represented by a three-axis coordinate system as it is shown in Fig 2.1(a) presenting a three-phase current system in a three-axis coordinate. This three-phase system can be depicted by using a complex reference frame. In Fig 2.1(b) an equivalent representation of the states fixed system is presented.

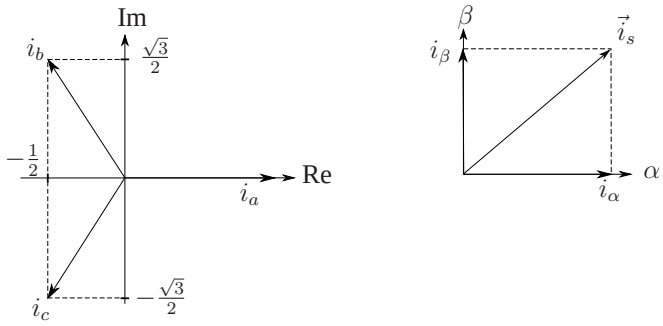

(a) Current System in a three-axis coordinate (a,b,c)

(b) Current system in a complex reference frame $\alpha\beta$

Figure 2.1: Coordinates transformation

A three-phase current system with angular frequency w_0 can be defined in a fixed

three-phase coordinate frame:

$$i_a = I \cdot sin(w_0 \cdot t) \tag{2.1}$$

$$i_b = I \cdot sin\left(w_0 \cdot t + \frac{2\pi}{3}\right) \tag{2.2}$$

$$i_c = I \cdot sin\left(w_0 \cdot t + \frac{4\pi}{3}\right) \tag{2.3}$$

The transformation from a three to two-phase system is described in the equations 2.4 to 2.6:

$$\boldsymbol{i}_s = i_a + a \cdot i_b + a^2 \cdot i_c \tag{2.4}$$

$$a = e^{j \cdot \frac{2 \cdot \pi}{3}} = \frac{-1}{2} + j \cdot \frac{\sqrt{3}}{2} \tag{2.5}$$

$$a^2 = e^{j \cdot \frac{4 \cdot \pi}{3}} = \frac{-1}{2} - j \cdot \frac{\sqrt{3}}{2} \tag{2.6}$$

The same vector $\boldsymbol{i}_s$ can be expressed in terms of complex coordinates by using the Clarke transformation:

$$\boldsymbol{i}_s = i_\alpha + j \cdot i_\beta \tag{2.7}$$

$$i_\alpha = \frac{2}{3} \cdot \left(i_a - \frac{1}{2} \cdot i_b - \frac{1}{2} \cdot i_c\right) \tag{2.8}$$

$$i_\beta = \frac{2}{3} \cdot \left(\frac{\sqrt{3}}{2} \cdot i_b - \frac{\sqrt{3}}{2} \cdot i_c\right) \tag{2.9}$$

The subindex α and β denotes the use of a complex reference frame. In matrix form, equations 2.8 and 2.9 can be rewritten as:

$$\begin{bmatrix} i_\alpha \\ i_\beta \end{bmatrix} = \frac{2}{3} \cdot \begin{bmatrix} 1 & -\frac{1}{2} & -\frac{1}{2} \\ 0 & \frac{\sqrt{3}}{2} & -\frac{\sqrt{3}}{2} \end{bmatrix} \cdot \begin{bmatrix} i_a \\ i_b \\ i_c \end{bmatrix} \tag{2.10}$$

When the system in $\alpha\beta$ coordinate needed to be transformed to rotating dq coordinate, the Park transformation is used. Assuming the dq coordinate rotates with an angle θ against the $\alpha\beta$ system, the realtionship of two coordinate systems are as following:

$$\begin{pmatrix} i_d \\ i_q \end{pmatrix} = \begin{pmatrix} cos(\theta) & sin(\theta) \\ -sin(\theta) & cos(\theta) \end{pmatrix} \begin{pmatrix} i_\alpha \\ i_\beta \end{pmatrix} \tag{2.11}$$

The inverse Park transformation from dq to $\alpha\beta$ coordinate is:

$$\begin{pmatrix} i_\alpha \\ i_\beta \end{pmatrix} = \begin{pmatrix} cos(\theta) & -sin(\theta) \\ sin(\theta) & cos(\theta) \end{pmatrix} \begin{pmatrix} i_d \\ i_q \end{pmatrix} \tag{2.12}$$

2.2 Mathematical model of an IM

An induction machine can be described by a well-known set of complex equations using a stator reference frame [34]:

$$\boldsymbol{v}_s = \boldsymbol{i}_s \cdot R_s + \frac{d}{dt}\boldsymbol{\psi}_s \tag{2.13}$$

$$0 = \boldsymbol{i}_r \cdot R_r + \frac{d}{dt}\boldsymbol{\psi}_r - j \cdot \omega \cdot \boldsymbol{\psi}_r \tag{2.14}$$

$$\boldsymbol{\psi}_s = L_s \cdot \boldsymbol{i}_s + L_m \cdot \boldsymbol{i}_r \tag{2.15}$$

$$\boldsymbol{\psi}_r = L_r \cdot \boldsymbol{i}_r + L_m \cdot \boldsymbol{i}_s \tag{2.16}$$

$$T_e = \frac{3}{2} \cdot p \cdot Im\{\boldsymbol{\psi}_s^* \cdot \boldsymbol{i}_s\}, \tag{2.17}$$

Equation (2.13) is the voltage equation of the phase winding: it describes the relationship of the stator voltage, the stator current and the stator flux linkage of the winding. In equation (2.14) The rotor voltage vector $\boldsymbol{v}_r$ is equal to zero because a squirrel-cage motor is considered. Hence the rotor winding is short circuited. The winding and rotor fluxes can be calculated by using the stator current and the rotor current in equation (2.15) and (2.16), respectively. The electromagnetic torque is proporional to the external product of two state variable space vectors in equation (2.17).

If the mechanical equation of the rotor is considered, it is possible to note that the torque depends on the ratio of change of the mechanical rotor speed ω_m.

$$J\frac{d\omega_m}{dt} = T_e - T_l \tag{2.18}$$

The coefficient J denotes the moment of inertia of the mechanical shaft and T_l is equal to the load torque connected to the machine. It corresponds to an external disturbance, which the control system must be able to compensate. ω_m is the mechanical rotor speed and it is related to the electric rotor speed ω by the number of pole pairs p:

$$\omega = p \cdot \omega_m \tag{2.19}$$

2.3 Mathematical model of a synchronous machine

In synchronous reference frame dq, the stator voltage equation of a synchronous machine can be expressed as following:

$$v_{sd} = R_s i_{sd} + \frac{d\psi_{sd}}{dt} - \omega\psi_{sq}, \tag{2.20}$$

$$v_{sq} = R_s i_{sq} + \frac{d\psi_{sd}}{dt} + \omega\psi_{sd}. \tag{2.21}$$

The total flux is a sum of the mutual flux generated by the stator windings and the permanent magnet rotor flux. The stator flux linkage is described for simplicity in the rotor reference frame by ignoring the leakage inductances and magnetic cross-couplings and given by:

$$\psi_{sd} = L_d i_{sd} + \psi_{PM}, \tag{2.22}$$

$$\psi_{sq} = L_q i_{sq}. \tag{2.23}$$

The torque equation consists of electromagnetic torque and the reluctance torque. It is calculated by:

$$\hat{T} = \frac{3}{2} p\psi_{PM} i_{sq} + \frac{3}{2} p(L_d - L_q) i_{sd} i_{sq}. \tag{2.24}$$

The reluctance torque appears only if the inductances have different values: $L_d \neq L_q$.

To complete the model, the mechanical equation is included:

$$\frac{d\omega}{dt} = \frac{1}{J}(T - T_l). \tag{2.25}$$

where J is the moment of the inertia and T_l is the load torque.

2.4 Two-level voltage source inverter

The power circuit of a two-level voltage source inverter is described in Fig. 2.2(a). The switching states of the converter are decided by the gating fire signals S_a, S_b and S_c. They are presented as follows:

$$S_i = \begin{cases} 1 & \textit{if } S_1 \text{ on and } \bar{S}_1 \text{ off} \\ 0 & \textit{if } S_1 \text{ off and } \bar{S}_1 \text{ on} \end{cases} \tag{2.26}$$

where i = a, b and c.

The switching states can be expressed by the vector as following:

$$\boldsymbol{S} = \frac{2}{3}(S_a + \boldsymbol{a}S_b + \boldsymbol{a}^2 S_c) \tag{2.27}$$

where $\boldsymbol{a} = e^{j2\pi/3}$.

Similar to the described three-phase current system above, the output voltage space vectors genergated by this two-level voltage source inverter are defined by:

$$\boldsymbol{v} = \frac{2}{3}(v_a + \boldsymbol{a}v_b + \boldsymbol{a}^2 v_c) \tag{2.28}$$

where $v_{a,b,c}$ denotes the phase to neutral voltages of the inverter. This voltage vector $\boldsymbol{v}$ is related to the switching state $\boldsymbol{S}$ by

$$\boldsymbol{v} = V_{dc}\boldsymbol{S}. \tag{2.29}$$

Considering all possible combinations of the switching signals $S_{a,b,c}$, there are in total eight reasonable different switching states. These are presented in Fig. 2.2(b). The equivalent of $\boldsymbol{v}_0 = \boldsymbol{v}_7$ results in only seven different voltage vectors.

In this work, the inverter is considered as a nonlinear discrete system with seven different states as possible outputs, because only the direct control methods are focused.

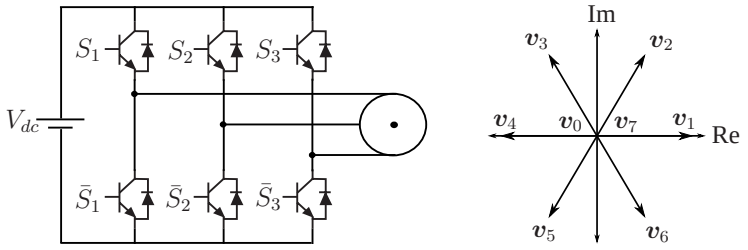

(a) Three-phase two-level inverter

(b) Different voltage vectors generated by a two-level inverter

Figure 2.2: Inverter and voltage vectors

CHAPTER 3

Predictive control in electrical drive systems

3.1 Classification of predictive control

Predictive control is a modern control method which precalculates the plant's behavior by means of a mathematical model and use this information to calculate optimum values for the actuating variables via an optimization criterion [19]. The structure of predictive control is presented in Fig. 3.1. The system estimates the unmeasured variables and feeds them back to the prediction block which includes variables prediction and optimization. The optimum values will be output to the actuator and finally control the plant. The basic idea is common for all kinds of predictive control methods, but the specific optimization criterions are different.

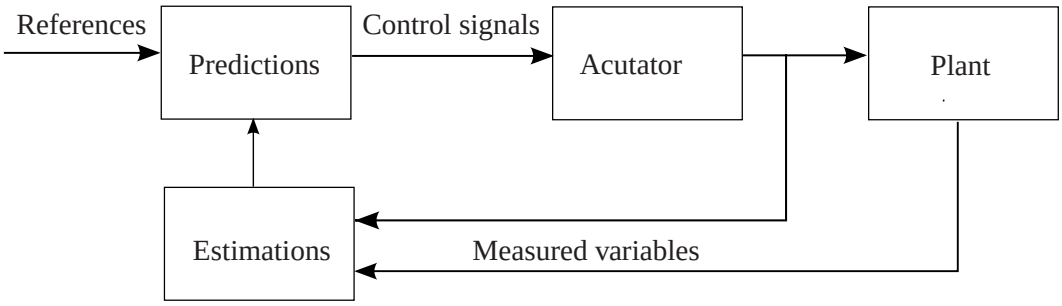

Figure 3.1: Block diagram of predictive control method.

Based on the functional principle, the predictive control can be classified mainly into three categories [35]: hysteresis-based control , trajectory-based control and

model-based predictive control (MPC) which includies continuous MPC and finite control state MPC (FCS-MPC) methods. The classification is presented in Fig. 3.2. The hysteresis-based predictive control is to keep the controlled variable within the predefined boundaries of a hysteresis area. DTC method belongs to the hysteresis-based predictive control. DTC method use torque and stator flux magnitude hysteresis controllers to realize the torque control [7, 8]. Predictive current control proposed in [25] is another example of hysteresis controller. The trajectory-based predictive control forces the variables to follow the predefined trajectory, i.e., direct speed control proposed in [10]. Hysteresis- and trajectory-based predictive controllers are explained clearly in [36]. Both of them do not need modulator and have variable switching frequencies. The absence of the inner current PI controller makes the structures of hysteresis- and trajectory-based predictive control systems simple.

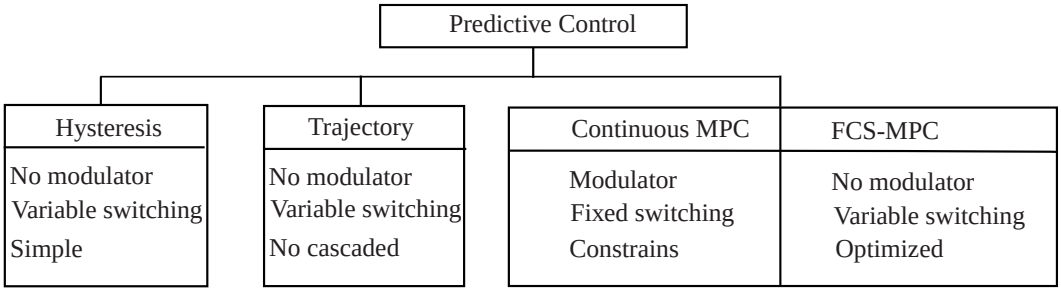

Figure 3.2: Classifications of predictive control.

MPC strategies are different ideas. They are capable to consider the past and to optimize future values of the actuating variables, not only for the next sampling cycle, but up to a specified future cost or control horizon. Comparing the structure of model-based predictive controllers, it can be seen that they are more like state controllers or Kalman filters rather than the hysteresis- and trajectory-based predictive controllers [36]. MPC strategies are also refered to as receding horizon control (RHC). The calculation of the plant behavior up to the prediction horizon N_p needs too much time, which makes it impossible to perform a proper control loop. The calculation complexity can be significantly reduced by the introduction of a control horizon N_u. Only the first set of control actions is applied to the system, in the next sampling instant a new prediction and optimization process is carried out. Fig. 3.3 helps to understand the idea.

Many MPC efforts have been made in the past years, these contributions can be classified into two main categories: continuous MPC and FCS-MPC. In continuous MPC, generalized predictive control (GPC) is a good example. The GPC algo-

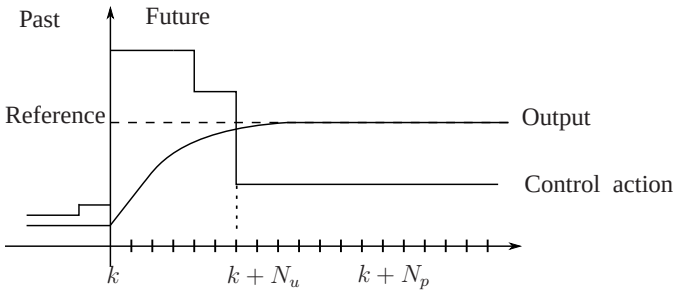

Figure 3.3: Definition of the control and prediction horizon [36].

rithm was proposed in 1987 and became one solution in drives control [37], [38]. In [36], GPC methods are used for electrical drives. The GPC controller uses a so-called CARIMA model which is based on the transfer function of the plant. In the algorithm a Diophantine equation has to be solved. In the work GPC controllers show very good performance. However, the design of GPC is complicated and the concept is not so easy to understand. Furthermore, GPC cannot easily handle constraints and a modulator is required. As another example of continuous MPC, the explicit MPC is presented in [39]. Dead-beat control is also a kind of continuous MPC which needs a modulator. During every sampling interval this approach uses system model to calculate the required reference voltage in order to reach the reference value in the next sampling instant. This voltage is applied via a modulator. The dead-beat contorl are widely investigately [40–44]. All continuous MPC methods need modulators and have constant switching frequencies.

3.2 FCS-Model Predictive Control

Compared to the continuous MPC Methods, FCS-MPC is conceptually simpler [45, 46]. The notable feature of FCS-MPC is that, it does not need a continuous actuating variable and has no modulator [47]. The block diagram of FCS-MPC of motor control considering a single prediction step is described in Fig. 3.4. The algorithm includes three steps: estimations, predictions and optimization. The estimation model calculates the required variables which cannot be directly measured such as fluxes by using the measured motor speed and stator currents. The state variables of the system $\boldsymbol{x}(k)$, including the estimated and measured values, are used as initinal condition for the predictions. The predicted values $\boldsymbol{x}(k+1)$ are evaluated by using a cost function. The switching state $\boldsymbol{S}$ which minimizes the cost function is selected as the gate fire signals of the inverter.

In FCS-MPC the inverter is taken into consideration in the controller design.

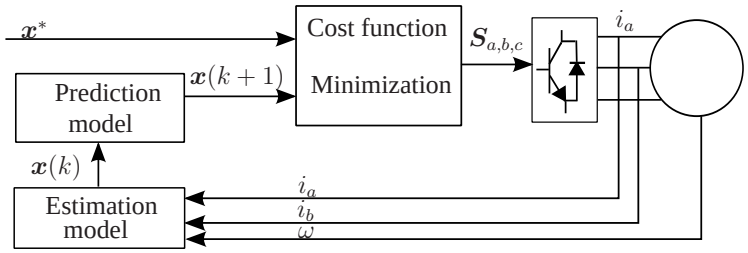

Figure 3.4: The structure of FCS-MPC for motor control.

Every possible inverter switching state is considered for the optimization of a cost function, which normally consists of the errors between references and measured (or estimated) control variables, but can also have additional terms, e.g., over-current protection. Then, the switching state which minimizes the cost function will be selected as the output signal during the next time step [48]. In cost function, to reduce the switching losses, some efforts have been implemented [49, 50]. The weighting factor design in the cost function has also been focused on [51, 52]. The MPC method can also be adapted into the encoderless systems [53–55]. Based on prediction horizons, MPC is classified into one-step and longer prediction horizons schemes [35]. With long prediction horizons, it can be expected to get better performance. However, the corresponding calculation effort will increase exponentially and model errors lead to a worsening of the control variables. On the other hand, one step-prediction FCS-MPC has already been successfully applied to a 2-level voltage source inverter [56], 3-level neutral point-clamped [57], cascaded H-bridge [58], flying capacitor [59, 60], matrix converters [61–63], current source rectifiers [64], modular multilevel converters [65] and multi-phase induction motor drives [66, 67]. MPC has also been applied to renewable energies and power control. For example, in [68] and [69] MPC strategies are applied for photovoltaic arrays and direct power control.

For the FCS-MPC methods with short predictive horizon, the model and the cost function design are very simple and intuitive. Predictive current control (PCC) is introduced in [56]. With an one-step prediction horizon the cost function is defined as:

$$g_j = |i^*_{s\alpha} - \hat{i}_{s\alpha}| + |i^*_{s\beta} - \hat{i}_{s\beta}| \tag{3.1}$$

where j denotes the different voltage vectors. The cost function considers the error between the predicted currents and the reference values. All possible voltage vectors are taken into the calculation of the cost function. The one which minimizes the cost function g_j will be selected as the output.

CHAPTER 4

PTC method for an IPMSM

4.1 Introduction

Due to its high efficiency and high power per volume and weight, permanent magnet synchronous machine (PMSM) has been widely used in drives for electric vehicles and railway vehicles [70]. In these applications, fast torque response is always important. DTC methods are widely investigately for the control of PMSMs. However, the DTC methods have large torque ripples. Though many improved DTC methods can reduce the ripples either by using space vector modulator (SVM) or by direct mean torque control (DMTC), they are on the cost of the system complexity.

MPC methods are applied to PMSMs as new approaches [71, 72]. The investigations show that the control of PMSM by using MPC methods can reduce the torque ripples efficiently while keeping the fast dynamics of the system. In this chapter, an interior PMSM (IPMSM) is tested by using a FCS-MPC method: Predictive Torque Control (PTC). The design of the PTC method of IPMSM is introduced and the method is carried out experimentally.

4.2 Predictive torque control

The block diagram of MPTC method is described in Fig. 4.1. A PTC method for IPMSM includes mainly three steps: torque estimation, torque and current prediction and the cost function design. An external speed PI controller is required to realize the adjustable speed drives. The system does not need a modulator. The switching state which minimizes the cost function will be selected as the gate sig-

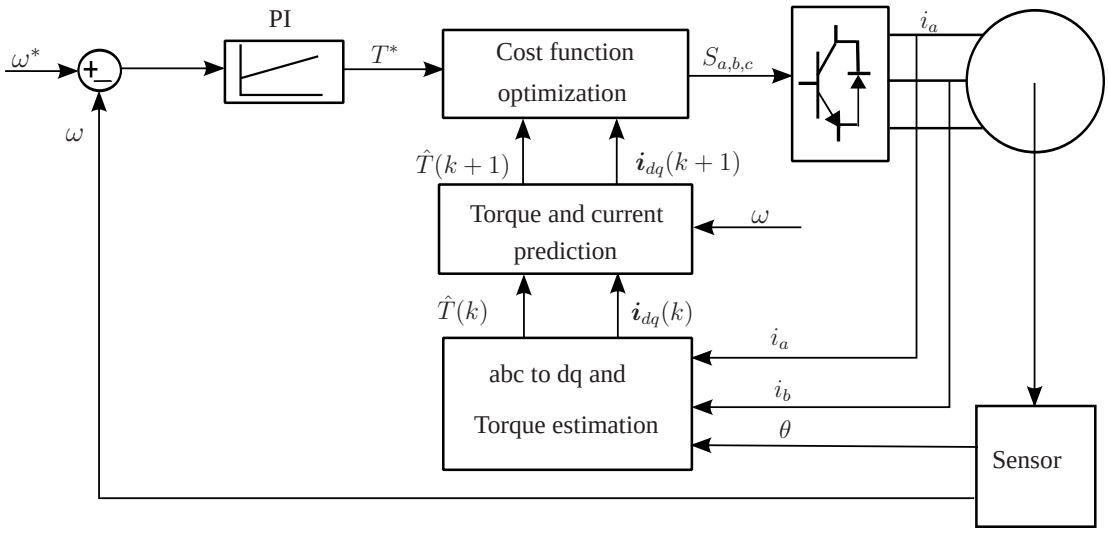

Figure 4.1: Block diagram of Predictive Torque Control of an IPMSM.

nals of the inverter.

4.2.1 Torque estimation and prediction model

The design of the PTC system of IPMSM is developed in synchornous reference frame. With the measured current values, the required dq values can be transformed by using Park transformation introduced in Chapter 2. The continuous-time dq stator currents $\boldsymbol{i}_{s,dq}$ are presented as follows:

$$\frac{di_{sd}}{dt} = -\frac{R_s}{L_d} i_{sd} + \frac{L_q}{L_d}\omega i_{sq} + \frac{1}{L_d} v_{sd}, \tag{4.1}$$

$$\frac{di_{sq}}{dt} = -\frac{R_s}{L_q} i_{sq} - \frac{L_d}{L_q}\omega i_{sd} - \omega\psi_{PM} + \frac{1}{L_q} v_{sq}. \tag{4.2}$$

The torque is not measured by using a torque sensor. Here, the torque is estimated by using the following equation:

$$\hat{T} = \frac{3}{2} p\psi_{PM} i_{sq} + \frac{3}{2} p(L_d - L_q) i_{sd} i_{sq}. \tag{4.3}$$

From the equation, it is easy to see the torque $\hat{T}$ can be calculated by using the $\boldsymbol{i}_{s,dq}$ and the costant IPMSM parameters.

An important step for PTC method is to predict the future value of the required signals. In this work, the predicted stator currents and the torque in the next step are essential. By using the Euler forward equation:

$$\frac{dx}{dt} \approx \frac{x(k+1) - x(k)}{T_s}. \tag{4.4}$$

The stator current and torque continuous-time model can be obtained as follows:

$$\frac{i_{sd}(k+1) - i_{sd}(k)}{T_s} = -\frac{R_s}{L_d} i_{sd}(k) + \frac{L_q}{L_d} \omega i_{sq}(k) + \frac{1}{L_d} v_{sd}(k+1), \tag{4.5}$$

$$\frac{i_{sq}(k+1) - i_{sq}(k)}{T_s} = -\frac{R_s}{L_q} i_{sq}(k) - \frac{L_d}{L_q} \omega i_{sd}(k) - \omega \psi_{PM} + \frac{1}{L_q} v_{sq}(k+1), \tag{4.6}$$

$$\hat{T}(k+1) = \frac{3}{2} p \psi_{PM} i_{sq}(k+1) + \frac{3}{2} p (L_d - L_q) i_{sd}(k+1) i_{sq}(k+1). \tag{4.7}$$

4.2.2 Cost function design

The core of the PTC method is to design a cost function for select the optimum actuating signals. The main goal of this work is to realize the torque control by considering the minimization of the torque error between the predicted torque and the reference value. Therefore, the cost of this error is:

$$T_{err} = (\hat{T}(k+1) - T^*)^2. \tag{4.8}$$

In this equation, the torque reference T^* is generated by a speed PI controller:

$$T^* = k_p \cdot (\omega^* - \hat{\omega}) + k_i \int (\omega^* - \hat{\omega}) dt, \tag{4.9}$$

where k_p and k_i are PI controllers gains.

A maximum torque per ampere (MTPA) criteria is considered to have a low absolute current since high currents lead to large losses [49, 50].

$$C_{MTPA} = (i_{sd}(k+1) + \frac{L_d - L_q}{\psi_{PM}} (i_{sd}^2(k+1) - i_{sq}^2(k+1)))^2. \tag{4.10}$$

An merit of the MPC method is to include the system constrains easily in the cost function. In this work, an over-current protection is considered to achieve a safe system.

$$I_m(k+1) = \begin{cases} 0 & \textit{if } |i(k+1)| \leq |i_{\max}|, \\ \gamma >> 0 & \textit{if } |i(k+1)| > |i_{\max}|. \end{cases} \tag{4.11}$$

where $|i(k+1)| = \sqrt{i_d^2(k+1) + i_q^2(k+1)}$. The vectors who generate the stator current bigger than the limition will never been selected as output. Hence the overcurrent phenomenon can be avoided and a safe system can be easily designed.

By considering equation 4.8 to 4.11, a final cost function of PTC method of an IMPSM is obtained:

$$g_j = (\hat{T}(k+1) - T^*)^2 + (i_{sd}(k+1) + \frac{L_d - L_q}{\psi_{PM}}(i_{sd}^2(k+1) - i_{sq}^2(k+1)))^2 + I_m(k+1)_j, \tag{4.12}$$

where j denotes all possible voltage vectors. Because a two-level voltage source inverter is used in the test, the value of j is $j = 1, 2, ..., 7$. is the coefficient of the cost function.

4.2.3 Time delay compensation

In an ideal simulation, the speed and stator current measurements are taken at the discrete instant k, and at the same time the optimum voltage vector $\vec{v}_s(k)$ is applied to the machine. However, in a real implementation the microprocessor needs time to execute the algorithm. It takes one sampling cycle to generate the optimum switching state if the variables are measured at time k. Hence, the optimum actuating variables are given to the inverter at the time step $k+1$, and not at step k as in a simulation.

To compensate this time delay, a compensation scheme is considered and described in Fig. 4.3. The previous voltage vector is used for a first prediction, then the current voltage vector $\vec{v}_s(k)$ is used to predict the stator flux and torque at time $k+1$. According to these values the controller selects the proper vector which will be applied at time $k+1$ in order to optimize the reference tracking criterion at time $k+2$. In this way the control strategy is time-consistent.

In the cost function, the problem can be solved by modifying the optimization step as following:

$$g_j = (\hat{T}(k+2) - T^*)^2 + (i_{sd}(k+2) + \frac{L_d - L_q}{\psi_{PM}}(i_{sd}^2(k+2) - i_{sq}^2(k+2)))^2 + I_m(k+2)_j, \tag{4.13}$$

Finally, the algorithm of PTC of IPMSM is described in Algorithm 1.

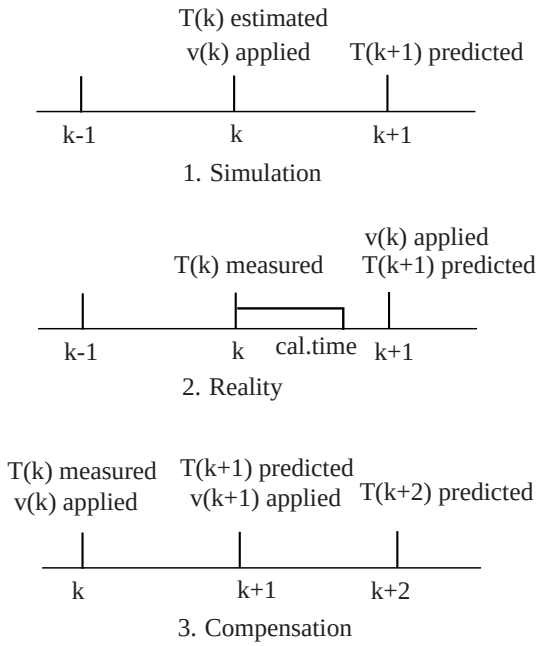

Figure 4.2: Time delay compensation.

4.3 Experimental results

The performance of the PTC method is experimentally investigated with an IPMSM. The test bench in described in Appendix. The sampling time is set to 40 μs. Thus, the system has a 25 kHz samling frequency. The observered calculation time of the algorithm is 12.1 μs. The samling interval is long enough to complete the calculation of the algorithm of this PTC method.

First test is to show the peformance with and without time delay compensation. In this test, the torque ripple is observered. From Fig. 4.3 it can be seen that with time delay compensation method the torque ripple is much lower than that without compensation. In this work, the performance both in stead and in transient states are observered. One test is developed to observe the behavior in steady state. The motor rotates at rated speed with a 70 $\%$ rated load (1.4 Nm). The results of the torque and the stator current are presented in Fig. 4.4. From the picture, it can be concluded that the motor works well with a small torque ripple. The ripple band is less than 0.2 Nm. Also, the system has a good stator current as shown in the picture.

The other test is to observer the system performance in the whole speed range. The speed reference changes from negative rated value to positive rate value while a 70 $\%$ rated load is alway added to the drive motor. The speed, torque and the stator

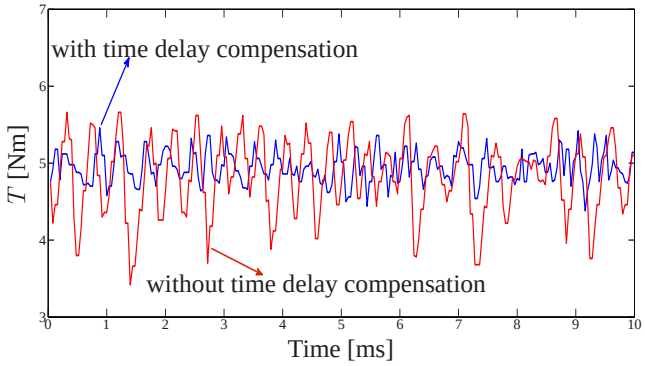

Figure 4.3: Torque response with and without time delay compensation.

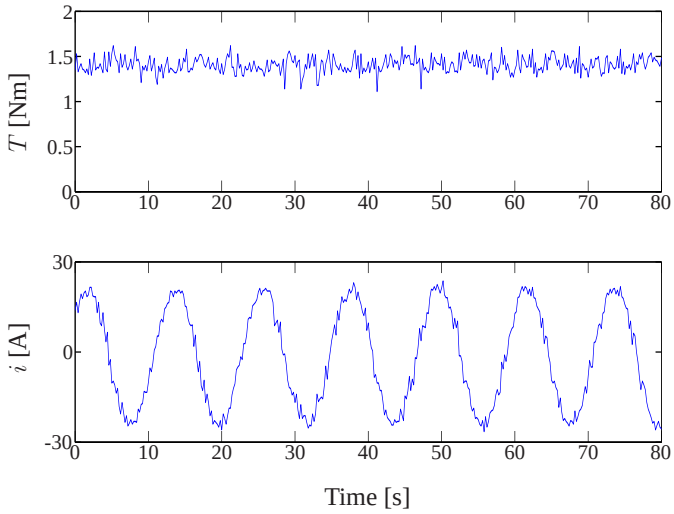

Figure 4.4: Torque and stator current waveforms in steady state.

Algorithm 1 The execution of the MPTC algroithm of an IPMSM

1: Initialize the system and build an array of 7 different voltage vectors.
2: Measurement of ω and $\boldsymbol{i}_s$.
3: Estimations of $\hat{T}(k)$ and $\hat{\boldsymbol{i}}_{s,dq}(k)$.
4: Delay compensation of $\hat{T}(k+1)$ and $\hat{\boldsymbol{i}}_{s,dq}(k+1)$.
5: Predictions of $\hat{T}(k+2)$ and $\hat{\boldsymbol{i}}_{s,dq}(k+2)$.
6: **for** $i = 1, 2, 3, ..., 7$ **do**
7: $g_j = (\hat{T}(k+2) - T^*)^2 + (i_{sd}(k+2) + \frac{L_d - L_q}{\psi_{PM}}(i_{sd}^2(k+2) - i_{sq}^2(k+2)))^2 + I_m(k+2)_j$.
The minimum value of g_j and the coressponding switching vector $\boldsymbol{v}_i$ are kept.
8: **end for**
9: $\boldsymbol{v}_i$ is injected into the inverter.

current are described in Fig. 4.5. The PTC system works well in the whole speed range with a big load. During the transient process, The stator current is limited by the over-current protection term in the cost function. The peak value is less than the i_{m} (40 A).

4.4 Conclusion

In this chapter, PTC method is tested on an IPMSM. The stator currents are directly measured from a current sensor. The transformation synchronous angle can also be read via an encoder. The system design is very simple. By using an Euler forward equation, the next step value of the current and the torque are predicted. Finally, a cost function considering the torque error, MTPA criteria and an over-current protection is developed.

The experimental results show that the system works well both in steady state and in transient state with a big load. The PTC method generates a very small torque ripple, which is an important feature for the drive control. Meanwhile, the system has very fast dynamics and the constraints are easily included. The cost function is very flexible. A switching frequency cost can also be added in the cost function to control the switching commutations.

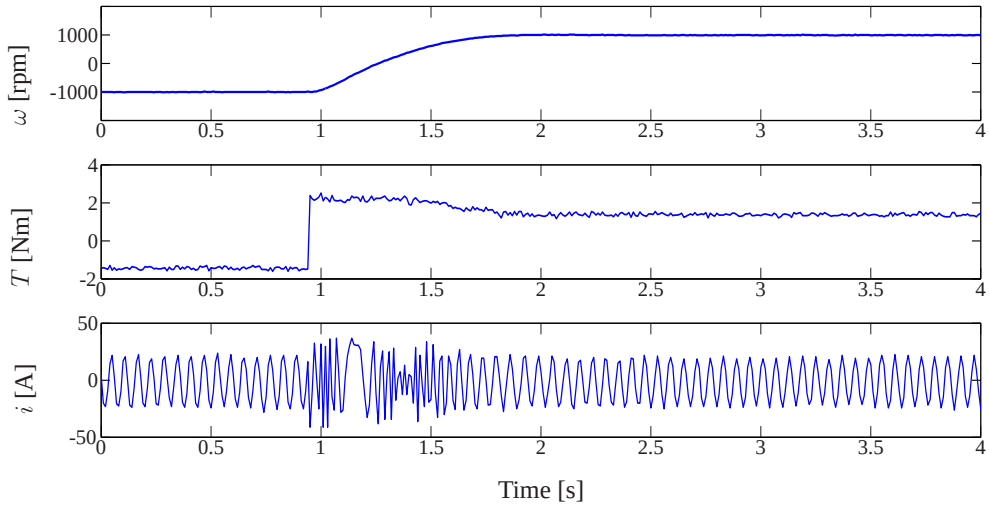

Figure 4.5: Speed, torque and stator current waveforms of PTC during a speed reversal maneuver.

CHAPTER 5

PTC method for IM: an evaluation with DTC

5.1 Introduction

DTC and PTC methods have many features in common. Both strategies have neither inner current PI controller nor modulator. They are direct control methods. However, they are conceptually different. DTC method is a hysteresis control method. A torque hysteresis controller and a flux hysteresis controller are considered in DTC method to limit the torque and flux magnitude within the hysteresis bands. The system selects the output by means of a pre-defined look-up table [1]. PTC method predicts the torque and flux in advance. The inverter model is considered in the contorller. A cost function is defined by considering the torque and flux errors between the references and the predicted values. All possible switching states are taken into the calculation. The one which minimizes the cost function will be selected as the output.

In this chapter, the DTC method and the PTC method are comprehensively compared based on the concept understanding and the experimental implementations. The aim is to evaluate the advantages and disadvantages of two similar but different direct control strategies.

5.2 Direct torque control

The main idea of DTC is to use hysteresis controllers for both stator flux and electromagnetic torque. With the output of the hysteresis controllers, the inverter switching state can be selected from a predefined look-up table [1, 17]. For DTC there are two

assumptions which must be considered. The first one is to suppose that the rotor speed is high enough to neglect the voltage drop caused by the stator resistance in the stator voltage equation. In this way, it is possible to figure out that the stator flux can be modified by the applied inverter voltage vector during a sampling step as follows:

$$\Delta \boldsymbol{\psi}_s \approx \boldsymbol{v}_s \cdot T_s, \tag{5.1}$$

where T_s is the sampling time.

In DTC the electromagnetic torque can be calculated as:

$$T = \frac{2}{3} \cdot \frac{L_m}{\sigma \cdot L_s \cdot L_r} \cdot p \cdot |\boldsymbol{\psi}_r| \cdot |\boldsymbol{\psi}_s| \cdot sin(\delta), \tag{5.2}$$

where $\sigma = 1 - (L_m^2 / L_s \cdot L_r)$.

In order to calculate the electromagnetic torque, the stator flux, rotor flux and the flux angle must be considered:

$$\boldsymbol{\psi}_r = \frac{k_s}{\sigma \cdot \tau_r \cdot s + 1} \cdot \boldsymbol{\psi}_s, \tag{5.3}$$

where $\tau_r = L_r / R_r$, $k_s = L_m / L_s$.

If (5.3) is observed, the second assumption can be concluded: the rotor flux is slower than the stator flux. Therefore, during one sampling step, the rotor flux can be considered as invariant. In this way the electromagnetic torque can be modified by changing the angle of the stator flux by applying an appropriate voltage vector.

Based on those assumptions, the electromagnetic torque and stator flux magnitude can be controlled independently of each other. The architecture of DTC can be observed in Fig. 5.1. The electromagnetic torque and flux references are compared to the estimated values obtained from a discrete model of the machine. The voltage equation is used to estimate the stator flux, from which the stator flux angle can be obtained. The measured current and the estimated flux are applied to the torque estimation. The error between the torque reference and the estimated torque will be forwarded to the torque hysteresis controllers; the error between the stator flux reference and the estimated flux is given to the flux hysteresis controller. Then, the switching vector of the inverter can be found in a predefined look-up table by taking into account the outputs of the two hysteresis controllers and the stator flux angle. As in every traditional speed control strategy, an external PI-speed controller is considered to achieve zero error at steady state on the speed reference tracking. This control loop generates the torque reference for the hysteresis-based torque controller.

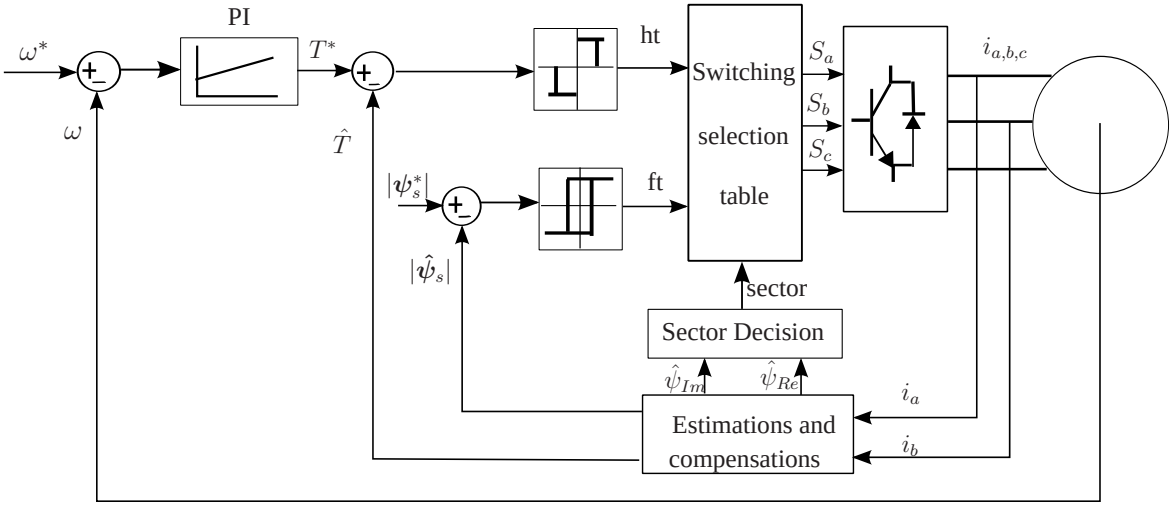

Figure 5.1: Block diagram of Direct Torque Control.

5.3 Predictive torque control

The architecture of PTC is described in Fig. 5.2. The core of PTC is the torque and flux predictions and the design of a cost function. As in DTC, an external speed PI-controller is used to control the speed. Both DTC and PTC use the same flux estimation and electromagnetic torque estimation.

5.3.1 The required signal estimations

Firstly, the rotor and stator fluxes need to be estimated. Based on the squirrel-cage induction machine model presented in chapter 2, the relationship among stator flux, rotor flux, and current can be expressed as:

$$\boldsymbol{\psi}_r + \tau_r \cdot \frac{d\boldsymbol{\psi}_r}{dt} = L_m \cdot \boldsymbol{i}_s \tag{5.4}$$

$$\boldsymbol{\psi}_s = L_m \cdot \left(\frac{\boldsymbol{\psi}_r - L_m \cdot \boldsymbol{i}_s}{L_r} \right) + L_s \cdot \boldsymbol{i}_s \tag{5.5}$$

where $\tau_r = L_r/R_r$.

To discretize (5.5), the Euler backward approximation:

$$\frac{dx}{dt} \approx \frac{x(k) - x(k-1)}{T_s}, \tag{5.6}$$

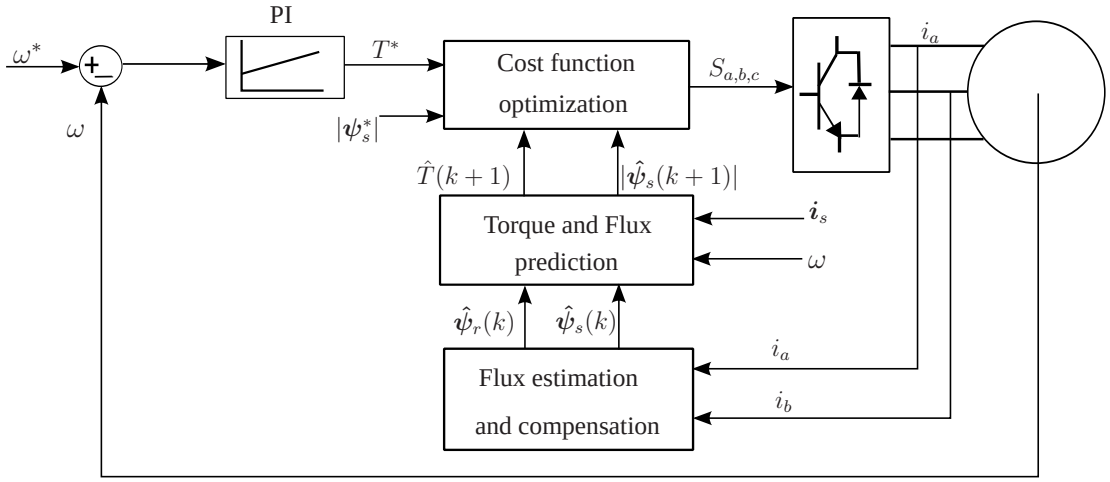

Figure 5.2: Block diagram of Predictive Torque Control.

can be taken into account. Then, the discrete equation for the rotor flux can be written as:

$$\hat{\boldsymbol{\psi}}_r(k) = \frac{L_r}{L_r + T_s \cdot R_r} \cdot \hat{\boldsymbol{\psi}}_r(k-1) + \frac{L_m}{\frac{\tau_r}{T_s} + 1} \cdot \boldsymbol{i}_s(k). \tag{5.7}$$

Substituting (5.7) into (5.5), the discrete stator flux equation can be obtained:

$$\hat{\boldsymbol{\psi}}_s(k) = k_r \cdot \hat{\boldsymbol{\psi}}_r(k) + \sigma \cdot L_s \cdot \boldsymbol{i}_s(k) \tag{5.8}$$

where $k_r = L_m/L_r$ and $\sigma = 1 - (L_m^2/L_s L_r)$.

5.3.2 Stator flux and electromagnetic torque prediction

In the predictive algorithm, the next-step stator flux $\hat{\boldsymbol{\psi}}_s(k+1)$ and the electromagnetic torque $\hat{T}(k+1)$ must be calculated [47]. From the induction machine model described in chapter 2 and [34], the relations between the stator and rotor flux, current, speed and electromagnetic torque can be described as:

$$\frac{d\boldsymbol{\psi}_s}{dt} = \boldsymbol{v}_s - R_s \cdot \boldsymbol{i}_s \tag{5.9}$$

$$\boldsymbol{i}_s = -\frac{1}{R_\sigma}(L_\sigma \cdot \frac{d\boldsymbol{i}_s}{dt} - k_r \cdot (\frac{1}{\tau_r} - j \cdot \omega) \cdot \boldsymbol{\psi}_r) - \boldsymbol{v}_s) \tag{5.10}$$

$$T = \frac{3}{2} \cdot p \cdot Im\{\boldsymbol{\psi}_s^* \cdot \boldsymbol{i}_s\}. \tag{5.11}$$

where $k_r = L_m/L_r$, $R_\sigma = R_s + k_r^2 \cdot R_r$ and $L_\sigma = \sigma \cdot L_s$. To predict the electromagnetic torque and stator flux, the forward Euler discretization is considered:

$$\frac{dx}{dt} \approx \frac{x(k+1) - x(k)}{T_s}. \tag{5.12}$$

The stator flux and current prediction can be obtained as follows [73]:

$$\hat{\boldsymbol{\psi}}_s(k+1) = \hat{\boldsymbol{\psi}}_s(k) + T_s \cdot \boldsymbol{v}_s(k) - R_s \cdot T_s \cdot \boldsymbol{i}_s(k). \tag{5.13}$$

$$\begin{aligned} \hat{\boldsymbol{i}}_s(k+1) = (1 - \tfrac{T_s}{\tau_\sigma}) \cdot \boldsymbol{i}_s(k) + \tfrac{T_s}{\tau_\sigma} \tfrac{1}{R_\sigma} \cdot [k_r \cdot (\tfrac{1}{\tau_r} \\ -j \cdot \omega(k)) \cdot \hat{\boldsymbol{\psi}}_r(k) + \boldsymbol{v}_s(k)], \end{aligned} \tag{5.14}$$

where $\tau_\sigma = \sigma \cdot L_s/R_\sigma$.

With the predicted stator flux and the predicted current, the electromagnetic torque can be predicted:

$$\hat{T}(k+1) = \frac{3}{2} \cdot p \cdot Im\{\hat{\boldsymbol{\psi}}_s(k+1)^* \cdot \hat{\boldsymbol{i}}_s(k+1)\}. \tag{5.15}$$

5.3.3 Cost function

The last step is to develop a proper cost function for the optimization. The cost function is very flexible and can handle a multi-variable problem. It should be designed according to the specific control goals. In this chapter, the cost function includes four components: torque error, stator flux error, switching transitions and current limitation as a constraint. The used cost function is definied as following:

$$\begin{aligned} g_i = |T^* - \hat{T}(k+1)_i| + \lambda_1 \cdot | \parallel \boldsymbol{\psi_s^*} \parallel - \parallel \hat{\boldsymbol{\psi}}_s(k+1)_i \parallel | \\ +\lambda_2 \cdot |S(k) - S(k+1)_i| + I_m(k+1), \end{aligned} \tag{5.16}$$

where i denotes the index of applied voltage vector for the prediction, it is $i = 1...7$.

The torque reference T^* is generated by a speed PI-controller. The coefficient λ denotes the weighting factor, which weights the relative importance of the each term.

The current limitation term is active when the absolute value of the predicted current is higher than its limit. The current limitation is defined as:

$$I_m(k+1) = \begin{cases} 0 & \textit{if } |i(k+1)| \leq |i_{max}|, \\ \gamma >> 0 & \textit{if } |i(k+1)| > |i_{max}|. \end{cases} \tag{5.17}$$

where $|i(k+1)| = \sqrt{i_\alpha^2(k+1) + i_\beta^2(k+1)}$.

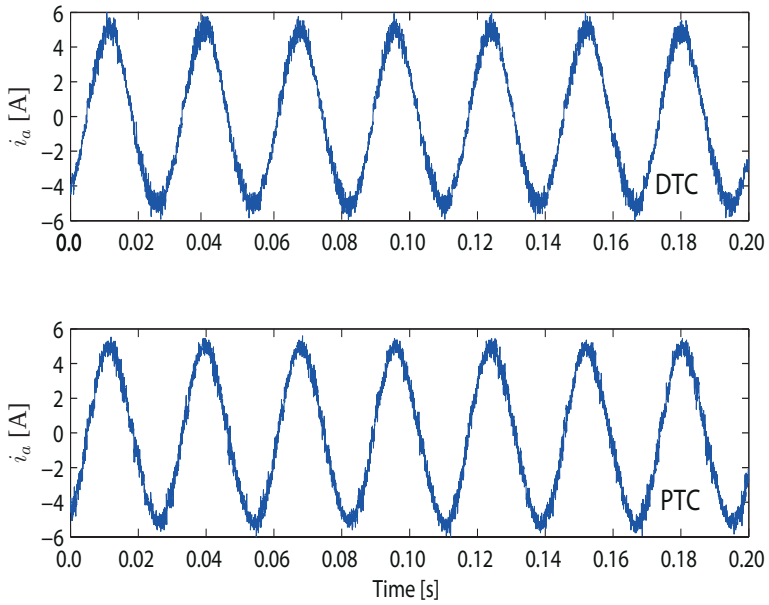

Figure 5.3: Stator current waveform with a half nominal load of DTC and PTC.

5.4 Experimental results

5.4.1 Experimental results and analysis

In order to develop a fair comparison, an equivalent switching frequency for both strategies in steady state should be guaranteed [73]. In order to make the switching frequency of both algorithms equivalent, the average switching frequency of PTC at a specific operation point is taken as a reference. It is possible to get a very similar switching frequency by modifying the bands of the hysteresis controllers in DTC method.

The stator current performance of both algorithms in steady state with a load torque is investigated. Several tests with different operating points are observed and both PTC and DTC have similar behavior. One of these test results is discussed. The speed reference is set to 1500 rpm (half of the nominal speed) and the two algorithms have the same speed PI-controller. The motor rotates with half of the nominal load. In PTC method it has an average IGBT switching frequency (3.5 kHz) at this operating point. To ensure an equivalent average switching frequency in DTC system, the torque hysteresis and flux hysteresis band are configured as 0.57 Nm and 0.005 Wb, respectively. The stator current waveforms are presented in Fig. 5.3. From the picture it can be concluded that both algorithms produce similar

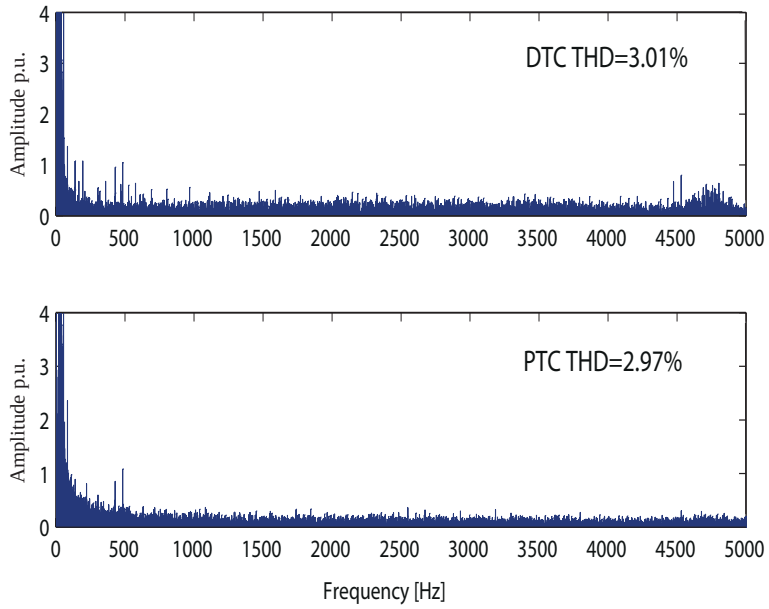

Figure 5.4: Harmonic spectrum of the stator currents of DTC and PTC.

stator currents for the same IGBT switching frequency. To evaluate the distortion of both stator currents, the spectrum and THD (total harmonic distortion) has been calculated and given in Fig. 5.4. It shows that DTC and PTC have very close THD values with 3.01% versus 2.97%.

The second test is designed to show the constant electromagnetic torque and stator flux behaviour. Without a speed PI-controller, the torque reference for both strategies is set to 7.0 Nm, and the stator flux magnitude is set to 0.71 Wb. The load motor is controlled with a closed loop speed control. In this way, the rotational speed is kept constant. In Fig. 5.5 and Fig. 5.6, the behaviours of the torque and flux are presented. It can be seen that the torque ripples of DTC and PTC are very similar and they both have a steady state error. However, since speed control is required in most of the applications, this issue can be easily avoided by just considering an outer speed PI-controller. For stator flux, both strategies also reach similar performance. It is important to point out that in FOC, the inner loop based on current PI-controllers assures zero error at steady state in the torque, that being an important advantage of this strategy.

The third test is to verify the performance of a torque step. The torque step is 7.5 Nm which was generated by a sudden change of the speed reference from 1000 rpm to 2000 rpm. From Fig. 5.7 and Fig. 5.8 it can be observed that both DTC and PTC can track the torque changes and show very fast dynamics. The uprising time

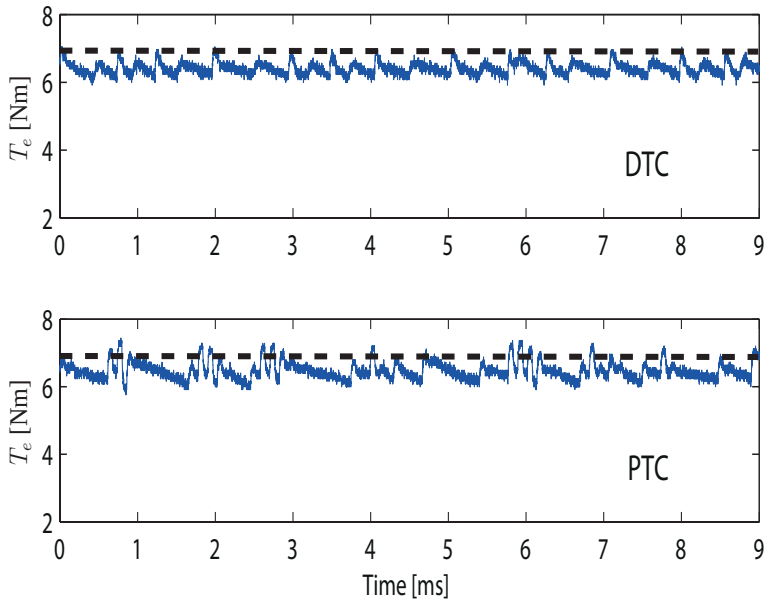

Figure 5.5: Torque behaviour at constant reference of 7 Nm of DTC and PTC.

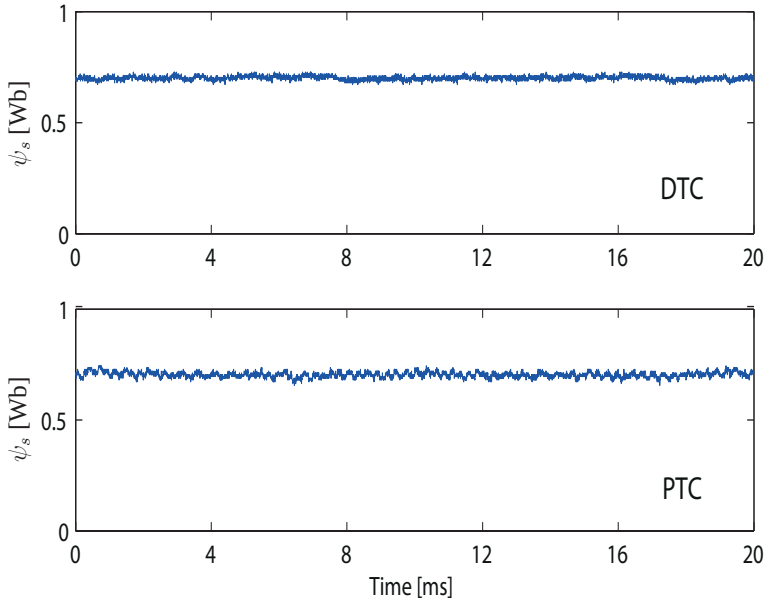

Figure 5.6: Stator flux behaviour at constant reference of 0.71 Wb of DTC and PTC.

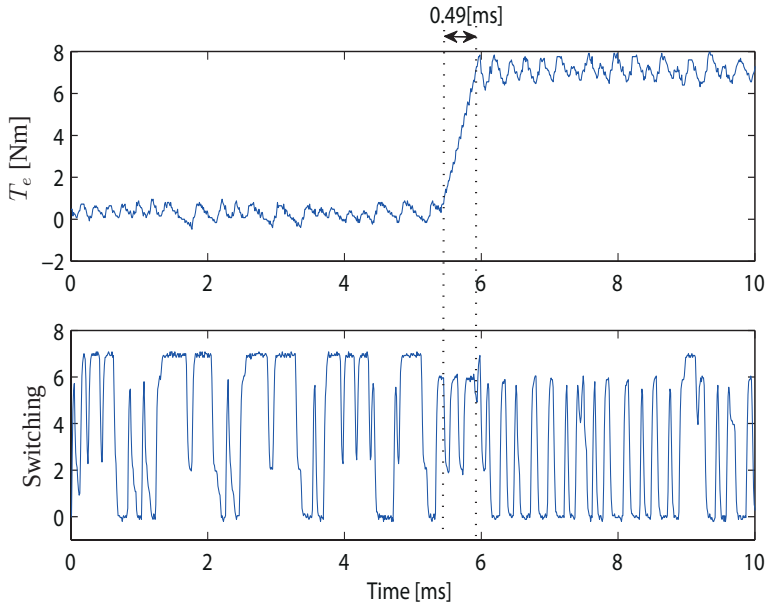

Figure 5.7: Torque step response of DTC.

for PTC and DTC is 0.49 ms. The figures also show the switching states before, during and after the torque step response. In these pictures, Switching 0 means 000, 1 means 001, ... 7 means 111. In steady state, both DTC and PTC alternate the application of active vectors with zero voltage vectors (0 and 7) to achieve the appropriate time average of the stator voltage, behaving effectively as a modulator. On the other hand, during the transient, only active vectors are applied, maximizing the actuation and hence minimizing the settling time.

The fourth test presents the performances of both strategies under a load torque impact. While the motor is rotating at 2000 rpm, a 4.0 Nm load torque (more than a half of the nominal torque) is suddenly applied to the system. The resulting speed and torque responses are presented in Fig.5.9 and Fig.5.10, respectively. Since the same speed PI-controllers are applied, the responses are equivalent.

To observer the performance of two algorithms in the whole speed range a rated speed reversal maneuver is tested. The speed alters from its positive nominal value (2772 rpm) to its negative nominal value (-2772 rpm). The same speed PI-controller is considered for both control methods. The results of speed, torque, stator current are presented in Fig. 5.11 and Fig. 5.12, respectively. It can be observed that DTC and PTC can reach very comparable performance. Since the same speed PI-controllers are used, there is no difference of the transient response. However, if the ripple of the torque signal during transient state is observed, the ripple of PTC is

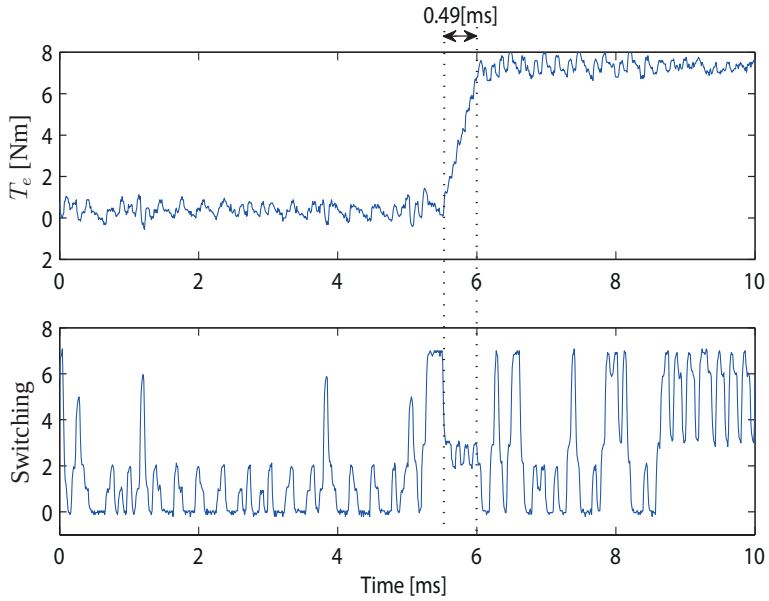

Figure 5.8: Torque step response of PTC.

lower than that of DTC method.

The last test is developed to verify the robustness of DTC and PTC methods. Both methods use the same fluxes estimation method. In reality the resistance of the motor varies with temperature, which could possibly influence the stability of the system. The measured stator resistance Rs of the drive motor is 2.68 Ω. In this test, the stator resistance Rs in the model of DTC and PTC is changed from 1.87 Ω (70 $\%$ of the measured value) to 4.0 Ω (150 $\%$ of the measured value), while the motor rotates at 300 rpm speed with an euqal average switching frequency for both algorithms. Fig. 6.8 depicits the results. It can be seen that both DTC and PTC have good and comparable robustness with respect to this parameter variation.

5.4.2 Implementation analysis

To achieve the experimental results presented above, the implementation efforts can be analyzed to figure out the difference and similarity between DTC and PTC. Both algorithms have the same merits: absence of the inner current PI controller and no modulator in system. The fast inner loops in DTC and PTC allow to increase the bandwidth of the external speed PI controller without interference. The systems are simple and reach very fast dynamics.

The calculation effort is taken into consideration and observed during implemen-

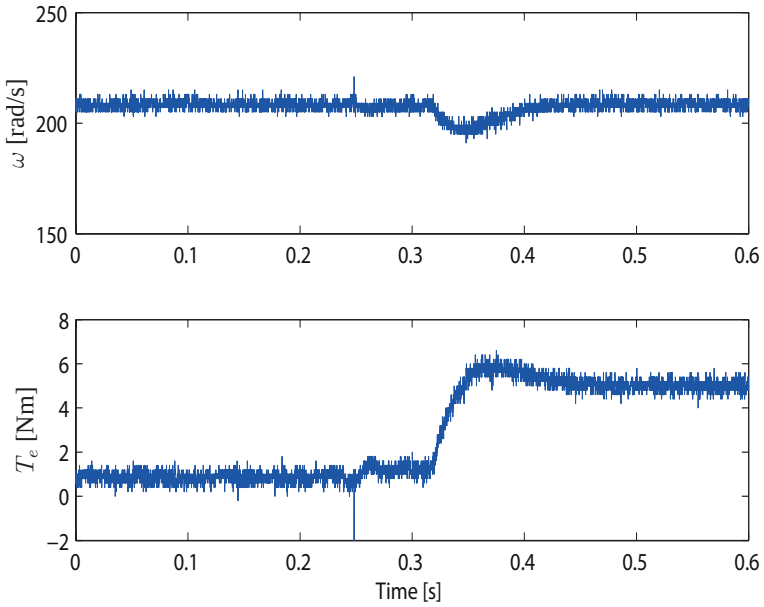

Figure 5.9: Speed and torque behaviour during a load impact on DTC.

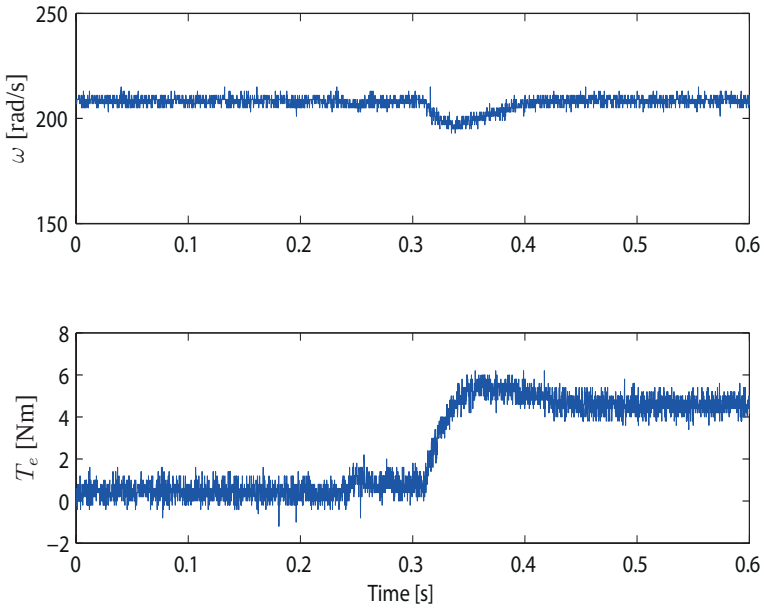

Figure 5.10: Speed and torque behaviour during a load impact on PTC.

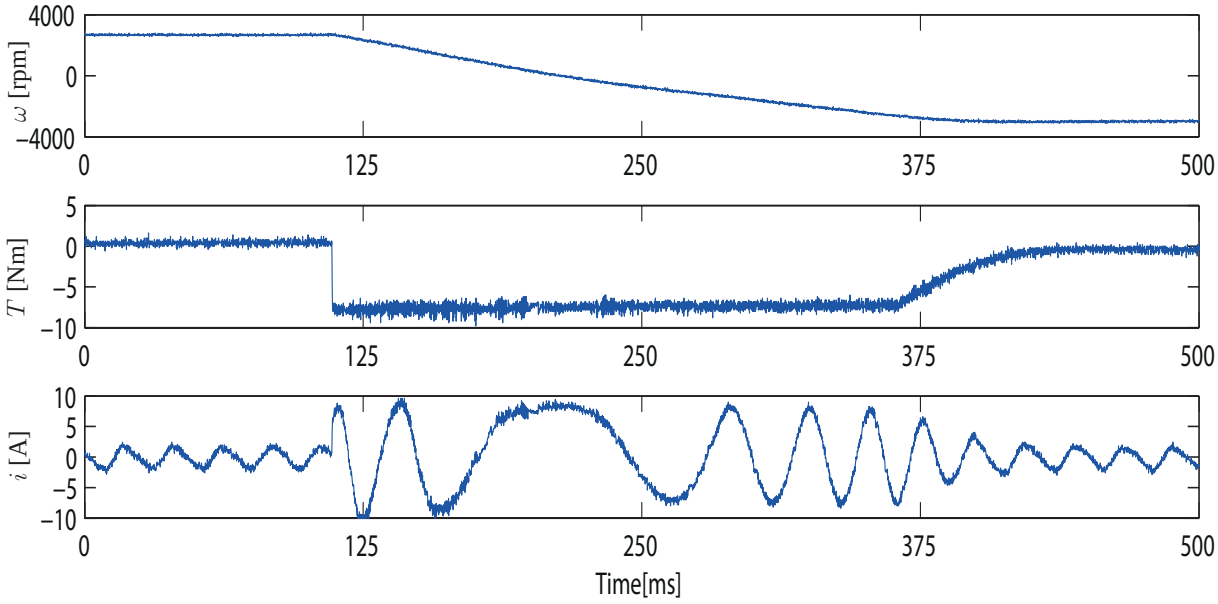

Figure 5.11: Speed, torque and stator current waveforms of DTC during a speed reversal maneuver.

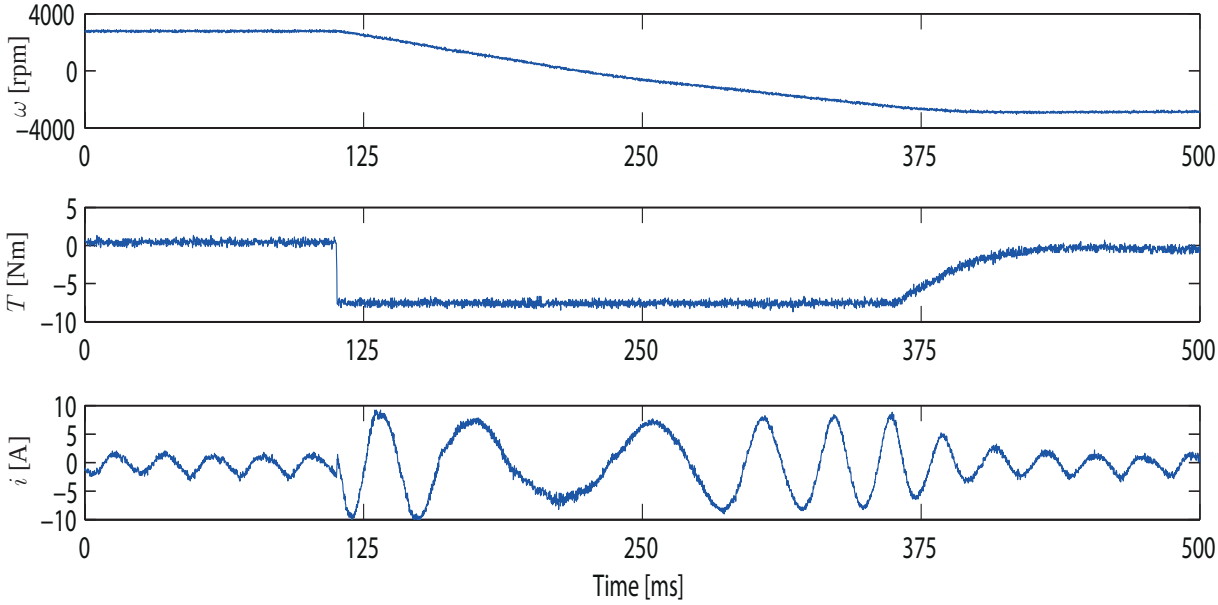

Figure 5.12: Speed, torque and stator current waveforms of PTC during a speed reversal maneuver.

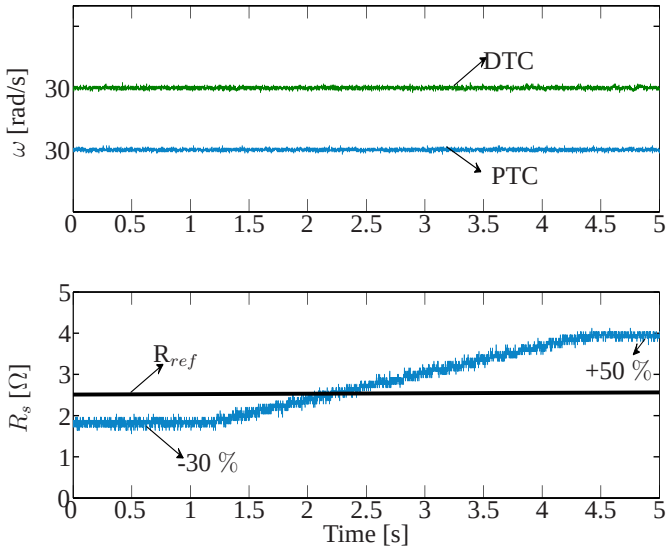

Figure 5.13: Robustness of the DTC and PTC system.

tation of both strategies. The measured algorithm calculation time of DTC and PTC are 8 μs and 20 μs, respectively. It can be seen that PTC takes more calculation time mainly because of calculation of the cost function. This results in a disadvantage of the PTC compared to the DTC method.

Both DTC and PTC methods need the same estimated variable: the stator flux. However, PTC needs no estimation of the angle of the stator flux which is necessary in DTC method.

Regarding the robustness of the systems, both methods show comparable feature. However, it should be noted that in PTC method the prediction of the stator current requires the measured rotor speed while DTC is inherently sensorless. It means that an incorrectly measured or estimated rotor speed will impact PTC system more severely than DTC system. From this point of view, the DTC system has a better robustness in its sensorless applications than the PTC method.

In DTC method, both torque and flux hysteresis controllers are necessary. To achieve better results it is necessary to tune the hysteresis bands. Therefore, there are two necessary parameters. In PTC there are two weighting factors of the cost function. They are very easy to be tuned. For the drives where only torque and flux control are concerned the switching transitions term in the cost function is neglected ($\lambda_2 = 0$). Only one parameter (λ_1) exists necessarily in the cost function. When the same importance of electromagnetic torque versus flux control is considered, this

Feature	DTC	PTC
Conceptual complexity	Higher	Lower
Calculation efforts	Lower	Higher
PI-current controllers	NO	NO
Use of Pulse Width Modulator	NO	NO
Switching frequency	Variable	Variable
Dynamics	Fast	Fast
Torque ripples (transient)	Higher	Lower
Stator current THD	Equivalent	Equivalent
Robustness	Good	Good
System Constraints Included	Hard	Easy

Table 5.1: COMPARATIVE ISSUES BETWEEN DTC AND PTC

parameter can be calculated as: $\lambda_1 = \frac{T_{nom}}{|\psi_{nom}|}$. Therefore, compared with DTC, PTC is more flexible to handle the switching frequency and the torque control quality.

In DTC method, in order to avoid damage of the motor, a current limitation must be implemented, especially at start-up. There is no optimization for over-current protection. The only way is to choose a zero voltage vector when an over-current is measured. In PTC, over-current protection can be easily included in the optimization of the cost function as described in Section IV. The vector which produces over-current will not be chosen and never be forwarded to the inverter. Of course, it must be considered that more technical goals can be included in the cost function. The used cost function in this work is a very simple one.

In a common test bench where the sampling frequency is not sufficiently high, both DTC and PTC methods need a time delay compensation. The impact of the time delay problem in DTC method is even more obvious than that on PTC strategy during tests. Without time delay compensation, only real hardware implementations are possible to reach a good performance, such as FPGAs which reach very high sampling rates (e.g. 40 kHz or higher) and can do the calculations with nearly no time delay. A model-based time delay compensation is used in this work.

5.5 Conclusion

In this chapter both PTC and DTC have been compared experimentally. The experimental results verify that both strategies can achieve comparable torque control performances both in transient and steady state. In steady state operation and under an equivalent number of commutations, both strategies can work with very similar

performance. In transient conditions, the experimental results verify that both PTC and DTC can achieve a very fast dynamic response because of the absence of inner current PI-controllers and the absence of a modulator. The selected switching vectors during transients minimize the settling time.

The comparative issues are presented in Table 5.1. It could be concluded that model predictive control emerges as a possible alternative in the field of electrical drives. However, there are still some open questions to solve, such as the performance of PTC in field weakening and a formal method to find the weighting factor when the cost function considers more than two control variables.

CHAPTER 6

PTC method with an extended prediction horizon

6.1 Introduction

Various FCS-MPC methods have been investigated. Predictive current control methods (PCC) [54, 74] are proposed to solve the current control issues in electrical drive systems. In [74] it is compared with hysteresis and pulsewidth modulation current control and shows comparable performance. Predictive speed control (PSC) [75] realizes the direct speed control method by using the FCS-MPC algorithm. With this PSC a predictive model is built by directly considering the speed control in the cost function. Model predictive torque control (MPTC) [45, 46, 76] is an important one and was already adopted into sensorless applications [77]. In [73] the MPTC is experimentally proved to be a powerful alternative control method for electrical drives. Similar to DTC method, the electromagnetic torque and the stator flux are controlled for minimum ripples in MPTC method. The difference is that, MPTC uses an internal predictive model to replace the hysteresis controllers and the look-up table. Based on the prediction horizon MPTC can be classified into one step prediction and long prediction horizons ($>$1 step). Like playing chess, longer prediction horizon is alway expected to get better results. However, longer prediction horizons mean more extensive online calculation effort which is a problem on a common test bench. The reason is that FCS-MPC method considers all possible voltage vectors of the applied inverter in every sampling interval. For example, with a two-level voltage source inverter, one-step based MPC needs to calculate 7 different voltage vectors within one sampling interval. However, two-step based MPC requires a 7^2 calculations. In [78] by adopting techniques from mathematical programming, most notably branch and bound concept, the number of switching se-

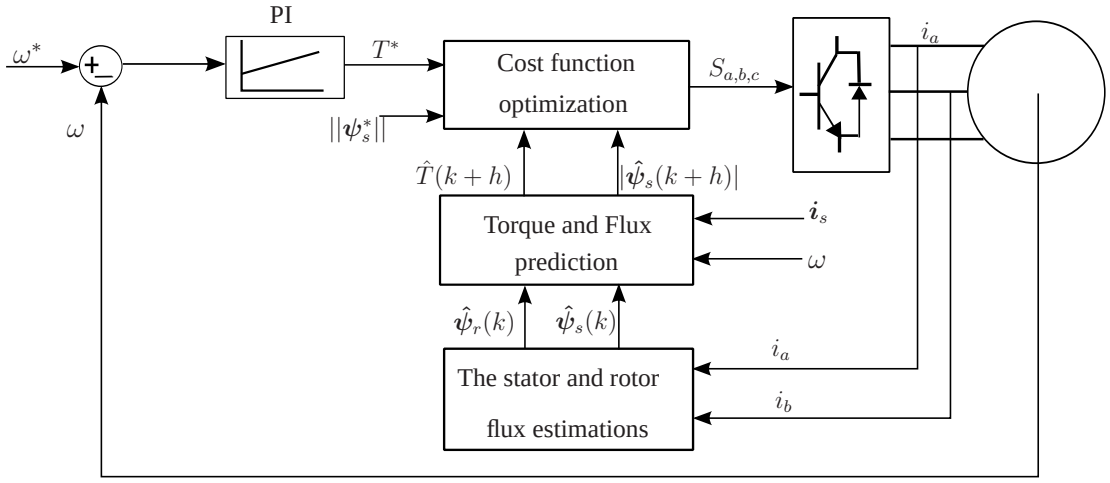

Figure 6.1: Block diagram of Predictive Torque Control.

quences explored can be significantly reduced by discarding suboptimal sequences. In [79] a heuristic strategy is introduced for reducing the calculation effort, but by cost of the system complexity. In [80] a method is proposed for reducing the switching losses for high power voltage source inverter. Furthermore, this method gives a possible solution to achieve long prediction horizons while all advantages of the original FCS-MPC method are kept, especially the intuitive algorithm and simple implementation.

In this chapter an extended prediction horizon based MPTC is implemented for an induction machine (IM). A cost function is constructed by considering the torque error, the stator flux error and an over-current constraint. The method is carried out experimentally.

6.2 Predictive torque control

The block diagram of MPTC method is described in Fig. 6.1. An MPTC method includes mainly three steps: the stator and rotor flux estimations, the electromagnetic and the stator flux predictions and the cost function design. An external speed PI controller is required to realize the adjustable speed drives. The system does not need any modulator. The switching signals selected by minimizing the cost function are directly switched to the output connected to the inverter.

In MPTC, long prediction horizon is expected to get better results than a single step prediction. As described in Fig. 6.2, one-step and two-step based MPTC are

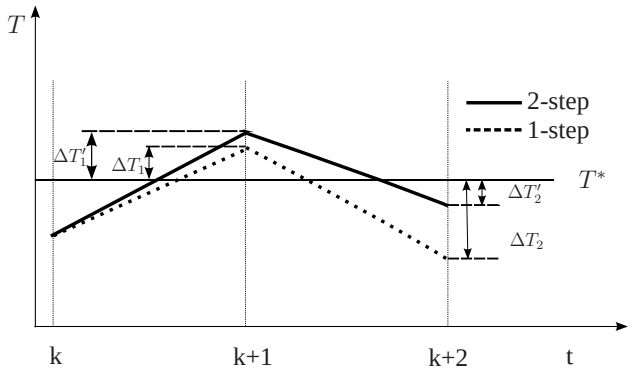

Figure 6.2: Ripple analysis between different prediction horizons.

analyzed. In the picture, ΔT_1 and ΔT_2 denotes the torque error of a single step based method at t(k+1) and t(k+2), respectively; $\Delta T_1'$ and $\Delta T_2'$ are the corresponding torque error for a two-step based method. With an one-step prediction, a low torque ripple in next step t(k+1) is guaranteed with a selected voltage vector which minimizes the cost function. However, this is possible to lead a high torque ripple in t(k+2). It means: $\Delta T_2 > \Delta T_1$. With a two-step prediction, the controller considers a minimum torque ripple for both t(k+1) and t(k+2) time step. The two-step based controller will select the best voltage vector which considers the torque ripple for two intervals. A minimum value of $(\Delta T_1' + \Delta T_2')$ is evaluated. It is possible to conclude that: $\Delta T_1 < \Delta T_1'$, but $(\Delta T_1 + \Delta T_2)/2 > (\Delta T_1' + \Delta T_2')/2$. Therefore, when an average torque ripple for two intervals is considered, long prediction horizon has possibly better results. In this paper, a two-step based MPTC is developed, with which a low average torque ripple can be achieved.

However, with a two-step prediction horizon, MPTC method has a problem of the big calculation burden. As depicited in Fig. 6.3, the conventional method considers all possible switching vectors within a single sampling interval. With a two level voltage source inverter introduced in section II, it has 8 different switching possibilities but 7 different voltage vectors. Therefore, with a two-step prediction, the controller has to calculate the algorithm $7^2 = 49$ times which is not an easy task for a common test bench. In Fig. 6.3 a reduced switching selection method is also introduced. The method allows a maximum one switching transition in a sampling instant [80]. In this way, a two-step based MPTC needs only $4^2 = 16$ times of the algroithm calculation, which can be applied on most test benches.

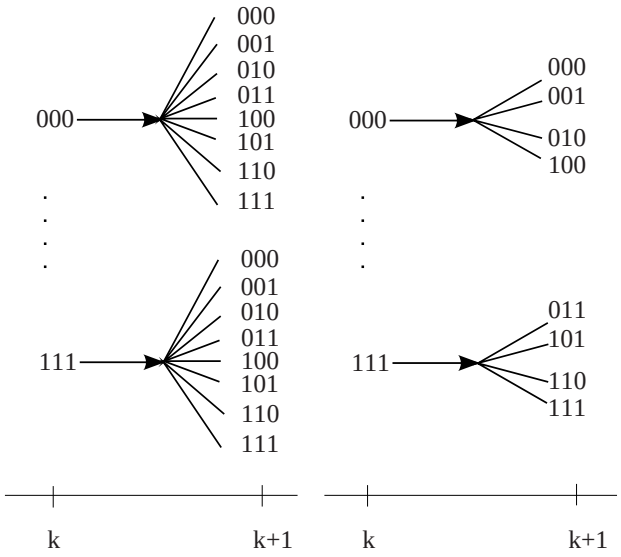

Figure 6.3: Switching state selection rules. Left: the conventional switching vector selection method. Right: the reduced calculation method.

6.2.1 The stator flux and electromagnetic torque predictions

For an extended prediction horizon, both 1-step and 2-step prediction values of the stator flux $\hat{\boldsymbol{\psi}}_s(k+h)$ and the electromagnetic torque $\hat{T}(k+h)$ must be calculated [47].

By using the same method described in chapter 5, the stator flux and current predictions can be obtained. The stator flux in time instant $(k+1)$ can be obtained as following:

$$\hat{\boldsymbol{\psi}}_s(k+1) = \hat{\boldsymbol{\psi}}_s(k) + T_s \cdot \boldsymbol{v}_s(k) - R_s \cdot T_s \cdot \boldsymbol{i}_s(k). \tag{6.1}$$

With the value of $\hat{\boldsymbol{\psi}}_s(k+1)$, the predicted stator flux at $(k+2)$ can be calculated.

$$\hat{\boldsymbol{\psi}}_s(k+2) = \hat{\boldsymbol{\psi}}_s(k+1) + T_s \cdot \boldsymbol{v}_s(k+1) - R_s \cdot T_s \cdot \boldsymbol{i}_s(k+1). \tag{6.2}$$

Similarly, the stator current at $(k+1)$ and $(k+2)$ can be predicted.

$$\begin{aligned}\hat{\boldsymbol{i}}_s(k+1) = (1 - \tfrac{T_s}{\tau_\sigma}) \cdot \boldsymbol{i}_s(k) + \tfrac{T_s}{\tau_\sigma}\tfrac{1}{R_\sigma} \cdot [k_r \cdot (\tfrac{1}{\tau_r} \\ -j \cdot \omega(k)) \cdot \hat{\boldsymbol{\psi}}_r(k) + \boldsymbol{v}_s(k)],\end{aligned} \tag{6.3}$$

$$\begin{aligned}\hat{\boldsymbol{i}}_s(k+2) = (1 - \tfrac{T_s}{\tau_\sigma}) \cdot \boldsymbol{i}_s(k+1) + \tfrac{T_s}{\tau_\sigma}\tfrac{1}{R_\sigma} \cdot [k_r \cdot (\tfrac{1}{\tau_r} \\ -j \cdot \omega(k)) \cdot \hat{\boldsymbol{\psi}}_r(k+1) + \boldsymbol{v}_s(k+1)].\end{aligned} \tag{6.4}$$

With the predicted stator flux and the predicted current, the electromagnetic torque can be predicted:

$$\hat{T}(k+h) = \frac{3}{2} \cdot p \cdot Im\{\hat{\boldsymbol{\psi}}_s(k+h)^* \cdot \hat{\boldsymbol{i}}_s(k+h)\}. \tag{6.5}$$

where $h = 1, 2$.

6.2.2 Cost function

A cost function is essential to MPC methods. The use of a cost function is also an advantage of all MPC methods. In the cost function the required control variables and system constraints can be easily included. The control tasks of MPTC method are the torque control and the flux control. Therefore, the torque and the stator flux errors between the predicted values and the references are evaluated. The over-current protection is included as a system constraint. The MPTC method seeks for always very fast dynamics, including the start-up process. It may generate an over-current phenomenon. With an over-current limitation the system will be very safe. The cost function of an extended prediction horizon is definied as following:

$$\begin{aligned} g_j = \sum_{h=1}^{N} \{ & |T^* - \hat{T}(k+h)_j| + \lambda \cdot | \parallel \boldsymbol{\psi}_s^* \parallel \\ & - \parallel \hat{\boldsymbol{\psi}}_s(k+h)_j \parallel | + I_m(k+h) \} \end{aligned} \tag{6.6}$$

where h is the prediction horizon and h = 1,2,3...N. j means the corresponding voltage vector. In this work, only 4 possible switching possibilities are considered within one sampling interval. Thus, $j = 1, 2, 3, 4$. λ is the weighting factor which weighs the relative importance of the torque control versus the stator flux control. When their importance is considered equally, the value is: $\lambda = \frac{T_{nom}}{|\bar{\psi}_{nom}|}$. An over-current protection part is included in the cost function as a system constraint. When the voltage vector which generates an over-current value in next step, the value of $I_m(k+h)$ is infinitive. Therefore, this voltage vector will not be selected. The $I_m(k+h)$ is defined as following:

$$I_m(k+h) = \begin{cases} 0 & \textit{if } |i(k+h)| \leq |i_{max}|, \\ \infty & \textit{if } |i(k+h)| > |i_{max}|. \end{cases} \tag{6.7}$$

where $|i(k+h)| = \sqrt{i_\alpha^2(k+h) + i_\beta^2(k+h)}$.

Finally the execution of the MPTC algorithm is explained in Algorithm 2.

Algorithm 2 The execution of the MPTC algroithm

1: Initialize the system and build a table of voltage vectors for realizing the maximum one switching transition method.
2: Measurement of ω and $\boldsymbol{i}_s$.
3: Estimations of $\hat{\boldsymbol{\psi}}_s(k)$ and $\hat{\boldsymbol{\psi}}_r(k)$.
4: Predictions of $\hat{\boldsymbol{i}}_s(k+h)$, $\hat{\boldsymbol{\psi}}_s(k+h)$, $\hat{\boldsymbol{\psi}}_r(k+h)$ and $\hat{T}(k+h)$, where $h = 1, 2, 3$.
5: **for** $i = 1, 2, 3, 4$ **do**
6: $g_i = |T^* - \hat{T}(k+2)_i|$
$+\lambda \cdot |\parallel \boldsymbol{\psi}_s^* \parallel - \parallel \hat{\boldsymbol{\psi}}_s(k+2)_i \parallel| + I_m(k+2)_i$
7: **for** $j = 1, 2, 3, 4$ **do**
8: $g_j = g_i + |T^* - \hat{T}(k+3)_j|$
$+\lambda \cdot |\parallel \boldsymbol{\psi}_s^* \parallel - \parallel \hat{\boldsymbol{\psi}}_s(k+3)_j \parallel| + I_m(k+3)_j$
9: The minimum value of g_j and the coressponding switching vector $\boldsymbol{v}_i$ are kept.
10: **end for**
11: **end for**
12: $\boldsymbol{v}_i$ is injected into the inverter.

6.3 Experimental results

In experiments the observered calculation time of the algorithm is 50.6 μs. A sampling frequency of 12.0 kHz is selected to satisfy this algorithm calculation time. Firstly, a torque ripple analysis between one-step prediction and two-step prediction is developed on the test bench. The calculation the one-step prediction based MPTC is about 12.6 μs. The motor works in steady state with a 4 Nm load. Fig. 6.4 depicts torque behaviors for one-step prediction and two-step prediction based MPTC, respectively. It can be seen that the torque ripple generated by a two-step prediction is lower than that produced by a one-step prediction PTC. The torque ripple bands are about 1.6 Nm and 2.0 Nm, respectively. The torque ripple is reduced approximately by 30 $\%$ by using a two-step prediction algorithm based on the same system configurations, i.e., the same sampling time and weighting factors in cost function.

To observer the performance of a two-step based MPTC method in the whole speed range a rated speed reversal maneuver is tested. The speed alters from its positive nominal value (2772 rpm) to its negative nominal value (-2772 rpm). The overcurrent protection i_{max} is set to 10.0 A. The reference of the magnitude of the stator flux is 0.7 Wb. A speed PI-controller is considered for an adjustable speed drive. The results of speed, torque, stator current and the magnitude of the stator

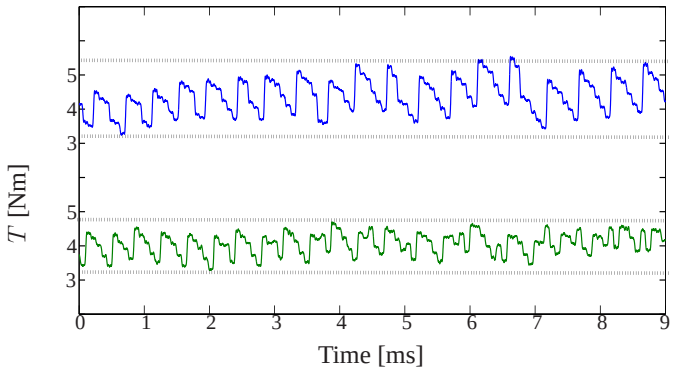

Figure 6.4: Torque behaviour. Top: torque with one-step prediction; bottom: torque with two-step prediction.

flux are presented in Fig. 6.5. It can be seen that the system works well in the whole speed range. During the transient state, the electromagnetic torque reaches its rated value (7.5 Nm) to achieve the fastest settling time. The current is limited within the setting value (10.0 A), which means the system constraint works well.

The system behaviors in steady state are observered. The motor rotates at half rated speed with a rated load torque. Fig. 6.6 presents the rotor speed, the electromagnetic torque, the stator current and the magnitude of the stator flux waveforms. From the picture, it can be seen that the torque ripples are small with this control method. The ripples are less than 1.0 Nm. More importantly, this value can even be reduced by tuning the weighting factor in the cost function. The method gets a good current quality in steady state with a load. The calculated current total harmonic distortion (THD) is 3.9 $\%$. The stator flux behavior is very well in this steady state. The test also concludes that the switching frequency in steady state is invariable: 1.2 kHz.

A load torque disturbance test is developed. The motor rotates at half rated speed. A full load torque (7.5 Nm) is suddenly added to the system as a disturbance signal. Fig. 6.7 depicits this dynamic process. From the picture, it can be observered that the system has a good performance with a very small torque ripple. The last test is developed to verify the robustness of this two-step based MPTC method. In reality the resistance of the motor varies with temperature, which could possibly influence the stability of the system. The measured stator resistance Rs of the drive motor is 2.68 Ω. In this test, the stator resistance Rs in the model is changed from 1.87 Ω (70 $\%$ of the measured value) to 3.4 Ω (130 $\%$ of the measured value), while the motor rotates at 200 rpm speed. Fig. 6.8 presents the results. It can be seen that the system has good robustness with respect to this parameter variation. However,

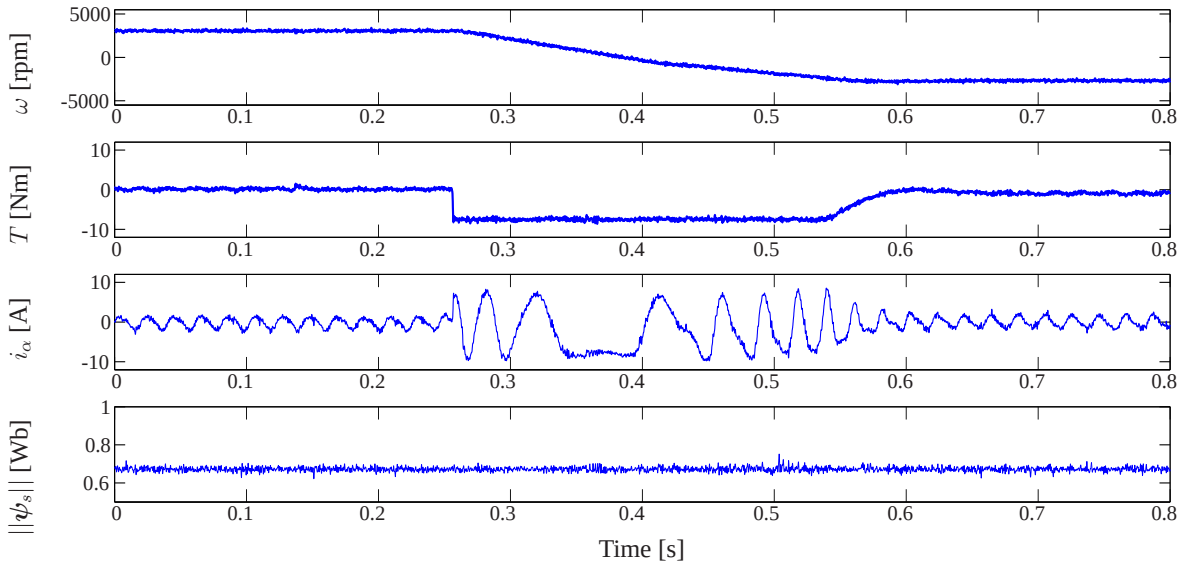

Figure 6.5: Speed, torque, stator current and stator flux magnitude waveforms of PTC during a full speed reversal maneuver.

to get a better robustness with a bigger parameter variation, some parameters online identification methods can be considered [81].

6.4 Conclusion

An extended prediction horizon based MPTC method is presented and verified experimentally in this chapter. By considering a maximum one switching transition in one interval, the calculation time of the MPTC decreases largely. A system constraint is easily included and works very well. The experimental results verify that this two-step based MPTC method works well both in steady and in transient states. The system has very fast dynamics and a low torque ripple. The system is robust with respect to a 30.0% stator resistance variation.

In the cost function, the torque and the stator errors are considered. By tuning the weighting factor, the different importance of the torque controller versus the flux controller can be decided, which shows a flexibility of the MPC system. As an alternative part, the switching transitions can also be included in the cost function design. A penalty on the switching transition can directly influence the average switching frequency. However, it emerges an open question of the needed formal

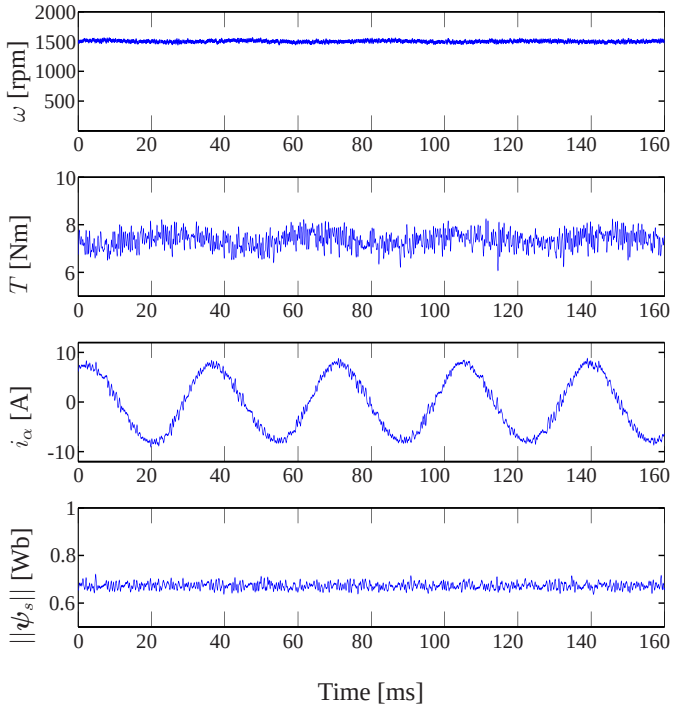

Figure 6.6: Speed, torque, stator current and stator flux magnitude waveforms of PTC in steady state with a full load.

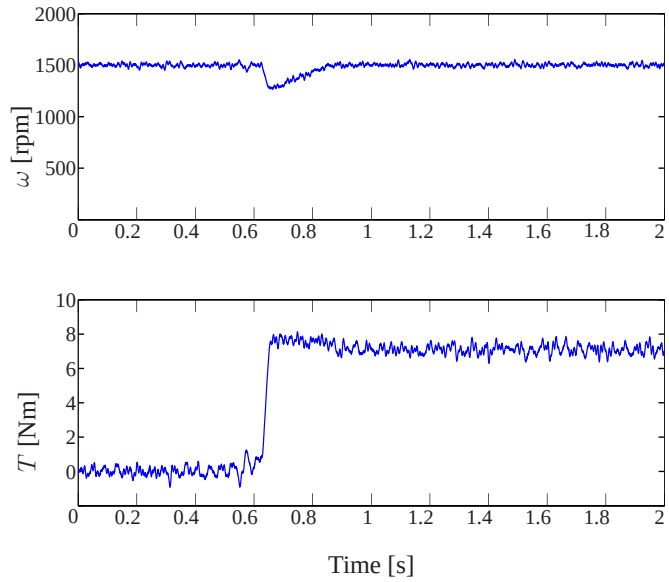

Figure 6.7: System disturbance with a full load.

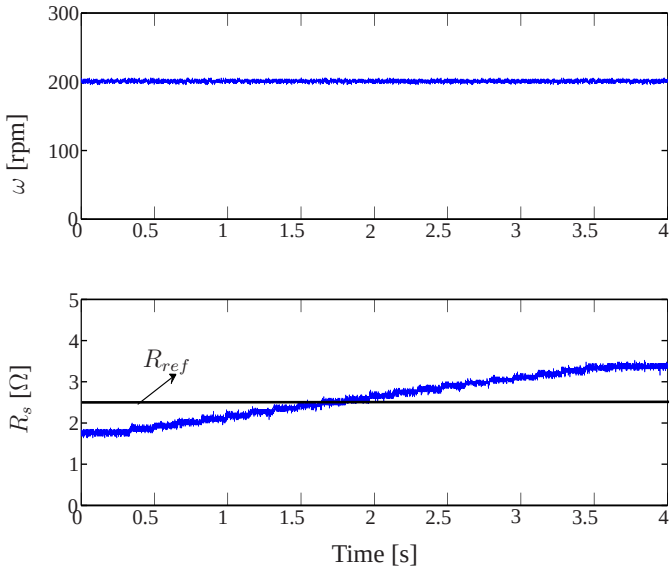

Figure 6.8: Robustness of the system with respect to the Rs variation.

method for the tuning work of the weighting factors when the cost function has more than two control variables.

CHAPTER 7

MRAS based encoderless PTC method

7.1 Introduction

PTC is also a closed loop adjustable speed controller. In almost all closed loop adjustable speed drives the measured rotor mechanical speed is required as a feedback for system controllers [1, 3]. Therefore, an encoder, speed measurement board and corresponding software are necessary for PTC design, which increase system cost and reduce reliability. The development of sensorless control methods has been favorably accepted by industries to solve these problems. By considering PTC well adaptable into sensorless applications, it is very important to find a proper observer.

During past years, many different and valuable observers have been proposed for speed estimation [27]. The simplest method is based on the reduced order observer (voltage model) [82]. It is very easy for concept understanding and implementation. But the obtained estimation accuracy is not good due to an open loop design. Extended Luenberger observers and Extended Kalman Filters (EKFs) are two promising alternatives due to the robustness to parameter changes [30, 32, 83, 84]. Unfortunately, they are difficult for implementation because of their complexities. Some more modern methods such as fuzzy logic and neural networks are researched for speed estimations [85, 86]. However, they also make the system complex. Another solution is the model reference adaptive system (MRAS) [31]. The principal of the MRAS is to estimate the speed by an adaptation mechanism. Normally, MRAS has two models: a reference model and an adjustable model. As a speed estimator, the output of the adaptation mechanism is the estimated speed which feedbacks to the adjustable model as an adjustable parameter. The input of the adaptation mechanism is the error formed by the reference model and the adjustable model.

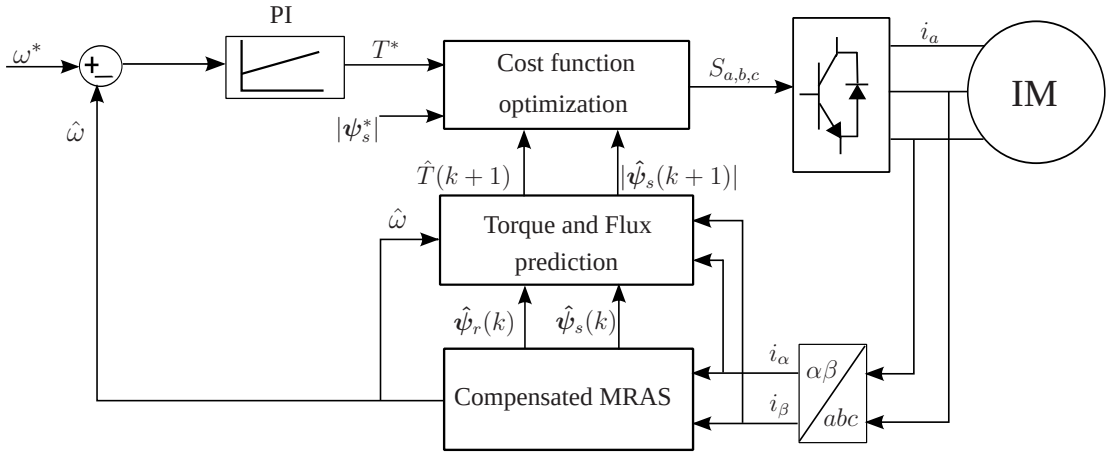

Figure 7.1: Block diagram of Encoderless Predictive Torque Control.

By forcing this error to be zero, speed estimation can be observed. The MRAS has been widely used for sensorless FOC and sensorless DTC [87, 88]. It has been approved to be a very useful, valuable and reliable observer. An important advantage of the MRAS is its less cumulative errors compared to sliding mode observer (SMO) which has been applied to PTC [89], where SMO must estimate speed angle firstly and then calculate the rotor speed by using the previous estimated values.

In this chapter, MRAS is applied into the PTC design. A MRAS based PTC is proposed to develop an encoderless PTC system for an induction machine (IM). The applied MRAS is rotor flux based. The rotor speed is estimated through a PI controller by driving the rotor flux error to zero. For obtaining a better result, the reference model of MRAS is compensated with a flux PI controller for solving the flux drift problem due to the unbalance of the measured stator currents.

7.2 A compensated MRAS based PTC

The execution of the encoderless PTC algorithm includes 3 steps: estimations of the electrical speed, the stator and rotor flux as well as the electromagnetic torque; predictions of the stator flux and electromagnetic torque; optimization function design. The architecture of encoderless PTC is described in Fig. 7.1. An external speed PI controller is used for adjustable speed control.

7.2.1 Model based states estimations

A rotor flux based MRAS is applied as observer for the required variable estimations. It consists of two models: reference model and adjustable model. These two models are independent rotor flux expressions in a stationary reference frame. The voltage model based rotor flux calculation is independent of the rotor speed $\hat{\omega}$. Therefore, it is taken as reference model:

$$\hat{\boldsymbol{\psi}}_s = \int \left(\vec{v}_s - \hat{R}_s \cdot \boldsymbol{i}_s\right) dt \tag{7.1}$$

$$\hat{\boldsymbol{\psi}}_r = \frac{L_r}{L_m} \cdot \left(\hat{\boldsymbol{\psi}}_s - \sigma \cdot L_s \cdot \boldsymbol{i}_s\right) \tag{7.2}$$

where $\hat{R}_s$ is the estimated stator resistance.

The current model based rotor flux calculation is dependent on $\hat{\omega}$. It is selected as adjustable model:

$$\hat{\boldsymbol{\psi}}_{rI} = \int \left(\frac{L_m}{\hat{\tau}_r} \cdot \boldsymbol{i}_s - \left(\frac{1}{\hat{\tau}_r} - j \cdot \hat{\omega}\right) \cdot \hat{\boldsymbol{\psi}}_{rI}\right) dt \tag{7.3}$$

where $\hat{\tau}_r = L_r/\hat{R}_r$. The adaptation mechanism of the rotor flux MRAS is designed by using a conventional PI controller.

$$\hat{\omega} = K_{pw} \cdot e_w + K_{iw} \int e_w dt \tag{7.4}$$

where K_{pw} and K_{iw} are gains of PI controller, and e_w denotes the rotor flux difference between the reference model and the adjustable model:

$$e_w = Im\{\hat{\boldsymbol{\psi}}^*_{rI} \cdot \hat{\boldsymbol{\psi}}_r\} \tag{7.5}$$

By forcing e_w to zero, the rotor speed is estimated [31].

The estimated speed is fed back to the external speed PI controller and compared with the speed reference to generate the torque reference.

Encoderless PTC requires not only the estimated rotor speed but also the estimated rotor flux and stator flux. The reference model can output the estimated stator flux and rotor flux in stationary frame. However, the reference model is based on an open loop voltage model. With this open loop voltage model, it can generate the flux as an internal variable to stabilize the estimator but not good enough for a controller. In a real industrial implementation, an offset cannot be avoided: switches resistances exist and lead to a voltage drop; measured unbalanced currents result in flux drift phenomenon. Therefore, the flux estimations cannot be directly used

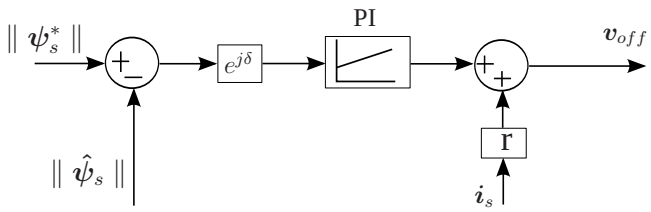

Figure 7.2: Block diagram of offset compensation.

for control without offset compensations. With such considerations, a compensated voltage model is designed as reference model:

$$\hat{\boldsymbol{\psi}}_s = \int \Big(\boldsymbol{v}_s - \hat{R}_s \cdot \boldsymbol{i}_s - \boldsymbol{v}_{off} \Big) dt \tag{7.6}$$

In this compensated voltage model,

$$\boldsymbol{v}_{off} = \boldsymbol{v}_r + \boldsymbol{v}_\psi \tag{7.7}$$

$$\boldsymbol{v}_r = r \cdot \boldsymbol{i}_s \tag{7.8}$$

$$\boldsymbol{v}_\psi = K_{pRs} \cdot e_\psi + K_{iRs} \int e_\psi dt \tag{7.9}$$

where r represents single switch resistance. K_{pRs} and K_{iRs} are gains of the flux PI regulator. e_ψ is defined as the error of the stator flux:

$$e_\psi = (\| \hat{\boldsymbol{\psi}}_s \| - \| \boldsymbol{\psi}_s^* \|) \cdot e^{j\delta} \tag{7.10}$$

where $\delta = \arctan(\dfrac{\hat{\psi}_{s\beta}}{\hat{\psi}_{s\alpha}})$.

The offset compensation is described in Fig. 7.2. By substituting this compensated $\hat{\boldsymbol{\psi}}_s$ into (7.1) and (7.2), a new reference model is built up. With this compensated reference model, a more accurate stator and rotor flux can be estimated. The output estimated flux can satisfy the controller requirement. It even can improve the accuracy of the estimated rotor speed $\hat{\omega}$.

The stator resistance R_s of the motor varies with temperature. Though the variation is very slow, the robustness of the system will be improved by estimating the acutal value of R_s. The speed estimation can also be impacted by the rotor time constant $\hat{\tau}_r = L_r/\hat{R}r$. Fortunately, this can be compensated for by varying the rotor resistance in the same ratio as the estimated stator resistance varies [90]. A stator resistance adaptation mechanism is presented as follows:

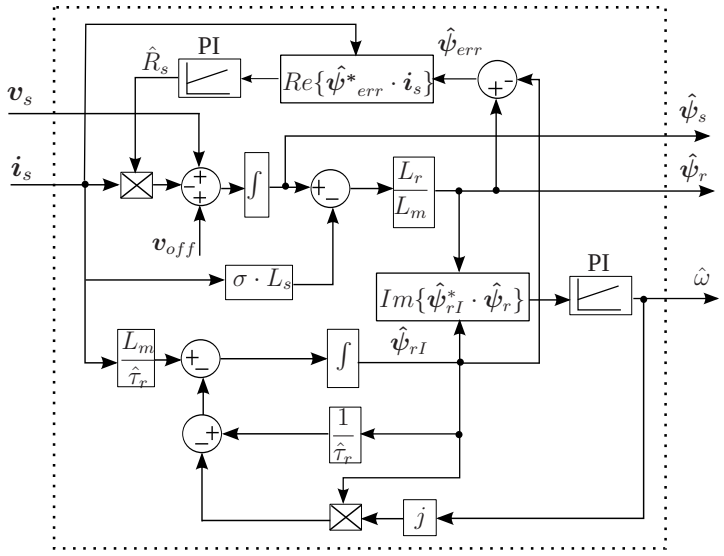

Figure 7.3: Block diagram of the compensated rotor flux MRAS.

$$e_{Rs} = Re\{(\hat{\boldsymbol{\psi}}_r - \hat{\boldsymbol{\psi}}_{rI})^* \cdot \boldsymbol{i}_s\} \tag{7.11}$$

$$\hat{R}_s = K_{pRs} \cdot e_{Rs} + K_{iRs} \int e_{Rs} dt. \tag{7.12}$$

The construct of the applied compensated MRAS is described in Fig. 7.3.

7.2.2 Stator flux and electromagnetic torque predictions

In the predictive algorithm, the next-step stator flux $\hat{\boldsymbol{\psi}}_s(k+1)$ and the electromagnetic torque $\hat{T}(k+1)$ must be calculated. To reach a more accurate prediction model, the offset compensation $\boldsymbol{v}_{off}$ is included into the voltage model. From the IM model described in chapter 2, the stator flux and the stator current can be described as follows:

$$\frac{d\boldsymbol{\psi}_s}{dt} = \vec{v}_s - \hat{R}_s \cdot \boldsymbol{i}_s - \boldsymbol{v}_{off} \tag{7.13}$$

$$\boldsymbol{i}_s = -\frac{1}{\hat{R}_\sigma}(L_\sigma \cdot \frac{d\boldsymbol{i}_s}{dt} - k_r \cdot (\frac{1}{\hat{\tau}_r} - j \cdot \hat{\omega}) \cdot \boldsymbol{\psi}_r) - \boldsymbol{v}_s + \boldsymbol{v}_{off}) \tag{7.14}$$

where $k_r = L_m/L_r$, $\hat{R}_\sigma = \hat{R}_s + k_r^2 \cdot \hat{R}_r$ and $L_\sigma = \sigma \cdot L_s$.

To predict the electromagnetic torque and stator flux, the forward Euler discretization is considered:

$$\frac{dx}{dt} \approx \frac{x(k+1) - x(k)}{T_s}. \tag{7.15}$$

The stator flux prediction can be obtained as:

$$\hat{\boldsymbol{\psi}}_s(k+1) = \hat{\boldsymbol{\psi}}_s(k) + T_s \cdot \boldsymbol{v}_s(k) - \hat{R}_s \cdot T_s \cdot \boldsymbol{i}_s(k) - T_s \cdot \boldsymbol{v}_{off}. \tag{7.16}$$

The stator current can be predicted as:

$$\begin{aligned} \hat{\boldsymbol{i}}_s(k+1) = (1 - \tfrac{T_s}{\tau_\sigma}) \cdot \boldsymbol{i}_s(k) + \tfrac{T_s}{\tau_\sigma} \tfrac{1}{R_\sigma} \cdot [k_r \cdot (\tfrac{1}{\tau_r} \\ -j \cdot \hat{\omega}(k)) \cdot \hat{\boldsymbol{\psi}}_r(k) + \boldsymbol{v}_s(k) - \boldsymbol{v}_{off}(k)], \end{aligned} \tag{7.17}$$

where $\tau_\sigma = \sigma \cdot L_s / R_\sigma$.

With predictions of the stator flux and the predicted current, the electromagnetic torque can be predicted:

$$\hat{T}(k+1) = \frac{3}{2} \cdot p \cdot Im\{\hat{\boldsymbol{\psi}}_s(k+1)^* \cdot \hat{\boldsymbol{i}}_s(k+1)\}. \tag{7.18}$$

7.2.3 Controller design

The proposed PTC method is an FS-PTC method which is designed by pre-considering a torque-band. The inverter switching state is included in the cost function. Try to restrict the switching frequency variation and reduce the switching losses are important for PTC implementation. During every sampling interval all possible switching states are evaluated. The one which minimizes the cost function will be selected as output. The pre-considered torque-band plays an important role in this strategy. The optimization method focuses on the flux error and the switching state when the torque error is within the torque-band. Therefore, in the condition that the torque error is inside the allowed torque-band, better flux response and less switching frequency variation and losses can be expected by using this method. The developed cost function is as following:

$$\begin{aligned} g_j = \sum_{h=1}^{N} \{\lambda_1 \cdot |T^* - \hat{T}(k+h)_j| + \lambda_2 \cdot | \parallel \boldsymbol{\psi_s^*} \parallel \\ - \parallel \hat{\boldsymbol{\psi}}_s(k+h)_j \parallel | + \lambda_3 \cdot |S(k) - S(k+h)_j|\} + I_m \end{aligned} \tag{7.19}$$

where $j = 0...6$, because a two-level voltage source inverter is applied in this system. All possible voltage vectors are presented in Fig. 7.4. It is easy to see that the

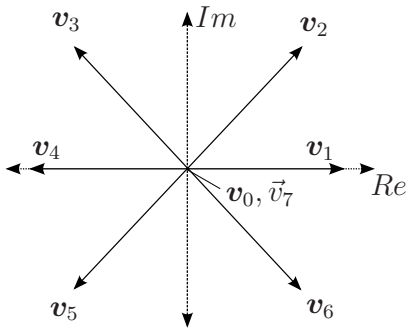

Figure 7.4: Voltage vectors of two-level voltage source inverter.

inverter has 8 different switching states but only 7 different voltage vectors. Thus, the cost function only needs to be calculated 7 times. Therefore, g_j has 7 different values. Among these values, the one which minimizes the g_j is selected as the output signal. h is the predictive horizon. In this work an one step PTC is considered and h = 1.

In this cost function the weighting factor λ_1 is designed by considering a torque band. When the torque error is inside this band, λ_1 is considered as zero. λ_1 is designed as:

$$\lambda_1 = \begin{cases} 0 & \textit{if } |T^* - \hat{T}(k+h)_j| \leq |T_{\text{band}}|, \\ > 0 & \textit{if } |T^* - \hat{T}(k+h)_j| > |T_{\text{band}}|. \end{cases} \tag{7.20}$$

where T_{band} is the value of the torque band.

In 7.19 the coefficient λ_2 denotes the weighting factor, which weighs the relative importance of the electromagnetic torque versus flux control. When their importance is considered equally, this coefficient should be chosen as: $\lambda_2 = \frac{T_{nom}}{|\boldsymbol{\psi}_{nom}|}$. λ_3 is the coefficient for the switching state. By choosing λ_3 properly, a reduction of switching frequency variation and switching losses can be expected.

The torque reference T^* is generated by a speed PI-controller.

$$T^* = K_{pt} \cdot (\omega^* - \hat{\omega}) + K_{it} \int (\omega^* - \hat{\omega}) dt \tag{7.21}$$

where K_{pt} and K_{it} are gains of the speed PI controller.

As a protection part, the current limitation term is active when the absolute value of the predicted current is higher than its limit. The current limitation is defined as:

$$I_m = \begin{cases} 0 & \textit{if } |i| \leq |i_{max}|, \\ \infty & \textit{if } |i| > |i_{max}|. \end{cases} \tag{7.22}$$

where $|i| = \sqrt{i_\alpha^2(k+1) + i_\beta^2(k+1)}$.

7.2.4 Implementation and experimental results

Implementation consideration

One of the disadvantages of PTC is the long calculation effort because of the optimization function. The selection of sampling frequencies must be analyzed. On the available test bench, the highest sampling frequency is 24 kHz. With a higher sampling frequency, better current measurements can be obtained. However, with this sampling frequency, the system cannot reach the expected performance, because with 24 kHz sampling interval, it means the interval time is 41.7 μs. By observing the execution time including the interrupt latency of the RTAI Linux, the A/D and D/A conversion time and pure algorithm implementation, it is about 47 μs which is longer than sampling interval. To keep a balance between the sampling and calculation, the selected sampling frequency and corresponding algorithm implementation time are: 16 kHz and 47 μs.

Another problem of FS-PTC is its variable and low switching frequencies because of the absence of PWM modulator. It can reduce the variation of the switching frequency by adding a switching state term in the cost function. However, it is almost impossible to reach an invariable switching frequency as in FOC method which has a modulator. Therefore, the current performance is not as good as that of FOC method when the current THD is taken into analysis [73]. However, the MRAS observer strongly depends on the stator currents, especially in low speed range. With 16 kHz sampling frequency, the average switching commutations can reach almost 2.3 kHz per IGBT at middle and high speed. But at low speed, the average switching frequency is around 1 kHz. This low and variable switching frequency leads to a big current THD. An experimental test is developed to confirm this. With a speed encoder, the motor rotates at 50 rpm without load. The stator current THD has been calculated. The index is 42.01 $\%$ which is very high. Therefore, it is difficult to reach very accurate speed estimations with very low speed.

Experimental results

The first test shows the validity of the compensated MRAS. A comparison test between original MRAS and compensated MRAS is observed. Fig. 7.5 presents the result. From the picture, the stator flux generated by MRAS without compensation has the obvious drift phenomenon and it cannot be used by predictive controller. The compensated MRAS works much better. It eliminates the flux drift

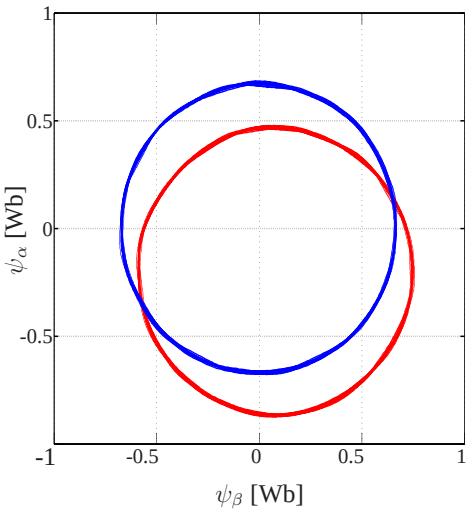

Figure 7.5: Stator flux with and without offset compensation.

phenomenon and it can output qualified and reliable estimated flux for PTC.

The second test is to observe the dynamics of the encoderless PTC. The torque step is 7.5 Nm (rated torque value) which is generated by a sudden speed change (200 rpm to 2600 rpm). Fig. 7.6 presents torque step and corresponding IGBT switching states during this dynamic process. In picture, switching 0 means 000, ... 6 means 110. Before and after the torque step dynamics, the switching state changes between zero state (0 and 7) and active states (1 to 6). However, during a torque step only active states are selected, which results in a fast settling time and fast dynamics.

The third test is developed for the wide range speed estimation. The speed reference changes from nominal speed (2772 rpm) to minus nominal speed (-2772 rpm). The measured and the estimated speed, the stator current and the estimated torque are presented in Fig. 7.7. It can be seen that both observer and controller work very well during this process. Fig. 7.8 shows the stator flux performance. The flux reference is set to 0.71 Wb. The estimated speed can track measured speed very well especially at steady states. To read a accurate speed error, Fig. 7.9 presents the speed error between estimated speed and measured speed. The speed error is calculated as $\Delta\omega = \frac{\omega - \hat{\omega}}{\omega} * 100\%$. For each group sampled data from oscilloscope, it has 100 k points. To show a clear and readable error information, all the presented error information in this paper are calculated by using an average value of every 100 points from the source. During transient, the motor crosses the very low speed

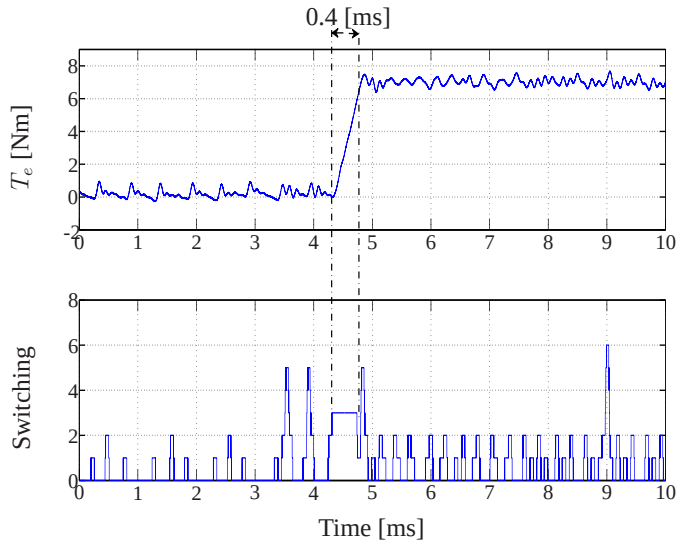

Figure 7.6: Torque step response.

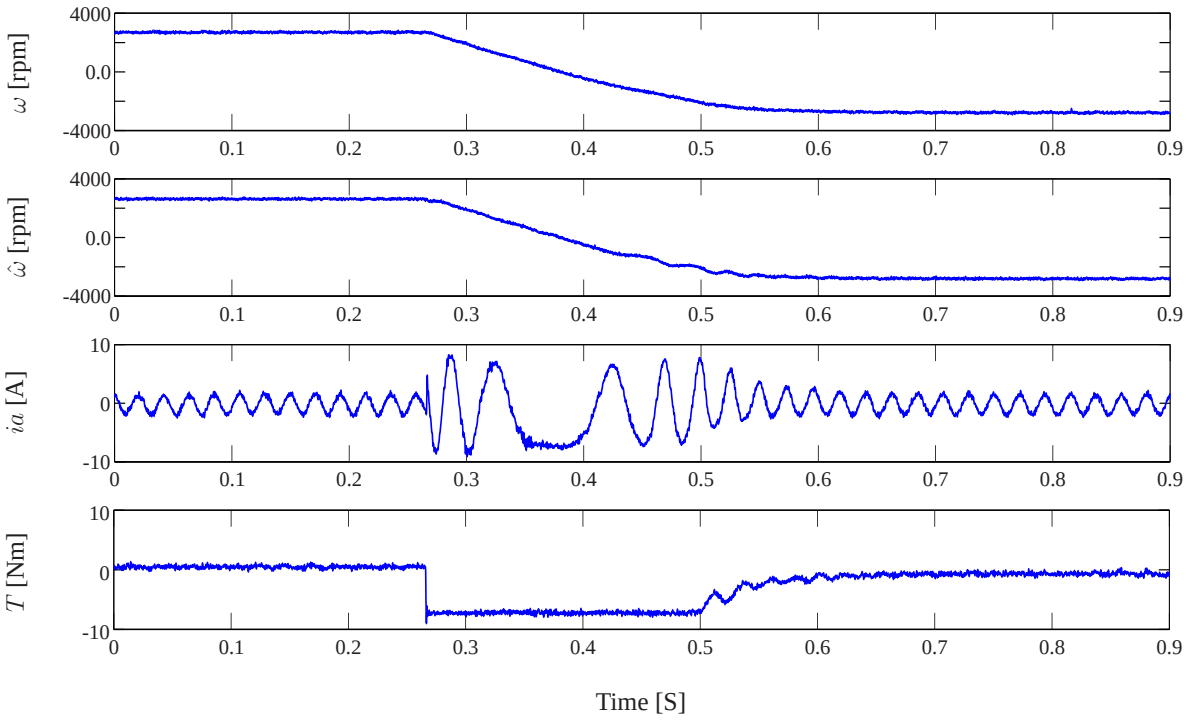

Figure 7.7: Measured speed, estimated speed, stator current and torque waveforms during a rated speed reversal maneuver.

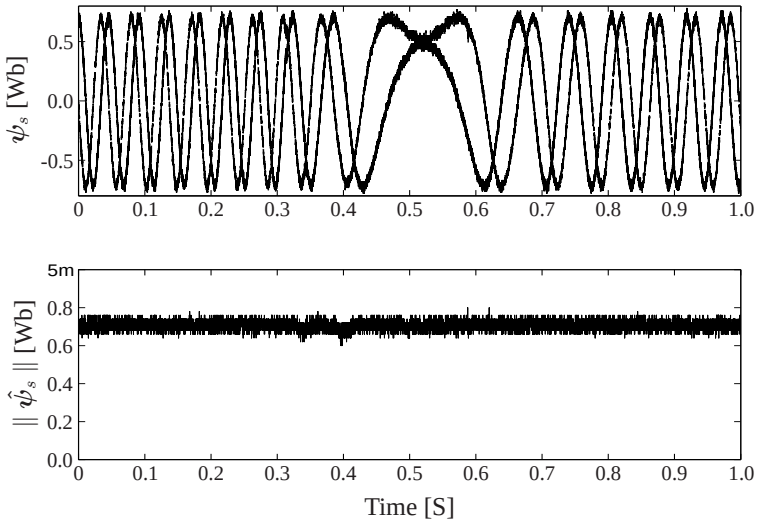

Figure 7.8: Stator flux performance during a rated speed reversal maneuver.

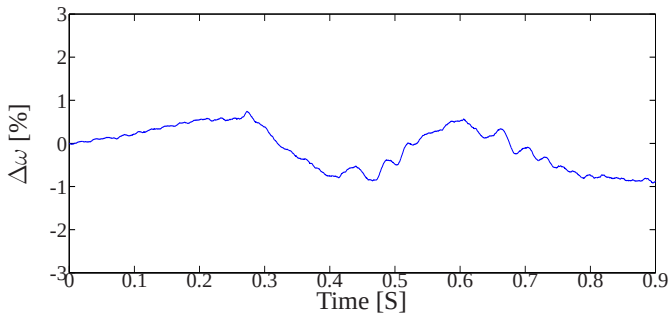

Figure 7.9: Speed error during a rated speed reversal maneuver.

region (include zero speed). Therefore, the $\Delta\omega$ is higher. The mean value of $\Delta\omega$ at steady states is 0.4 %. The calculated stator current THD is 12.0 % at steady states.

The fourth test is to observe the low speed performance. A slow speed reversal process is observed. The speed reference alters from 60 rpm (1.0 Hz) to -60 rpm. Fig. 7.10 shows the measured speed, estimated speed, stator current and estimated torque response. From the picture, the system is stable in low speed region. However, the speed error during transient is not so good because of the big current THD (around 40.0 %) at very low speed and variable switching frequency. Fig. 7.11 shows the detailed speed errors during the whole dynamic process. The highest speed error point during transients is almost 21.0 %. The mean value at steady state is 5.5 %.

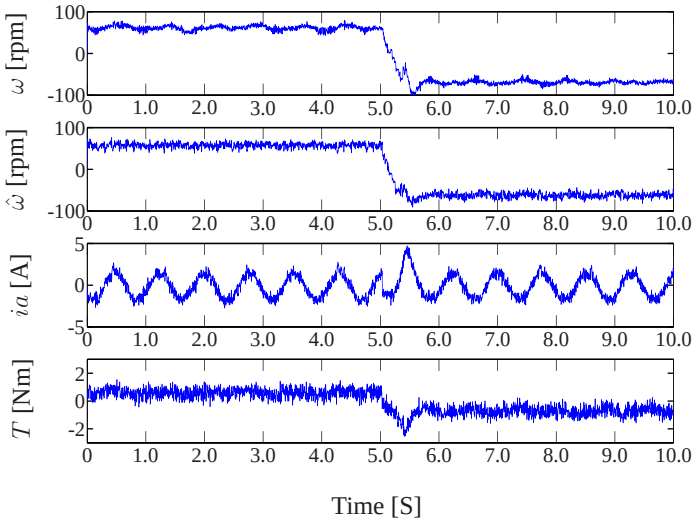

Figure 7.10: Low speed reversal maneuver performance.

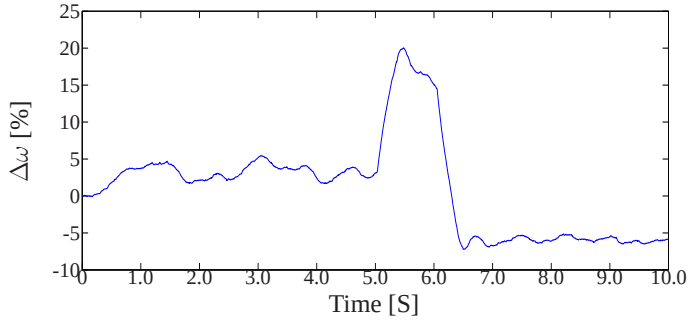

Figure 7.11: Speed error during a low speed reversal maneuver.

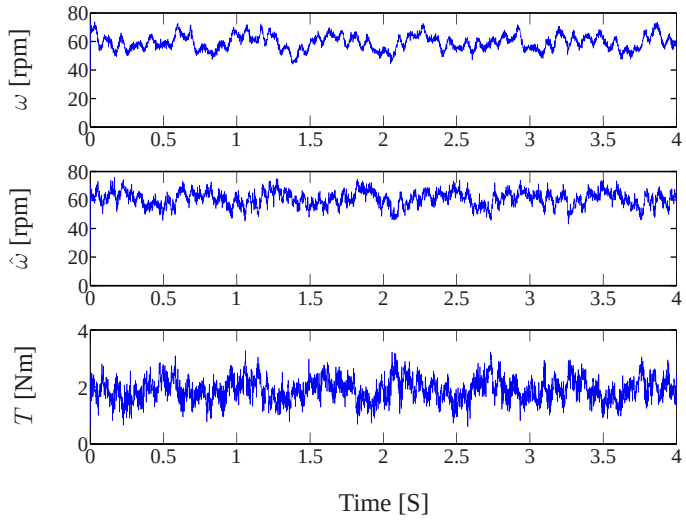

Figure 7.12: Low speed steady behavior with a load.

The performance of the system over a load torque is also important. A low speed performance with a load at steady state and a high speed performance with a full load disturbance are observed in this work, respectively. Fig. 7.12 presents the performance of the low speed performance with a load. The motor rotates at a low speed (60 rpm) with a 25 $\%$ of the nominal load. In this picture, the measured and the estimated speed, the stator current and the torque are depicted. The system is stable. A full load is taken into consideration as a disturb and added to the system. The motor rotates at norminal speed (2772 rpm). A 7.5 Nm load is suddenly added to the system as a disturbance. Fig. 7.13 shows the response of the measured speed and the estimated speed and the torque. The results show that the system has a good performance over a full load disturbance. Before and after added load, the calculated stator current THD is 12.0 $\%$ and 3.0 $\%$, respectively.

To analyze the robustness of the system, the influence brought by the variations of the stator resistance is observed. Initially, the value of the stator resistance is set to 70 $\%$ of the measured value (2.68 Ω). In a few seconds the stator resistance estimator is turned on. Fig. 7.14 presents the results for this $\hat{R}_s$ estimation process. The picture shows that the estimator works well to track the real resistance value. Furthermore, both the measured and the estimated speed keep almost the same value during process of this resistance variations. It shows that the applied encoderless FS-PTC method has a good robustness over a 30 $\%$ variations of the stator resistance.

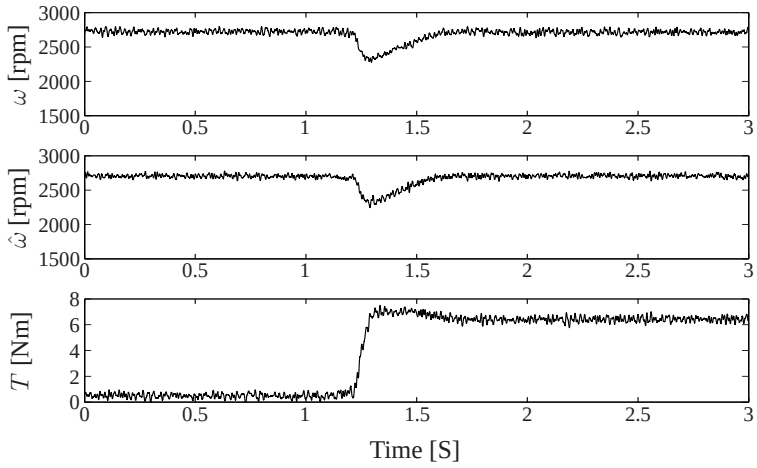

Figure 7.13: A full load disturbance at the nominal speed.

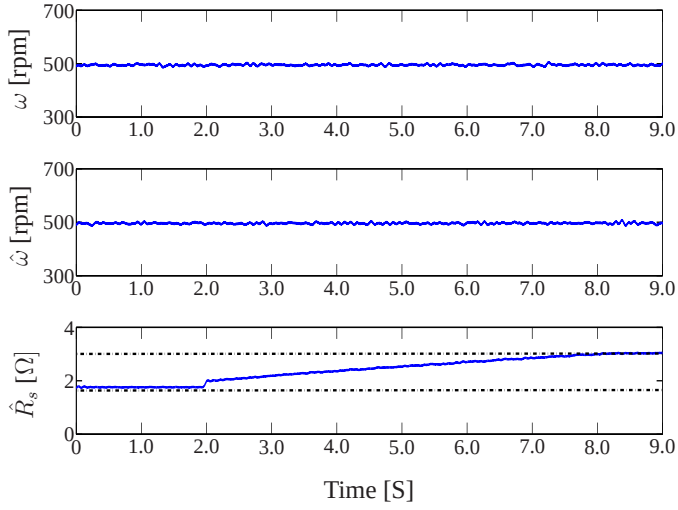

Figure 7.14: The process of the stator resistance estimation.

7.3 A sliding mode MRAS based PTC

7.3.1 A sliding mode MRAS design

For obtaining the qualified flux estimations, sliding mode observer (SMO) is investigated for the flux estimations and it has been approved a reliable and accurate observer [33,91]. To compensate the offset and estimate the flux accurately, a SMO based voltage model is considered as a reference model of MRAS in this work. The sliding surface is built by using a saturation function for reducing the chattering noise. The sliding function is built as:

$$Sat(x) = \begin{cases} -1 & \textit{if } x - \hat{x} < \Delta, \\ (x - \hat{x})/\Delta & \textit{if } |x - \hat{x}| < \Delta, \\ 1 & \textit{if } x - \hat{x} > \Delta. \end{cases}, \tag{7.23}$$

where $x = i_\alpha$ and i_β, Δ is a tuning parameter.

The new reference model by using the sliding mode method is described as:

$$\frac{d}{dt}\hat{\boldsymbol{\psi}}_s = \boldsymbol{v}_s - R_s \cdot \boldsymbol{i}_s + k \cdot Sat(\boldsymbol{i}_s - \hat{\boldsymbol{i}}_s), \tag{7.24}$$

$$\hat{\boldsymbol{i}}_s = \frac{1}{L_\sigma^2} \cdot (L_r \cdot \hat{\boldsymbol{\psi}}_s - L_m \cdot \hat{\boldsymbol{\psi}}_r), \tag{7.25}$$

where $L_\sigma^2 = \sigma \cdot L_s \cdot L_r$ and k is the slding mode gain. To reduce the chattering problem and compensate the offset, the k is designed by including the PI dynamics [92].

$$k = k_{1p} + \frac{k_{1i}}{s}, \tag{7.26}$$

where k_{1p} and k_{1i} are the gains of the PI controller.

7.3.2 The required system signals prediction

By considering the proposed prediction model in [73] and the same SMO compensation method in the observer, a sliding mode based prediction model is developed. The stator flux, the stator current and the electromagnetic torque can be predicted as follows:

$$\hat{\boldsymbol{\psi}}_s(k+1) = \hat{\boldsymbol{\psi}}_s(k) + T_s \cdot \boldsymbol{v}_s(k) - T_s \cdot R_s \cdot \boldsymbol{i}_s(k) + T_s \cdot k \cdot Sat(\boldsymbol{i}_s - \hat{\boldsymbol{i}}_s), \tag{7.27}$$

$$\begin{aligned}\hat{\boldsymbol{i}}_s(k+1) = (1-\tfrac{T_s}{\tau_\sigma})\cdot \boldsymbol{i}_s(k) + \tfrac{T_s}{\tau_\sigma}\tfrac{1}{R_\sigma}\cdot[k_r\cdot(\tfrac{1}{\tau_r} - j\cdot\hat{\omega}(k))\\ \cdot\hat{\boldsymbol{\psi}}_r(k) + \boldsymbol{v}_s(k) + k\cdot Sat(\boldsymbol{i}_s - \hat{\boldsymbol{i}}_s)],\end{aligned} \tag{7.28}$$

The tuning of the sliding mode gain k is the same with that in the observer, because they use the same model for predictions and observations.

7.3.3 Experimental results

The first test is to verify the system performance in full speed range without the load. The speed reference changes from 2772 rpm (nominal speed) to -2772 rpm and then returns to 2772 rpm. The measured speed, the estimated speed, the speed error, the electromagnetic torque and the stator current are presented in Fig. 7.15. From the figure, the system works well in full speed range. The peak value of the speed error between the measured speed and the estimated speed is less than 18 rpm which is occured in zero speed. But the average value of the speed error during the whole working time is zero. During the trajectory from 2772 rpm to -2772 rpm, the torque reaches reference is let to be set at the maximum value for achieving a fast dynamics. The stator flux is also observed during the full speed reversal manuever. Fig. 7.16 shows the measured speed, the stator flux value in α and β and the magnitude of the stator flux. The stator flux reference is set to be 0.91 Wb. Fig. 7.16 verifies that the stator flux is controlled well. The flux control is not affected even when zero speed is crossed. It shows that speed estimation error will not influence the flux estimation and control.

The second experiment is to test the system performance with a load impact. A suddenly load change (from no load to 40 %) is exerted at time instant 1.3 s while the speed was kept at -1500 rpm. Fig. 7.17 shows the system has a good load disturbance response. At time instant 2.4 s, the speed reference changes to 1500 rpm from -1500 rpm while keeping the 40 % load connected on the system. Fig. 7.17 presents good speed reversal maneuver with the load. From the figure the the peak value of the speed errors between the measured and the estimated speed at a time instant is about 20 rpm. The average value at steady state is zero.

The performance at low speed is important. Fig. 7.18 presents the low speed reversal maneuver performance. The speed reference changes from 100 rpm to -100 rpm without load. From the Fig. 7.18, the system can track the speed reference well. The errors during the transient is big because the acrossing of the standstill. The peak value is about 85 rpm while the mean value is about 45 rpm. At steady states, the peak of the speed errors between the measured and the estimated speed is 10 rpm. However, the average error is almost zero. It shows the merit of the sliding mode method.

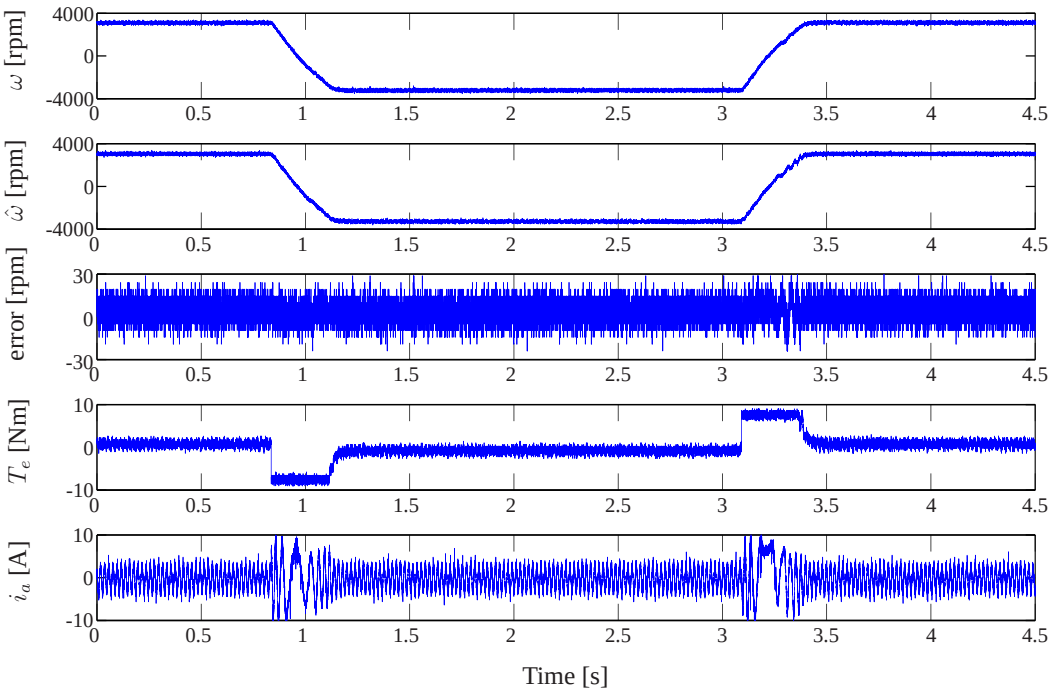

Figure 7.15: Measured speed, estimated speed, speed error, torque and stator current waveforms for the full speed (2772 rpm to -2772 rpm).

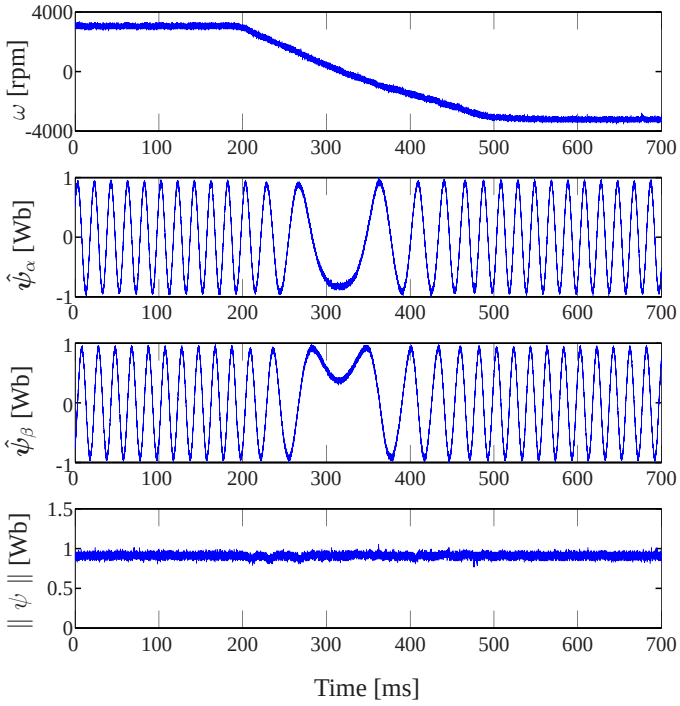

Figure 7.16: Speed, stator flux in α, stator flux in β, magnitude of the stator flux waveforms during a rated speed reversal maneuver.

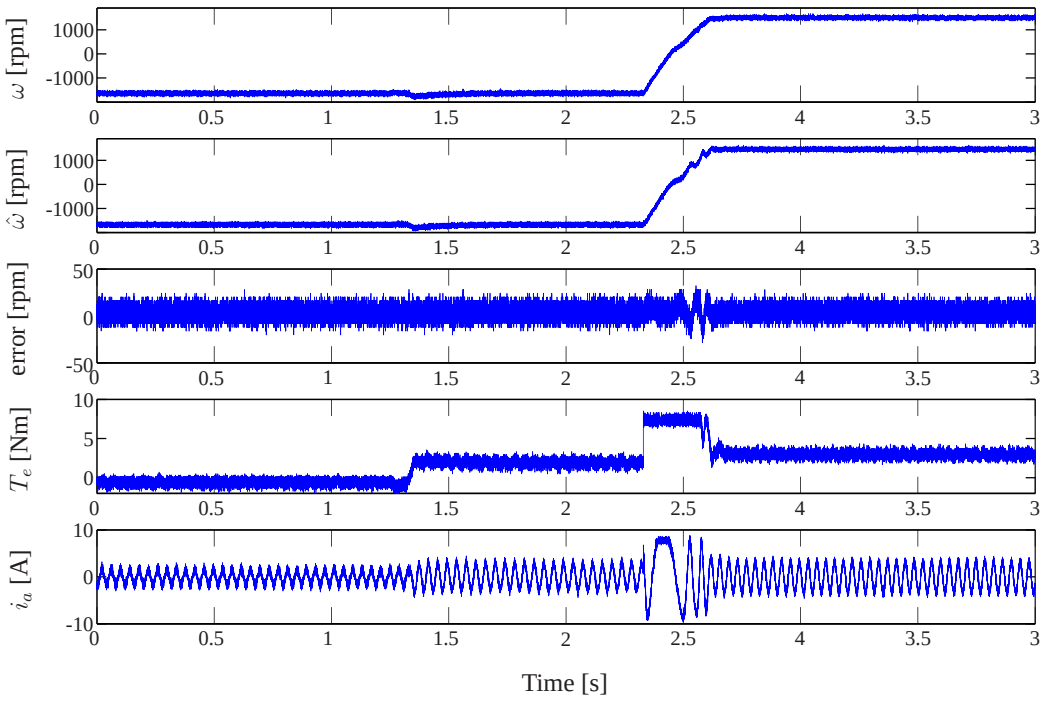

Figure 7.17: Measured speed, estimated speed, speed error, torque and stator current waveforms during a middle speed (1500 rpm) reversal maneuver with a 40 % load impact.

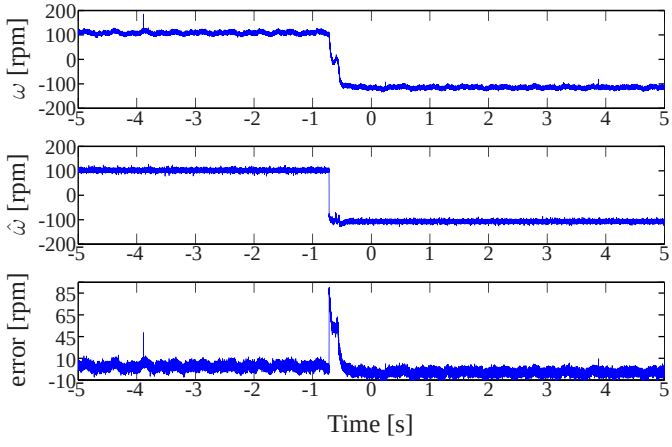

Figure 7.18: Measured speed, estimated speed, speed error waveforms for a low speed (100 rpm) reversal maneuver without load.

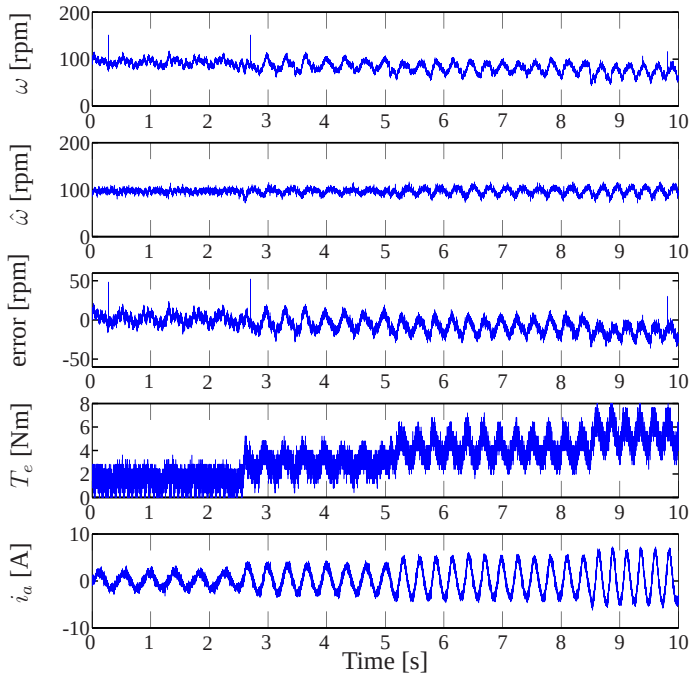

Figure 7.19: Measured speed, estimated speed, speed error, torque and stator current waveforms at low speed (100 rpm) with the variable load (from 20 % to 80 % rated load).

The load impact at a low speed is observed. Fig. 7.19 presents the result of a variable load torque impact to the system at low speed (100 rpm). During the time (0 to 2.5 s), a 1.5 Nm (20 %) load is added to the system. The system is robust with an average speed error: zero. During the time interval (2.5 to 5 s), a 3.0 Nm (40 %) load is added. The average speed error is about 3 rpm. During the time interval (5 to 8.5 s), a 4.5 Nm (60 %) is added. The speed error on average is around 10 rpm. Finally, a 6 Nm (80 %) load is added to the system and leads to a 15 rpm average speed error. Fig. 7.19 also shows the stator current performance during this torque variable process. The value of the current is increasing and the distortion is reducing with the increase of the load torque. It can be seen that increasing the load torque reduces the stability of the system. The reason should be searched in the inf-norm of the uncertainty of the system. when the load torque is increased, the margin of stability is occurred in higher speeds [21].

7.4 Conclusion

An encoderless PTC is proposed and experimentally verified in this work. A compensated MRAS is applied as the observer which outputs not only the estimated speed but also qualified stator and rotor flux. A stator resistance estimator is also included in MRAS. Torque and stator flux are predicted based on the estimated variables and measured stator current. To achieve an accurate predictive model, the offset compensation is taken into account in the same way as in MRAS.

The experimental results show that the compensated MRAS can obtain good stator and rotor flux by eliminating the flux drift phenomenon. The encoderless PTC also reaches very fast dynamics because of the absence of the internal current PI controller. The system works well in full rated speed range and has a good dynamic response with a full load disturbance. In very low speed range (1.0 Hz), the average value of the speed error at steady state is small. However, it is not very good by crossing the zero speed point during a speed reversal process. But it is normal for very low speed with a FS-PTC method, because the IGBTs switching frequency is low and variable and the system does not have good quality of the current THD at speed less than 1.0 Hz.

The proposed encoderless FS-PTC can work well without a speed encoder and it makes PTC more comparable with DTC which is inherently speed sensorless. Especially in traction and steel industries as well as electrical vehicle control applications where torque control is favorable, the encoderless PTC is promising. The variable and the low switching frequency is a problem which leads to not ideal speed estimations at very low frequencies. However, this encoderless FS-PTC mehod keeps the advantages: low cost, simple implementation and fast system dynamics.

CHAPTER 8

EFOSMO based encoderless PTC method

8.1 Introduction

The traditional PTC method for IM applications requires a speed term included in the prediction steps [93]. The predicted stator current values are dependent on the measured or estimated speed [76]. However, the DTC method is inherently encoderless [1]. The simplified block diagrams of the DTC and PTC methods are presented in Fig. 8.2. It is easy to see that the DTC method does not have any speed-dependent term, while the PTC method requires speed term for predictions. On this point, the PTC method cannot be applied as flexibly and reliably as DTC. The speed measurement or speed estimation will certainly reduce the stability of the system due to either the disturbance caused by the speed measurement components or the inaccuracy of the speed estimations [82]. The encoderless model predictive control has been widely investigated [53, 94, 95]. However, in the encoderless FS-PTC method the model of the prediction is speed dependent.

Based on the above investigations and considerations, a novel inherently encoderless PTC method is proposed in this work. The aim of the control strategy is to eliminate the speed component from PTC controller. In this way, the method could have the advantage of the DTC as well as the advantages which are gained purely from the predictive characteristics. To complete the system design, an inherently encoderless observer must be selected and applied. speed estimation is usually the last step of the estimation process, the estimated speed is always affected by cumulative errors. The voltage model observer is one which does not include speed-dependent term and is very easy to implement. However, a known problem for such an open-loop observer is weak robustness and low accuracy [27]. Sliding mode observer

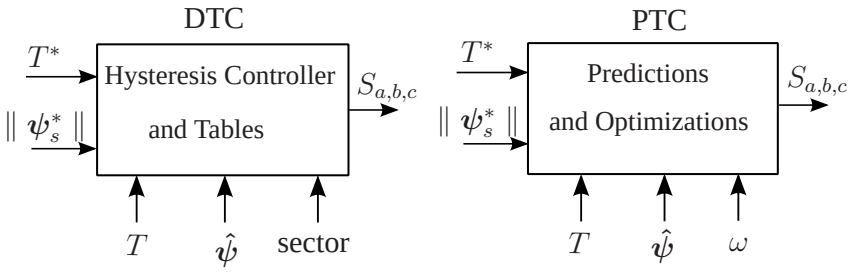

Figure 8.1: Simplified block diagrams of the DTC and PTC methods.

(SMO) is a popular observer [96], which has many merits: disturbances rejection and strong robustness to parameter deviations [91]. Many applications confirmed that SMO is a good and qualified observer [33, 97]. More importantly, SMO makes speed independent design possible [89].

In [89, 98] the inherently encoderless PTC is proposed by using compensated reduced order observer and the full order sliding mode observer (FOSMO) method, respectively. They are investigated only with simulation results. As mentioned, though the reduced order observer is speed inherently, it is lack of accuracy and reliability [27]. In this chapter, an inherently encoderless PTC by using encoderless full order sliding mode observer (EFOSMO) is improved by considering the stator and rotor resistances online identifications and by using a saturation function for relieving the undesirable chattering noise. By using this method the speed term is completely eliminated from prediction and observer models. Like other direct torque control methods, the system is very flexible. When an adjustable-speed drive is required, it is very easy to add an external speed PI controller to produce the torque reference for implementing the speed control. The proposed system is carried out experimently, demonstrating the performance of the adjustable speed and load disturbance.

8.2 Inherently encoderless PTC system

The inherently encoderless FS-PTC method includes two parts: Observer design and FS-PTC design. Both the observer and the FS-PTC must be speed independent. Fig. 8.2 presents the block diagram of the proposed inherently encoderless FS-PTC method. The inputs of the torque control system are torque reference T^* and stator flux reference $\| \vec{\psi}_s^* \|$. The feedbacks of the whole system are the stator voltage $\boldsymbol{v}_s$ and the measured stator currents $\boldsymbol{i}_s$. The function of the inherently encoderless FOSMO is to estimate the flux $\hat{\boldsymbol{\psi}}_r^r(k)$ and $\hat{\boldsymbol{\psi}}_s^r(k)$ and complete the coordinate trans-

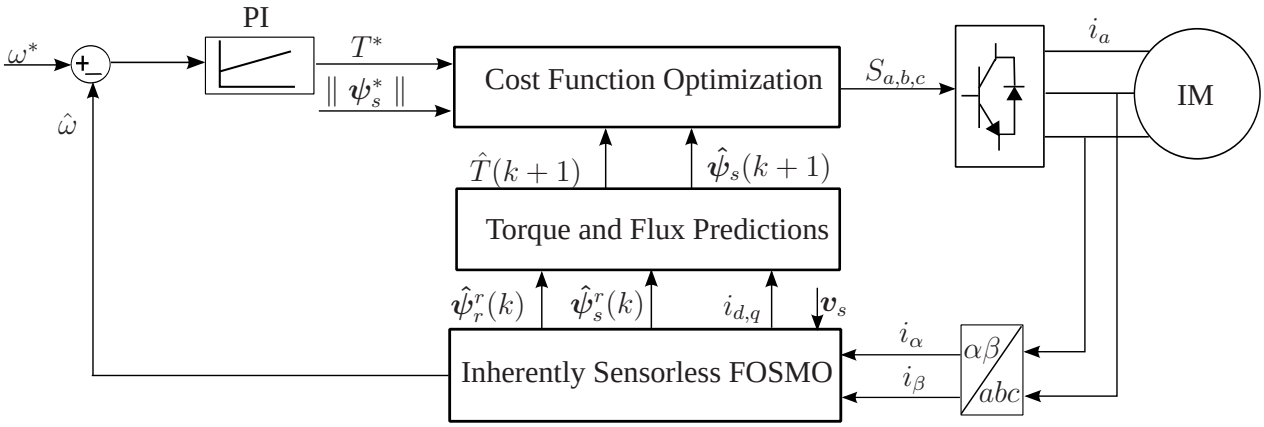

Figure 8.2: Block diagram of inherently encoderless FS-PTC method.

formations with the absence of the estimated speed. The torque $\hat{T}_e(k+1)$ and flux predictions $\hat{\boldsymbol{\psi}}_s(k+1)$ are implemented in synchronous frame and they are speed insensitive. Finally, the cost function is built for the best switching state selection.

8.2.1 Full order sliding mode encoderless observer

The aim of this section is to build an encoderless observer which means that the flux estimations do not need any estimated speed term. Therefore, the estimated speed error will not impact the accuracy of the flux observer. A full-order SMO is selected and it has the merit of the sliding mode theory: strong robustness [91]. In this work, SMO is implemented for IM. According to the IM mathematic model and SMO theory, the full-order SMO could be modeled as:

$$\frac{d}{dt}\hat{\boldsymbol{\psi}}_s = \boldsymbol{v}_s - R_s \cdot \boldsymbol{i}_s + k_1 \cdot sgn(\boldsymbol{i}_s - \hat{\boldsymbol{i}}_s) \tag{8.1}$$

$$\hat{\boldsymbol{i}}_s = \frac{1}{L_\sigma^2} \cdot (L_r \cdot \hat{\boldsymbol{\psi}}_s - L_m \cdot \hat{\boldsymbol{\psi}}_r) \tag{8.2}$$

$$\frac{d}{dt}\hat{\boldsymbol{\psi}}_r = \frac{L_m}{\tau_r} \cdot \boldsymbol{i}_s - \frac{1}{\tau_r} \cdot \hat{\boldsymbol{\psi}}_r + j \cdot \hat{\omega} \cdot \hat{\boldsymbol{\psi}}_r + k_2 \cdot sgn(\boldsymbol{i}_s - \hat{\boldsymbol{i}}_s). \tag{8.3}$$

The sliding surface is constructed by using the current error between the measured and the estimated current $\boldsymbol{i}_s - \hat{\boldsymbol{i}}_s$. The sgn function is component-wise applied for $\boldsymbol{i}_s - \hat{\boldsymbol{i}}_s$. To reduce the undesirable chattering problems caused by the sign function,

a saturation function is applied [13] and is defined as:

$$Sat(x) = \begin{cases} -1 & \textit{if } x - \hat{x} < \Delta, \\ (x - \hat{x})/\Delta & \textit{if } |x - \hat{x}| < \Delta, \\ 1 & \textit{if } x - \hat{x} > \Delta. \end{cases} , \tag{8.4}$$

where $x = i_\alpha$ and i_β, Δ is a tuning parameter.

In the applied FOSMO, k_1 and k_2 are the gains of the observer. It is noted that (6) is based on the voltage model observer. Normally the voltage model observer has flux drift phenomenon and DC offset. For removing drifts, compensating the offset and reducing chattering problems, the PI dynamics are included in the design. By considering the same parameters tuning method introduced in [92], the coefficient k_1 is defined by using a PI controller:

$$k_1 = k_{1p} + \frac{k_{1i}}{s} \tag{8.5}$$

k_2 is set as:

$$k_2 = k_{21} + j \cdot k_{22} \tag{8.6}$$

where k_{1p} and k_{1i} are PI gains; k_{21} and k_{22} are sliding mode gains.

The described FOSMO could work for the flux estimation. However, the aim is to design an inherently encoderless observer. According to the mentioned model, (8.1) and (8.2) are speed independent but rotor flux model (8.3) does have a speed term which cannot satisfy the requirement. Define (8.3) in synchronous frame and take into account that the imaginary component of (8.3) is zero. Then a new rotor flux model which only includes the real component can be described:

$$\frac{d}{dt}\hat{\boldsymbol{\psi}}^r_{rd} = \frac{L_m}{\tau_r} \cdot \boldsymbol{i}^r_{sd} - \frac{1}{\tau_r} \cdot \hat{\boldsymbol{\psi}}^r_{rd} + Re\left\{k_2 \cdot Sat(\boldsymbol{i}_s - \hat{\boldsymbol{i}}_s) \cdot e^{-j\cdot\hat{\theta}_r}\right\} \tag{8.7}$$

Where $\hat{\theta}_r$ is the coordinate transformation angle $\arctan(\frac{\hat{\psi}_{r\beta}}{\hat{\psi}_{r\alpha}})$. And in stator reference, the rotor flux $\vec{\hat{\psi}}_r$ is:

$$\hat{\boldsymbol{\psi}}_r = \frac{1}{L_m}(L_r \cdot \hat{\boldsymbol{\psi}}_s - L_\sigma^2 \cdot \boldsymbol{i}_s) \tag{8.8}$$

By combining (8.1), (8.2) and (8.7) the new encoderless FOSMO (EFOSMO) is built. It does not employ any rotor speed adaptation. Therefore, the applied EFOSMO is insensitive to speed estimation errors.

8.2.2 Inherently encoderless states prediction

As a FS-PTC method, the electromagnetic torque $T_e(k+1)$ and the stator flux $\boldsymbol{\psi}_s(k+1)$ must be predicted. It must be mentioned that the conventional FS-PTC methods use the electrical speed for states predictions [99], which means that the accuracy of the prediction is dependent on the measured or estimated speed. In this section, the aim is to build an encoderless prediction model by removing the speed term.

In the next step, in synchronous reference frame, stator flux $\vec{\psi}_s(k+1)$ can be calculated:

$$\hat{\boldsymbol{\psi}}_s^r(k+1) = \hat{\boldsymbol{\psi}}_s^r(k) + T_s[\boldsymbol{v}_s^r(k) - R_s \cdot \boldsymbol{i}_s^r(k) + k_1 \cdot Sat(\boldsymbol{i}_s^r(k) - \hat{\boldsymbol{i}}_s^r(k))] \quad (8.9)$$

where T_s is the sampling interval. The angle for coordinate transformation ($\alpha - \beta$ to $d-q$) is described in the last sub-section. The same sliding mode function as introduced in the observer is applied towards an accurate prediction model.

To predict the electromagnetic torque $T(k+1)$, the IM mathematic model is used and is considered in synchronous frame:

$$\hat{T}(k+1) = \frac{3}{2} \cdot p \cdot Im\{\hat{\boldsymbol{\psi}}_s^r(k+1)^* \cdot \hat{\boldsymbol{i}}_s^r(k+1)\}. \quad (8.10)$$

In torque prediction, the predicted stator current $\boldsymbol{i}_s^r(k+1)$ is necessary. Consider current predictions in $d-q$ reference, in this reference, the stator rotor imaginary component is zero. As proved in the appendix, the current predictions can be described as following:

$$\hat{\boldsymbol{i}}_{sd}^r(k+1) = A \cdot \hat{\boldsymbol{\psi}}_{sd}^r(k+1) - (B - C \cdot T_s) \cdot \hat{\boldsymbol{\psi}}_{rd}^r(k) - T_s \cdot D \cdot \hat{\boldsymbol{\psi}}_{sd}^r(k) \quad (8.11)$$

$$\hat{\boldsymbol{i}}_{sq}^r(k+1) = A \cdot \hat{\boldsymbol{\psi}}_{sq}^r(k+1) \quad (8.12)$$

where $A = \dfrac{L_r}{L_s \cdot L_r - L_m^2}$, $B = \dfrac{L_m}{L_s \cdot L_r - L_m^2}$, $C = \dfrac{1}{\sigma \cdot \tau_r}$ and $D = B \cdot \dfrac{L_m}{\sigma \cdot L_s \cdot \tau_r}$.

8.2.3 Torque operation mode controller design

The cost function is very flexible and can handle system constraints. It should be designed according to the specific control goals. The cost function includes three

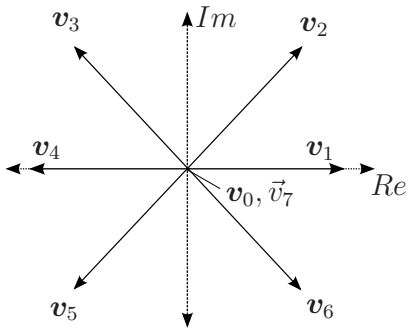

Figure 8.3: Voltage vectors of two-level voltage source inverter.

terms: Torque error, stator flux error and overcurrent protection:

$$\begin{aligned} g_i = \sum_{h=1}^{N} \{ & |T^* - \hat{T}(k+h)_i|^2 + \lambda \cdot | \parallel \boldsymbol{\psi}_s^* \parallel \\ & - \parallel \hat{\boldsymbol{\psi}}_s(k+h)_i \parallel |^2 + I_m(k+h)_i \} \end{aligned} \tag{8.13}$$

The torque reference T^* is either a constant in direct torque control operation or by an external speed PI-controller for speed-adjustabe drives. The coefficient λ denotes the weighting factor which weights the relative importance of the electromagnetic torque versus flux control.

The overcurrent protection term is actived when the absolute value of the predicted current is higher than its limit. The current limitation is defined as:

$$I_m(k+h) = \begin{cases} 0 & \textit{if } |i(k+h)| \leq |i_{\max}|, \\ \gamma >> 0 & \textit{if } |i(k+h)| > |i_{\max}|. \end{cases} \tag{8.14}$$

where $|i(k+h)| = \sqrt{i_\alpha^2(k+h) + i_\beta^2(k+h)}$.

In the cost function h ($h = 1, 2 \cdots$) is the prediction horizon. i denotes the index of applied voltage vector for the prediction. As a two-level voltage source inverter is applied, there are in total 8 different switching states as described in Fig. 8.3.

For the conventional FS-PTC method all switching states must be considered in one sampling interval. In this case $i = 0...7$, which means that the cost function must be calculated 8 times with a one-step prediction ($N = 1$) for selecting the best switching state. The cost function at time instant k+1 will be calculated corresponding to the 8 inverter switching states from 000 to 111.

8.2.4 Adjustable-speed drive

In many instances the adjustable-speed drive is required. Based on the proposed inherently encoderless FS-PTC method, it is very easy to add a speed control loop.

To realize a speed control, both speed reference ω^* and the estimated speed $\hat{\omega}$ are required. The applied FOSMO can estimate the rotor speed, but the estimated rotor speed does not inject into either FOSMO or the prediction model. This means the FOSMO can output the estimated speed but this output does not affect the accuracy of the flux estimation.

The ω^* is calculated as the difference between the rotor flux speed and the slip speed:

$$\hat{\omega} = \frac{\hat{\psi}_{r\alpha}(k-1) \cdot \hat{\psi}_{r\beta}(k) - \hat{\psi}_{r\beta}(k-1) \cdot \hat{\psi}_{r\alpha}(k)}{T_s \cdot \hat{\psi}_r^2(k)} - \frac{2R_r}{3p} \cdot \frac{\hat{T}_e(k)}{\hat{\psi}_r^2(k)} \tag{8.15}$$

The torque reference T_e^* is generated by means of a speed PI controller.

$$T_e^* = k_p \cdot (\omega^* - \hat{\omega}) + k_i \int (\omega^* - \hat{\omega}) dt \tag{8.16}$$

where k_p and k_i are gains of the PI modulator. There is no internal current PI control for system, the inner loop of PTC method is very fast and allows it to increase the bandwidth of the outer speed loop without interference. Therefore, the speed PI controller can reach very fast dynamics.

8.2.5 Influence of parameter variation

Parameters of the motor can be measured. However, it is hard to use the correct parameters, because they can vary with the motor work conditions such as motor temperature. From the observer it can be seen that the accuracy of the observer could be influenced by detuning of magnetizing inductance L_m, resistance R_s and R_r. The sensitivity to parameter detuning is investigated using simulations. Because in the cost function the torque and the stator flux are controlled, the predicted and actual values of the torque and the flux are observered during the parameter variations. In Fig. 8.4 the predicted and measured torque, the predicted and measured stator flux magnitude over the variations of L_m are observered. The speed reference is 200 rpm and the motor starts up at time instant ($t = 0$) with the real value (0.275 mH). At time instant ($t = 0.3\ s$) the L_m decreases with a $30.0\ \%$ magnitude. From the picture, with this variation the measured torque T is influenced by the variation of L_m. A obvious oscillation can be seen. Howeer, the stator flux magnitude and predicted torque are not impacted. In Fig. 8.5, system stability

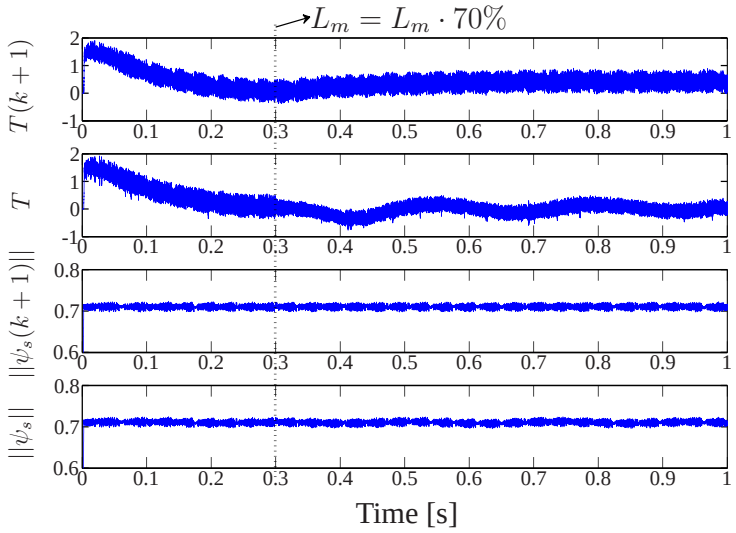

Figure 8.4: Predicted and measured torque, predicted and measured stator flux magnitude waveforms with a L_m variation (-30$\%$).

over the variation of stator resistance is observered. At time instant ($t = 0.3\ s$) R_s increases with a $30.0\ \%$ magnitude. The predicted values are not impaceted due to the values in controller are kept. Both measured torque and measured stator flux magnitude are influenced by this variation. The reason can be found from the stator flux estimation equation. The stator resistance is an important parameter for stator observation, especially at low speed range. The influence of rotor resistance with a $60.0\ \%$ variation is also investigated. The simulations confirm that the change of R_r has almost neglected influence on the system observations. The simulations have also verified that bigger variations of L_m, R_s and R_r have more influence on the system stability.

The stator and rotor resistances are not constants with the varying of the temperature. The simulations have verified that system is almost not sensitive to the rotor resistance detuning but is sensitive to stator resistance errors. In this work, the stator resistance is estimated [91] as following:

$$\hat{R}_s = R_s - k_{rs} \int Im(\hat{\psi}_r^* \cdot Sat(i_s^r - \hat{i}_s^r))dt, \tag{8.17}$$

where the k_{rs} is the gain for the stator resistance estimation.

Considering the similar thermal behavior of stator and rotor resistance, it can be assumed that the rotor resistance varies in a fixed ratio as the estimated stator resistance varies [30]. $\hat{R}_r$ can be estimated as:

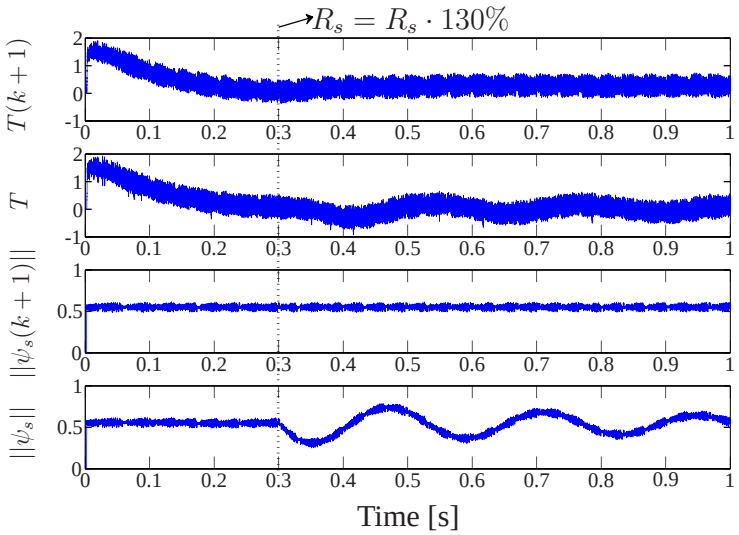

Figure 8.5: Predicted and measured torque, predicted and measured stator flux magnitude waveforms with a stator resistance variation (+30%).

$$\hat{R}_r = R_r + k_{rr} R_r \frac{\hat{R}_s - R_s}{R_s} \tag{8.18}$$

where R_r is the initial measured value and k_{rr} is a constant for tuning the ratio between stator and rotor resistance.

8.2.6 Theoretical analysis of the encoderless system

To clarify the difference between the proposed system and the traditional method, Fig. 8.6 is presented. In traditional encoderless PTC, FOSMO needs the injection of the estimated speed $\hat{\omega}_e$. It means that the errors generated by either $\hat{\omega}_r$ or $\hat{\omega}_{slip}$ will influence the accuracy of the estimated stator and rotor flux $\hat{\boldsymbol{\psi}}_{s,r}$. Also, the prediction model takes $\hat{\omega}_e$ as a variable. Flux prediction $\hat{\boldsymbol{\psi}}_{s,r}$(k+1) and stator current prediction $\hat{\boldsymbol{i}}_s$(k+1) rely on it.

In the proposed encoderless prediction model and EFOSMO system, the estimated rotor electrical speed $\hat{\omega}_e$ is injected neither into EFOSMO nor into prediction model. From the diagram, it can be seen the estimation of $\hat{\omega}_e$ is the last step of the estimation process, which means that $\hat{\omega}_e$ includes the accumulated noise and errors. When this inaccurate estimate is fed back to the observer, the flux estimation accuracy deteriorates [67]. The same situation can be seen for the prediction model. From the view of this point the proposed encoderless prediction model and

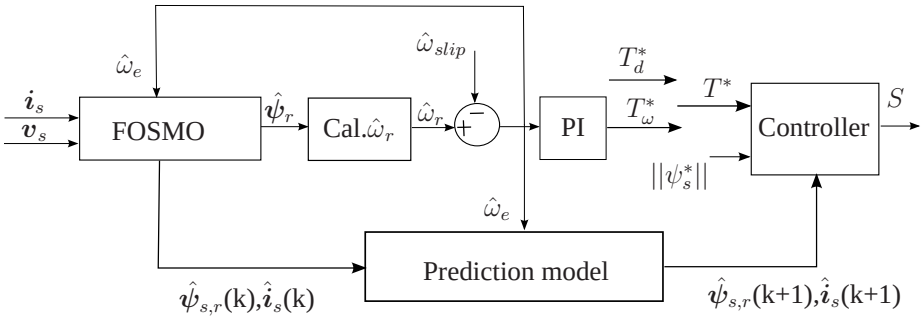

(1) Traditional prediction model and FOSMO

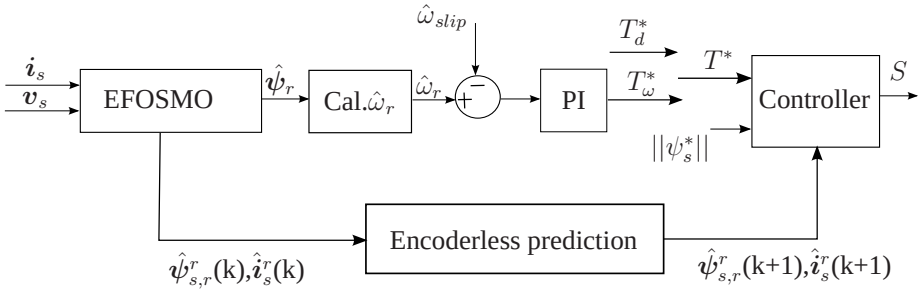

(2) Encoderless prediction model and EFOSMO

Figure 8.6: Structure of the encoderless PTC: (1) traditional prediction model and FOSMO; (2) encoderless prediction model and EFOSMO.

EFOSMO system have advantages compared with the traditional one. The system can also work in direct torque mode, which means that torque reference can be set as a fixed value T_d^*. Therefore, the predictive direct torque control method does not need the $\hat{\omega}_e$ for speed PI controll to generate T_ω^*. With predictive direct torque control operation, the proposed system does not need the calculation of $\hat{\omega}_e$, which is only necessary for adjustable-speed drives. .

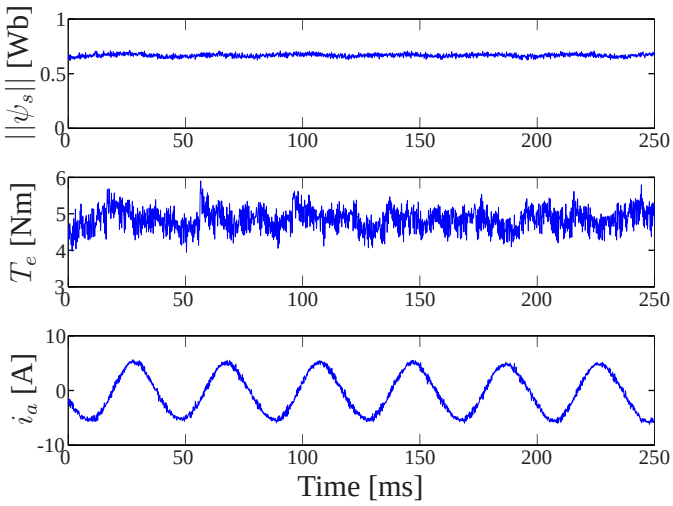

Figure 8.7: Stator flux magnitude, torque and stator current waveforms at steady state (1500 rpm, 5 Nm load).

8.3 Experimental results and analysis

8.3.1 Experimental results

Like other direct torque control methods, the proposed inherently encoderless FS-PTC method can work by directly using torque and stator flux reference, which makes the external speed PI controller absent. However, as a completed system, adjustable-speed application is very important. The first test is to verify the system performance at steady state. The motor rotates at 1500 rpm with a 5 Nm load. Fig. 8.7 shows the stator flux magnitude, torque and the stator current waveforms. The system shows very good behavior in steady state. The torque ripple is lower than 1.5 Nm and the calculated current THD is about 3.5 $\%$.

The second test is developed to observe the system performance in the whole speed range. The flux reference is set to be a constant 0.71 Wb. The weighting fact of the cost function is calculated by considering the electromagnetic torque and flux control to be of equal relative importance. The calculated value is 10.7. Fig. 8.8 shows the measured speed, the estimated speed, the stator current and the torque performance during the full rated speed reversal process. The result shows that the proposed method can work in full speed range. During the transient stage (2772 rpm to -2772 rpm), the electromagnetic torque reaches -7.5 Nm, which is the maximum value generated by speed PI controller, and is also the rated torque of

the motor. During the transient stage (-2772 rpm to 2772 rpm), the electromagnetic torque keeps at 7.5 Nm for achieving the fastest dynamic process. A very important advantage of the FS-PTC is fast torque dynamics. These fast dynamics are due to the absence of both the inner current PI controller and a modulator. To verify this feature, a torque step test is developed. Fig. 8.9 presents the torque response and switching signals during this process. In the picture, switching 0 means 000, switching 1 means 001 ... switching 7 means 111. The torque step is generated by a sudden change of torque reference. In this test, torque reference changes from 2.0 Nm to 7.5 Nm (rated torque). From the picture, it can be seen that the dynamics are very fast: 0.2 ms. Before and after the torque step, the switching changes, among all available switching states, from 0 to 7. During the torque step process, only active switching signals (switching 1 and 3) are selected. This is the reason for a fast settling time. To evaluate the accuracy of the speed estimation in the rated speed reversal process, the speed error between the measured speed and the estimated speed is calculated as: $\Delta\omega = \frac{\omega - \hat{\omega}}{\omega} * 100\%$. Fig. 8.10 shows the speed error $\Delta\omega$. The value is high during the transient stage because of crossing the low speed region, including the zero speed. At steady state the mean value of $\Delta\omega$ is 0.5 $\%$.

The system performance in low speed range (2.0 $\%$ of the nominal speed) is observed. Fig. 8.11 presents the measured speed, the estimated speed, the stator current and the torque waveforms during the low speed (60 rpm) reversal maneuver. From the picture, it can be seen that the system can track the speed robustly. Fig. 8.12 shows the speed error $\Delta\omega$. At this low speed reference, the mean value of $\Delta\omega$ at steady state is 3.0 $\%$. During the transient stage, the system crosses lower speed range. A high index of $\Delta\omega$ is generated.

Fig. fig:loaddisturbanceismo presents the performance over a full rated load disturbance. The measured speed, the estimated speed, the stator current and the electromagnetic torque are shown in the picture. The motor rotates at a rated speed. A 7.5 Nm full load is suddenly added to the system. From the picture, it can be concluded that the system has a good response over a load disturbance. At steady state, it works almost the same as shown in Fig. 8.8. The speed error $\Delta\omega$ is presented in Fig. 8.14. During the transient stage, the value is a little bit high. At steady state, the index is almost the same as in the full speed reversal test: The mean value of $\Delta\omega$ is 0.5 $\%$.

8.3.2 Implementation Analysis

In the adjustable-speed drive tests, the system can track both low speed and high speed references well. However, during the transient the speed error $\Delta\omega$ is high.

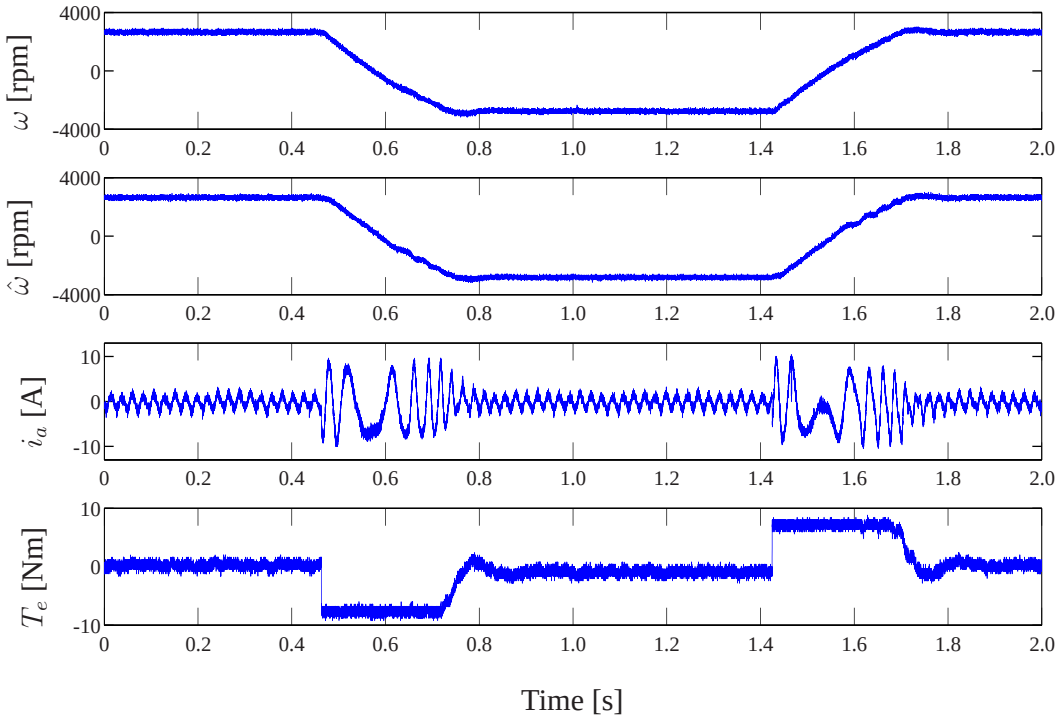

Figure 8.8: Speed, estimated speed, stator current and torque response during a rated speed reversal maneuver.

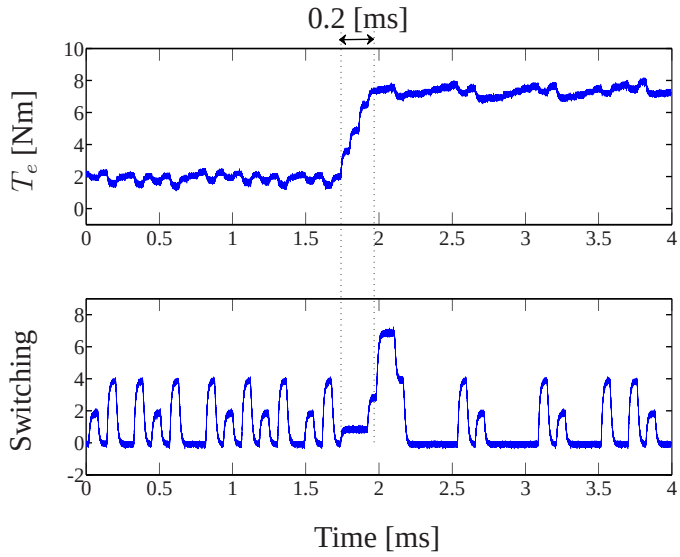

Figure 8.9: Torque response and switching signals during a torque step.

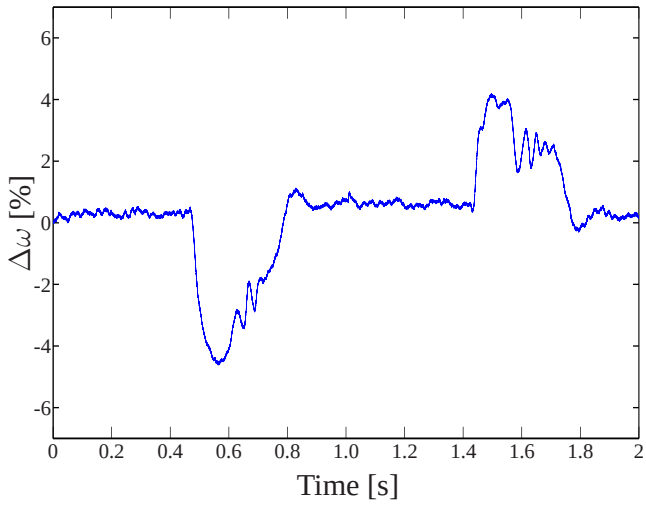

Figure 8.10: Speed error during a rated speed reversal maneuver.

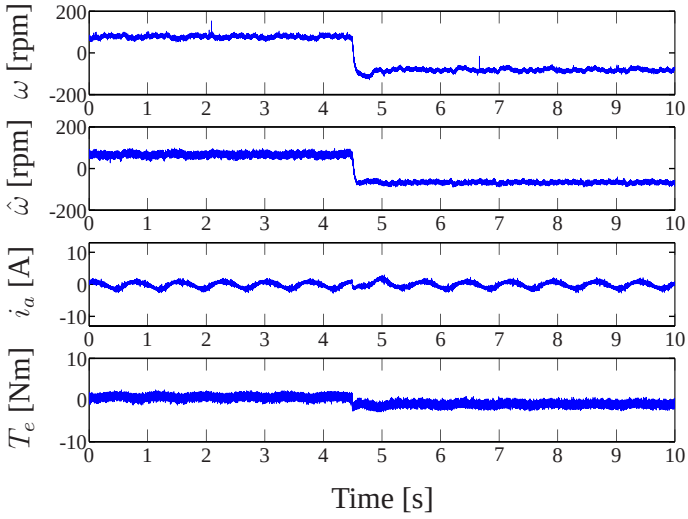

Figure 8.11: Speed, estimated speed, stator current and torque response during a low speed (60 rpm) reversal process.

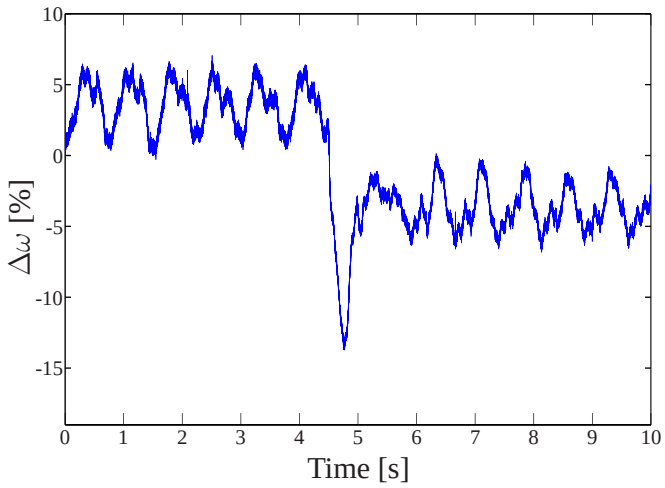

Figure 8.12: Speed error during a low speed (1.0 Hz) reversal process.

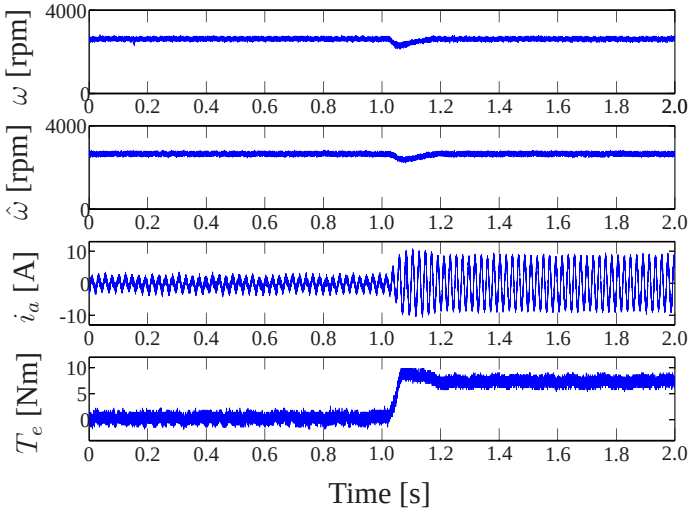

Figure 8.13: Speed, estimated speed, stator current and torque response during a full load disturbance.

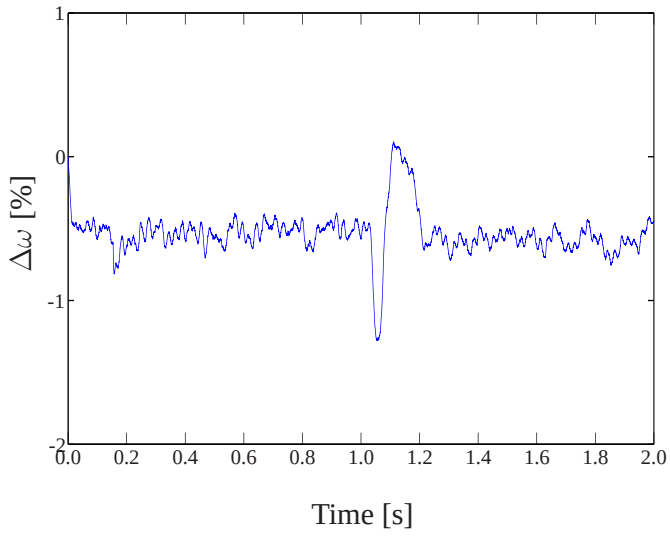

Figure 8.14: Speed error during a 100 % load torque disturbance.

Also the $\Delta\omega$ at low speed (60 rpm) is much bigger than that at high speed reference. By observing the current total harmonic distortion (THD), it is possible to explain the big speed error phenomenon. A test regarding current THD is developed for the FS-PTC method with a speed encoder. At the low speed of 60 rpm, the current THD is very big: 41.07 $\%$. Especially in the low speed range, from equation (8.1), it is easy to see that the measured current affects the flux estimation very much. The FS-PTC method does not have an invariable switching frequency because of the absence of a modulator. At rated speed, the average switching frequency of each IGBT is about 2.9 kHz and results in a current THD: 14 $\%$. At 60 rpm, the average switching frequency is around 1.0 kHz and leads to a current THD: 41.07 $\%$. Therefore, compared to FOC method and the DTC method, which uses SVM, the PTC method exhibits a worse current THD due to its lack of an invariable switching frequency. A possible approach to get a better THD is to increase the sampling frequency.

However, with the absence of a modulator and the absence of the internal current PI controller, the system becomes simpler and the PTC method reaches very fast dynamics as shown in the torque step test. When the fast dynamics and middle or high speed working range are expected, the inherently encoderless PTC method can be a very good alternative strategy.

The proposed method resulted in a better performance compared to encoderless PTC method with H-inf calculated feedback gains [53]. The problem of uncertainty injected from calculated speed is solved by this inherently encoderless method.

Therefore, the proposed method is more stable in low speed performance and shows better THD.

8.4 Conclusion

A novel inherently encoderless PTC method is proposed in this chapter. Both the controller and the observer are speed independent. The EFOSMO is applied to estimate the flux values, which are required for state predictions. An inherently speed independent state predictor is developed and utilized. An optimization cost function is designed to select the best switching signal. An external speed PI controller can easily be added to implement the adjustable speed control. To reduce the chattering problem of the SMO, a saturation function is used instead of the sign function. The stator and the rotor resistances online identifications are used for improve the robustness of the system.

The adjustable speed control is tested and analyzed in this work. Experimental results verify that the system works well. The proposed strategy reaches very fast dynamics due to the absence of the internal current PI controller compared to the FOC, and it works well in the full speed range. It also has a good response over a 100 $\%$ rated load torque.

The proposed system is insensitive to the estimated speed errors. This advantage further enhances the competitive features of the PTC method. Specifically, it achieves the main advantage of the DTC method which is inherently encoderless application. The future work will consider an optimization algorithm to reduce the calculation time for a short sampling interval. In this way, the quality of the measured current will be improved and the average of switching frequency can be increased; both of these aspects are important for the performance improvement of the inherently encoderless FS-PTC implementation. The work is accepted for publication [100].

CHAPTER 9

Summary and future prospects

In this dissertation, different predictive control strategies in the field of electrical drives are invesitgated in chapter 3. Predictive control can be classified into three main categories: hysteresis- and trajectory-based predictive control and MPC. FCS-PTC method is one of the MPC methods. Compared to the continuous MPC, FCS-PTC has advantages of absence of a modulator and easier concept understanding. As a promising control method, FCS-PTC method has been investigated widely in the field of electrical drive system.

In chapter 4 and 5, FCS-PTC method is applied into PMSM and IM with a two-level voltage source inverter. The method has a straightforward algorithm structure, which makes it easy to implement. FCS-PTC is compared experimentally to the traditional popular method: DTC method. The two methods have the same feature: absence of a modulator, fast dynamics. In experiments, FCS-PTC method shows even better behavior regarding the torque ripple both in steady state and in transient state. They produced very similar stator current THD in steady state with a half load. When the complex of the system is disscussed, FCS-PTC has advantages of less parameters and flexibility of the cost function design. FCS-PTC method needs bigger calculation time. Fortunately, this drawback becomes lightly due to the development of FPGAs and DSP. Two methods have good robustness regarding to a variation of rotor resistance. However, the DTC method is inherently encoderless which means the controller will be not impacted by the error of the estimated or measured rotor speed. From the point of this view, DTC has an advantage. Gererally speaking, FCS-PTC method shows very strong alternative for the motor control.

A future work is to test the FCS-PTC method by using a multi-level inverter, with which a look-up table for DTC method is much more complicated than that

with a two-level voltage source inverter. However, for FCS-PTC method, it still has a straightforward algorithm. It can calculate all possible voltage vectors generating by a multi-level voltage inverter but absolutelly more calculation time. Therefore, a reduced calculation time algorithm has to be considered. It can be predicted that the application of FCS-PTC method for a multi-level inverter will show big advantages compared with the DTC method regarding the complex of the algorithm and implementations.

Chapter 6 proposes a two-step FCS-PTC by considering a maximum one switching transition in a sampling instant. This method solved a problem of calculation effort for a two-step prediction horizon. With this idea, a two-step PTC only has calculation effort of $4^2 = 16$ times of the loop, which is much smaller than the original way ($7^2 = 49$). Furthermore, it reduces the switching frequency of the IGBTs, which can decrease the losses of the inverter, especially for some high-voltage applications. However, with a longer prediction horizon (> 3) which needs a $4^3 = 64$ times of calculation loop, it does not work. The only way is to increase the sampling time, which will absolutey reduce the quality of the measured currents.

A future work could be to find a better solution for long prediction horizon based PTC method. However, longer horizon does not absolutely mean the better performance. The accuracy of the prediction model is very essential. An unaccurate prediction model will results in even a worse results for long prediction horizon. Therefore, some online parameter identifications must be included when a very long prediction horizon is used.

Encoderless applications of FCS-PTC method have been discussed in chapter 7 and 8. MRAS system is approved to be a good observer for PTC system. However, it must be compensated for better flux in estimation quality. A traditional compensation method which considers the inverter parameter and a SMO compensation method are investigated. The disadvantage of the former one is the need of an accurate inverter model. The draw of the latter method is the chattering problem injected by the SMO. Experimental results verify that the observers can adapt the PTC system very well. However, FCS-PTC has a disadvantage: the prediction model relies strongly on the measured or estimated speed. It means it is not an inherently encoderless method which is a feature of the DTC method. To overcome this problem, the system is considered in the synchronous reference frame and an encoderless FOSMO is developed. The new designed system has not only an encoderless prediction model but also an encoderless observer, which make the system speed independent. Furthermore, the influence of the parameters variations, i.e., stator resistance and mutual inductance, is analzed with simulations. The parameters variation can make system unstable. A stator resistance online identification method is considered in the work. The experimental results show that this inher-

ently encoderless PTC method can work in a wide range of the speed. However, it does not show very good performance at very low speed range. The reason could be found by observing the current THD at low speeds. Because of the low and variable frequency, the observer is very hard to estimate the flux accurately. Some possible solutions are improving sampling frequencies and by considering a SVM for PTC method.

A future work could develop a comprehensive study based on different model-based observers, i.e., LO, EKF, MRAS and SMO. The aim is to find the most appropriate observer for FCS-PTC method. Since an advantage of the FCS-PTC method is its intuitive and straightforward feature, the complex of an observer will be an important criterion for the comparison. The accuracy of the estimated speed and fluxes is essential to the encoderless PTC method. The accurate estimated variables can guarantee not only the relibility of the prediction model but also the control accuracy.

The above efforts show that the MPC method is emergering as a powerful alternative control method in electrical drives. For FCS-PTC method with- and without an encoder, different cost functions are developed and applied. However, how to build a formal cost function and to find the weighting factors when the cost function considers more than two control variables are still an open question. Also, the performance of PTC method in field weakening condition needs to be investigated in future.

APPENDIX A

List of publications

A.1 Journal papers

- F. Wang, Z. Zhang, S. A. Davari, D. A. Khaburi, J. Rodriguez and R. Kennel, An Encoderless Predictive Torque Control for an Induction Machine with a Revised Prediction Model and EFOSMO, *Industrial Electronics, IEEE Transactions on*, 2014. (**accepted**)
- F. Wang, Z. Chen, P. Stolze, J. -F. Stumper, J. Rodriguez and R. Kennel, Encoderless Finite-State Predictive Torque Control for Induction Machine with a Compensated MRAS, *Industrial Informatics, IEEE Transactions on*, 2014.(**accepted**)
- F. Wang, Z. Zhang, R. Kennel and J. Rodriguez, Model predictive torque control with an extended prediction horizon for electrical drive systems, *Internation Journal of Control*, 2014. (**Invited paper**)
- F. Wang, Z. Chen, M. Trincado, P. Stolze, J. Rodriguez and R. Kennel, High Performance Control Strategies of Electrical Drives: an Evaluation of DTC and FCS-PTC, *EPE Journal*, 2014. (**under review**)
- F. Wang, S. A. Davari, J. Rodriguez and R. Kennel, Using a Sliding Mode MRAS for Encoderless Predictive Torque Control of an Induction Machine, *IEEE trans. on Industrial Applications*, 2013. (**in preparation**)
- S. A. Davari, D. A. Khaburi, F. Wang and R. Kennel, Using Full Order and Reduced Order Observers for Robust Sensorless Predictive Torque Con-

trol of Induction Motors, *Power Electronics, IEEE Transactions on*, 2012. (**published**)

- S. A. Davari, D. A. Khaburi, F. Wang and R. Kennel, Robust Sensorless Predictive Control of Induction Motors with Sliding Mode Voltage Model Observer, *Turkish Journal of Electrical Engineering and Computer Sciences*, 2013.(**published**)

A.2 Conference papers

- Z. Chen, F. Wang, P. Stolze and R. Kennel, Using Compensated MRAS for Model Predictive Control of Induction Machine, *Power Eletronics and Applications (EPE), 15th*, 2013.
- Z. Zhang, C. Hackl, F. Wang, C. Zhe and R. Kennel, Encoderless Model Predictive Control of Back-to-Back Converter Direct-Drive Permanent magnet Synchronous Generator Wind Turbine Systems, *Power Eletronics and Applications (EPE), 15th*, 2013.
- W. Xie, F. Wang, X. Wang, G. Dajaku, D. Gerling and R. Kennel, Analysis of High Efficiency and Low Cost Drive System of IPMSM by Using two-step Model Predictive Torque Control, *Control Conference (CCC), 32nd Chinese*, 2013.
- S. A. Davari, D. A. Khaburi, F. Wang and R. Kennel, Robust Sliding Mode Voltage Model Observer for Sensorless PTC of Induction Motors, *Power Electronics and Drive Systems Technology (PEDSTC), 3rd*, 2012.
- F. Wang, P. Stolze, S. A. Davari, D. A. Khaburi, J. Rodriguez and R. Kennel, Speed-Independent FCS-Model Predictive Torque Control for IM based on SMO, *EPE-PEMC, 15th*, 2012.
- F. Wang, P. Stolze, S. A. Davari, D. A. Khaburi, J. Rodriguez and R. Kennel, Inherent FCS-Model predictive torque control for induction machine without Encoder , *SPEEDAM, 15th*, 2012.
- F. Wang, S. A. Davari, D. A. Khaburi, J. Rodriguez and R. Kennel, Sensorless model predictive torque control for induction machine by using the sliding mode full-order observer , *SLED*, 2011.

APPENDIX B

Experimental setup

The induction machin test bench is shown in Fig. B.1. It consists of two 2.2 kW squirrel-cage induction machines. One machine, driven by a Danfoss VLT FC-302 3.0 kW inverter, is used as load machine. The main machine is driven by a modified SERVOSTAR620 14 kVA inverter which provides full control over the IGBT gates. A self-made 1.4 GHz real time computer system is used. The rotor position is measured by a 1024 points incremental encoder. The parameters of the main motor are given in Table B.1. The test bench is shown in Fig. B.1.

The IPMSM test bench is shown in Fig. B.2. It consists of an IPMSM driven by an inverter which provides full control IGBT gates, and a DC motor as a load machine. The test bench has a DC electrical source, which makes the tests possibly with different power source. The motor temperature can be observered by a temperature monitor and power meter helps the analysis of the efficiency alalysis. The actual torque can be directly measured on this test bench. The parameters of the main motor are given in Table B.2. The test bench is shown in Fig. B.2.

Parameter	Value
DC link voltage V_{dc}	582 V
Rs	2.68 Ω
Rr	2.13 Ω
Lm	275.1 mH
Ls	283.4 mH
Lr	283.4 mH
p	1.0
ω_{nom}	2772.0 RPM
T_{nom}	7.5 Nm
J	0.005 Kg/m^2

Table B.1: PARAMETERS OF THE INDUCTION MACHINE

Parameter	Value
DC link voltage V_{dc}	12 V
Rs	0.018 Ω
Ld	275.1 mH
Lq	283.4 mH
ψ_{pm}	0.007 Vs
p	5
ω_{nom}	1000.0 RPM
T_{nom}	2.0 Nm

Table B.2: PARAMETERS OF THE IPMSM

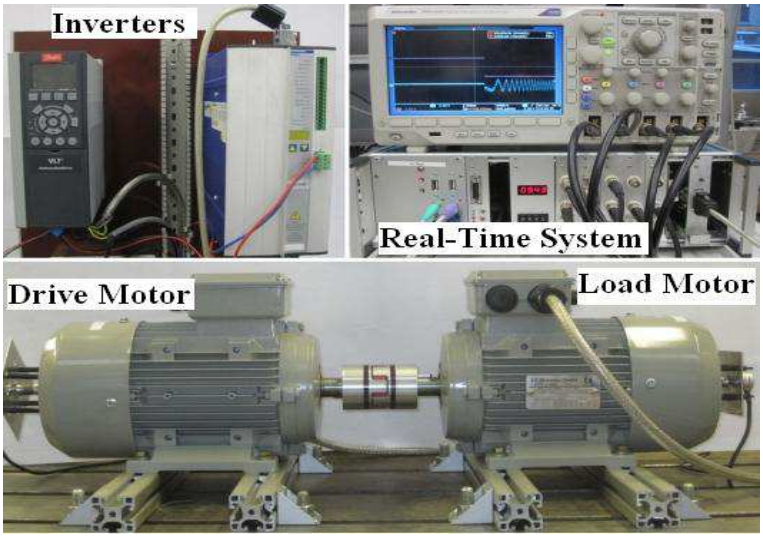

Figure B.1: Test bench description: IM system.

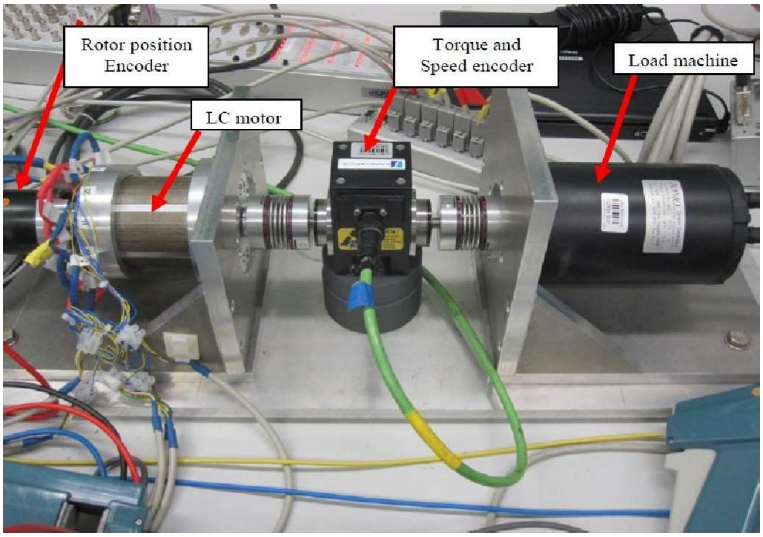

Figure B.2: Test bench description: IPMSM system.

APPENDIX C

Encoderless prediction model

To predict the stator current in synchronous reference (d-q reference), the forward Euler discretization is used:

$$\frac{dx}{dt} \approx \frac{x(k+1) - x(k)}{T_s}. \tag{C.1}$$

By considering the flux equations in d-q reference, the discretization model can be obtained:

$$\vec{\hat{i}}_s^r(k+1) = \frac{1}{L_s}(\vec{\hat{\psi}}_s^r(k+1) - L_m \cdot \vec{\hat{i}}_r^r(k+1)) \tag{C.2}$$

$$\vec{\hat{i}}_r^r(k+1) = \frac{1}{L_s \cdot L_r - L_m^2}(L_s \cdot \vec{\hat{\psi}}_r^r(k+1) - L_m \cdot \vec{\hat{\psi}}_s^r(k+1)) \tag{C.3}$$

By using (C.3) in (C.2)

$$\vec{\hat{i}}_s^r(k+1) = A \cdot \vec{\hat{\psi}}_s^r(k+1) - B \cdot \vec{\hat{\psi}}_r^r(k+1) \tag{C.4}$$

where $A = \frac{1}{L_s}(1 + \frac{L_m^2}{L_s \cdot L_r - L_m^2})$ and $B = \frac{L_m}{L_s \cdot L_r - L_m^2}$.

In d-q reference, the imaginary part of the rotor flux $\vec{\hat{\psi}}_{rq}^r(k+1)$ is zero. Thus the $\vec{\hat{i}}_s^r(k+1)$ on q axis can be described:

$$\vec{\hat{i}}_{sq}^r(k+1) = A \cdot \vec{\hat{\psi}}_{sq}^r(k+1) \tag{C.5}$$

To reach a predicted $\vec{\hat{i}}_s^r(k+1)$ on d axis, the relationship between rotor flux and stator flux is taken into account:

$$\vec{\hat{\psi}}^r_{rd}(k+1) = \frac{T_s \cdot L_m}{L_s \cdot \sigma}\vec{\hat{\psi}}^r_{sd}(k) - \frac{Ts}{\tau_r \cdot \sigma}\vec{\hat{\psi}}^r_{rd}(k) + \vec{\hat{\psi}}^r_{rd}(k) \tag{C.6}$$

With (C.4) and (C.6), the predicted $\vec{\hat{i}}^r_{sd}(k+1)$ can be calculated as:

$$\vec{\hat{i}}^r_{sd}(k+1) = A \cdot \vec{\hat{\psi}}^r_{sd}(k+1) - (B - C \cdot T_s) \cdot \vec{\hat{\psi}}^r_{rd}(k) - T_s \cdot D \cdot \vec{\hat{\psi}}^r_{sd}(k) \tag{C.7}$$

where $C = \dfrac{1}{\sigma \cdot \tau_r}$ and $D = B \cdot \dfrac{L_m}{\sigma \cdot L_s \cdot \tau_r}$.

APPENDIX D

Nomenclature

General electrical variables:

$i_{a,b,c}$	Phase currents
$i_{\alpha,\beta}$	Phase currents in stator reference frame
$i_{d,q}$	Phase currents in synchronous reference frame
J	Moment of inertia of the mechanical shaft
p	Pair of poles
$S_{a,b,c}$	Switching states of inverter
T_e	Electromagnetic torque
T_l	Load torque
$\boldsymbol{v}_{0,1,\ldots,7}$	Voltage vectors generated by a two-level inverter
V_{dc}	DC link voltage
$\boldsymbol{v}_s$	Stator voltage vector in stator reference frame
$v_{\alpha,\beta}$	Stator voltage in stator reference frame
$\boldsymbol{\psi}_s$	Stator flux vector in stator reference frame
$\boldsymbol{\psi}_r$	Rotorr flux vector in stator reference frame
ω_e	Electrical rotor speed
ω_m	Mechanical rotor speed

IPMSM parameters:

R_s	Stator resistance
ψ_{pm}	Flux magnitude of rotor permanent magnet
L_d	Mutual stator inductance in direct axis
L_q	Mutual rotor inductance in quadrature axis

IM parameters:

R_s	Stator resistance
R_r	Rotor resistance
L_m	Mutual inductance
L_s	Stator inductance
L_r	Rotor inductance
τ_r	Rotor time constant
σ	Leakage coefficient
k_s	Stator coupling factor
k_r	Rotor coupling factor
R_σ	Effective resistance of both windings
L_σ	Transient stator inductance
τ_σ	Transient time constant

Abbreviations

AC	Alternating current
DC	Direct current
DMTC	Direct mean torque control
DSP	Digital signal processing
DTC	Direct torque control
EFOSMO	Encoderless full order sliding mode observer
FCS-PTC	Finite control state-predictive torque control
FOC	Field oriented control
FPGAs	Field programmable gate arrays
GPC	Generalized predictive control
IM	Induction machine
IPMSM	Interior permanent magnet synchronous machine
LO	Luenberger observer
MPC	Model predictive control
MRAS	Model reference adaptive system
MTPA	Maximum torque per ampere
PCC	Predictive current control
PI	Proportional-integral
PSC	Predictive speed control
PWM	Pulse width modulation
SMO	Sliding mode observer
SVM	Space vector modulation
THD	Total harmonic distortion

Bibliography

[1] Hasse, *Control of Electrical Drives*. Berlin: Springer-Verlag, 1996.

[2] T. A. Lipo, *Vector control and dynamics of AC drives*. Oxford University Press, 1996, vol. 41.

[3] W. Leonhard, *Control of Electrical Drives*. Springer-Verlag New York, Inc., 1996.

[4] F. Blaschke, "The principle of field orientation as applied to the new transvector closed-loop control system for rotating machines," *Siemens Review*, vol. 39, no. 5, pp. 217–220, 1972.

[5] J. Holtz, "Pulsewidth modulation for electronic power conversion," *Proceedings of the IEEE*, vol. 82, no. 8, pp. 1194 –1214, aug 1994.

[6] M. Kazmierkowski, L. Franquelo, J. Rodriguez, M. Perez, and J. Leon, "High-performance motor drives," *Industrial Electronics Magazine, IEEE*, vol. 5, no. 3, pp. 6 –26, sept. 2011.

[7] I. Takahashi and T. Noguchi, "A new quick-response and high-efficiency control strategy of an induction motor," *Industry Applications, IEEE Transactions on*, vol. IA-22, no. 5, pp. 820 –827, sept. 1986.

[8] I. Takahashi and Y. Ohmori, "High-performance direct torque control of an induction motor," *Industry Applications, IEEE Transactions on*, vol. 25, no. 2, pp. 257 –264, mar/apr 1989.

[9] J.-K. Kang and S.-K. Sul, "New direct torque control of induction motor for minimum torque ripple and constant switching frequency," *Industry Applications, IEEE Transactions on*, vol. 35, no. 5, pp. 1076–1082, 1999.

[10] P. Mutschler and E. Flach, "Digital implementation of predictive direct control algorithms for induction motors," in *Industry Applications Conference, 1998. Thirty-Third IAS Annual Meeting. The 1998 IEEE*, vol. 1, 1998, pp. 444–451 vol.1.

[11] M. Pacas and J. Weber, "Predictive direct torque control for the pm synchronous machine," *Industrial Electronics, IEEE Transactions on*, vol. 52, no. 5, pp. 1350–1356, 2005.

[12] V. Ambrozic, G. Buja, and R. Menis, "Band-constrained technique for direct torque control of induction motor," *Industrial Electronics, IEEE Transactions on*, vol. 51, no. 4, pp. 776–784, 2004.

[13] C. Lascu, I. Boldea, and F. Blaabjerg, "Variable-structure direct torque control - a class of fast and robust controllers for induction machine drives," *Industrial Electronics, IEEE Transactions on*, vol. 51, no. 4, pp. 785–792, 2004.

[14] T. Habetler, F. Profumo, M. Pastorelli, and L. Tolbert, "Direct torque control of induction machines using space vector modulation," in *Industry Applications Society Annual Meeting, 1991., Conference Record of the 1991 IEEE*, 1991, pp. 428–436 vol.1.

[15] K.-B. Lee, F. Blaabjerg, and T.-W. Yoon, "Speed-sensorless dtc-svm for matrix converter drives with simple nonlinearity compensation," *Industry Applications, IEEE Transactions on*, vol. 43, no. 6, pp. 1639–1649, 2007.

[16] D. Stando and M. Kazmierkowski, "Novel speed sensorless dtc-svm scheme for induction motor drives," in *Compatibility and Power Electronics (CPE), 2013 8th International Conference on*, 2013, pp. 225–230.

[17] J. Beerten, J. Verveckken, and J. Driesen, "Predictive direct torque control for flux and torque ripple reduction," *Industrial Electronics, IEEE Transactions on*, vol. 57, no. 1, pp. 404 –412, jan. 2010.

[18] E. F. Camacho and C. Bordons, *Model Predictive Control*, Springer-Verlag, Ed., 2007.

[19] J. Maciejowski, *Predictive Control with Constraints*. Prentice-Hall, 2002.

[20] M. Morari and J. Lee, "Model Predictive Control: Past, present and future," *Computers & Chemical Engineering*, vol. 23, no. 4, pp. 667–682, 1999.

[21] M. Perez, M. Vasquez, J. Rodriguez, and J. Pontt, "Fpga-based predictive current control of a three-phase active front end rectifier," in *Industrial Technology, 2009. ICIT 2009. IEEE International Conference on*, 2009, pp. 1–6.

[22] C. Buccella, C. Cecati, and H. Latafat, "Digital control of power converters x2014;a survey," *Industrial Informatics, IEEE Transactions on*, vol. 8, no. 3, pp. 437–447, 2012.

[23] T. Atalik, M. Deniz, E. Koc, C. Gercek, B. Gultekin, M. Ermis, and I. Cadirci, "Multi-dsp and -fpga-based fully digital control system for cascaded multilevel converters used in facts applications," *Industrial Informatics, IEEE Transactions on*, vol. 8, no. 3, pp. 511–527, 2012.

[24] M. Kazmierkowski, M. Jasinski, and G. Wrona, "Dsp-based control of grid-connected power converters operating under grid distortions," *Industrial Informatics, IEEE Transactions on*, vol. 7, no. 2, pp. 204–211, 2011.

[25] J. Holtz and S. Stadtfeldt, "A predictive controller for the stator current vector of AC machines fed from a switched voltage source," in *Proc. IEEE Int. Power Electron. Conf. IPEC*, vol. 2, Mar. 27-31, 1983, pp. 1665–1675.

[26] R. Kennel and D. Schöder, "A predictive control strategy for converters," in *IFAC Control in Power Electronics and Electrical Drives*, 1983, pp. 415–422.

[27] J. Holtz, "Speed estimation and sensorless control of ac drives," in *Industrial Electronics, Control, and Instrumentation, 1993. Proceedings of the IECON '93., International Conference on*, nov 1993, pp. 649 –654 vol.2.

[28] D. Luenberger, "An introduction to observers," *Automatic Control, IEEE Transactions on*, vol. 16, no. 6, pp. 596–602, 1971.

[29] J. Holtz, "Sensorless control of induction machines:with or without signal injection?" *Industrial Electronics, IEEE Transactions on*, vol. 53, no. 1, pp. 7–30, 2005.

[30] K. Kubota, K. Matsuse, and T. Nakano, "Dsp-based speed adaptive flux observer of induction motor," *Industry Applications, IEEE Transactions on*, vol. 29, no. 2, pp. 344–348, 1993.

[31] C. Schauder, "Adaptive speed identification for vector control of induction motors without rotational transducers," *Industry Applications, IEEE Transactions on*, vol. 28, no. 5, pp. 1054 –1061, sep/oct 1992.

[32] Y.-R. Kim, S.-K. Sul, and M.-H. Park, "Speed sensorless vector control of induction motor using extended kalman filter," *Industry Applications, IEEE Transactions on*, vol. 30, no. 5, pp. 1225–1233, 1994.

[33] Z. Yan and V. Utkin, "Sliding mode observers for electric machines-an overview," in *IECON 02 [Industrial Electronics Society, IEEE 2002 28th Annual Conference of the]*, vol. 3, 2002, pp. 1842–1847 vol.3.

[34] J. Holtz, "The dynamic representation of AC drive systems by complex signal flow graphs," in *Industrial Electronics, 1994. Symposium Proceedings, ISIE '94., 1994 IEEE International Symposium on*, may 1994, pp. 1 –6.

[35] P. Cortes, M. Kazmierkowski, R. Kennel, D. Quevedo, and J. Rodriguez, "Predictive control in power electronics and drives," *Industrial Electronics, IEEE Transactions on*, vol. 55, no. 12, pp. 4312 –4324, dec. 2008.

[36] A. Linder, R. Kanchan, R. Kennel, and P. Stolze, *Model-based predictive control of electric drives*. Cuvillier, 2010.

[37] D. Clarke, "Application of generalized predictive control to industrial processes," *Control Systems Magazine, IEEE*, vol. 8, no. 2, pp. 49 –55, april 1988.

[38] R. Kennel, A. Linder, and M. Linke, "Generalized predictive control (GPC)-ready for use in drive applications?" in *Power Electronics Specialists Conference, 2001. PESC. 2001 IEEE 32nd Annual*, vol. 4, 2001, pp. 1839 –1844 vol. 4.

[39] S. Mariethoz, A. Domahidi, and M. Morari, "Sensorless explicit model predictive control of permanent magnet synchronous motors," in *Electric Machines and Drives Conference, 2009. IEMDC '09. IEEE International*, 2009, pp. 1250–1257.

[40] O. Kukrer, "Discrete-time current control of voltage-fed three-phase pwm inverters," *Power Electronics, IEEE Transactions on*, vol. 11, no. 2, pp. 260–269, 1996.

[41] H. Le-Huy, K. Slimani, and P. Viarouge, "Analysis and implementation of a real-time predictive current controller for permanent-magnet synchronous servo drives," *Industrial Electronics, IEEE Transactions on*, vol. 41, no. 1, pp. 110–117, 1994.

[42] H.-T. Moon, H.-S. Kim, and M.-J. Youn, "A discrete-time predictive current control for pmsm," *Power Electronics, IEEE Transactions on*, vol. 18, no. 1, pp. 464–472, 2003.

[43] H. Abu-Rub, J. Guzinski, Z. Krzeminski, and H. Toliyat, "Predictive current control of voltage-source inverters," *Industrial Electronics, IEEE Transactions on*, vol. 51, no. 3, pp. 585–593, 2004.

[44] S. Saggini, W. Stefanutti, E. Tedeschi, and P. Mattavelli, "Digital deadbeat control tuning for dc-dc converters using error correlation," *Power Electronics, IEEE Transactions on*, vol. 22, no. 4, pp. 1566–1570, 2007.

[45] T. Geyer, G. Papafotiou, and M. Morari, "Model predictive direct torque control x2014;part i: Concept, algorithm, and analysis," *Industrial Electronics, IEEE Transactions on*, vol. 56, no. 6, pp. 1894–1905, 2009.

[46] G. Papafotiou, J. Kley, K. Papadopoulos, P. Bohren, and M. Morari, "Model predictive direct torque control x2014;part ii: Implementation and experimental evaluation," *Industrial Electronics, IEEE Transactions on*, vol. 56, no. 6, pp. 1906–1915, 2009.

[47] M. Nemec, D. Nedeljkovic, and V. Ambrozic, "Predictive torque control of induction machines using immediate flux control," *Industrial Electronics, IEEE Transactions on*, vol. 54, no. 4, pp. 2009–2017, 2007.

[48] J. Rodriguez, J. Pontt, C. Silva, P. Cortés, U. Ammann, and S. Rees, "Predictive direct torque control of an induction machine," in *Proc. IEEE 11th Int. Power Electron. Motion Control Conf. EPE-PEMC*, Sep. 2-4,Riga, Latvia 2004.

[49] M. Preindl and S. Bolognani, "Model predictive direct torque control with finite control set for pmsm drive systems, part 1: Maximum torque per ampere operation," *Industrial Informatics, IEEE Transactions on*, vol. PP, no. 99, pp. 1–1, 2013.

[50] ——, "Model predictive direct torque control with finite control set for pmsm drive systems, part 2: Field weakening operation," *Industrial Informatics, IEEE Transactions on*, vol. 9, no. 2, pp. 648–657, 2013.

[51] S. Alireza Davari, D. Khaburi, and R. Kennel, "An improved fcs x2013;mpc algorithm for an induction motor with an imposed optimized weighting factor," *Power Electronics, IEEE Transactions on*, vol. 27, no. 3, pp. 1540–1551, 2012.

[52] C. Rojas, J. Rodriguez, F. Villarroel, J. Espinoza, C. Silva, and M. Trincado, "Predictive torque and flux control without weighting factors," *Industrial Electronics, IEEE Transactions on*, vol. PP, no. 99, p. 1, 2012.

[53] S. Alireza Davari, D. Khaburi, F. Wang, and R. Kennel, "Using full order and reduced order observers for robust sensorless predictive torque control of induction motors," *Power Electronics, IEEE Transactions on*, vol. 27, no. 7, pp. 3424–3433, 2012.

[54] M. Preindl and E. Schaltz, "Sensorless model predictive direct current control using novel second-order pll observer for pmsm drive systems," *Industrial Electronics, IEEE Transactions on*, vol. 58, no. 9, pp. 4087–4095, 2011.

[55] J. Guzinski and H. Abu-Rub, "Speed sensorless induction motor drive with predictive current controller," *Industrial Electronics, IEEE Transactions on*, vol. 60, no. 2, pp. 699–709, 2013.

[56] J. Rodriguez, J. Pontt, C. A. Silva, P. Correa, P. Lezana, P. Cortes, and U. Ammann, "Predictive current control of a voltage source inverter," *Industrial Electronics, IEEE Transactions on*, vol. 54, no. 1, pp. 495 –503, feb. 2007.

[57] T. Laczynski and A. Mertens, "Predictive stator current control for medium voltage drives with LC filters," *Power Electronics, IEEE Transactions on*, vol. 24, no. 11, pp. 2427 –2435, nov. 2009.

[58] P. Cortes ands, A. Wilson, S. Kouro, J. Rodriguez, and H. Abu-Rub, "Model predictive control of multilevel cascaded H-bridge inverters," *Industrial Electronics, IEEE Transactions on*, vol. 57, no. 8, pp. 2691 –2699, aug. 2010.

[59] F. Defay, A.-M. Llor, and M. Fadel, "Direct control strategy for a four-level three-phase flying-capacitor inverter," *Industrial Electronics, IEEE Transactions on*, vol. 57, no. 7, pp. 2240 –2248, july 2010.

[60] D. du Toit, H. Mouton, R. Kennel, and P. Stolze, "Predictive control of series stacked flying-capacitor active rectifiers," *Industrial Informatics, IEEE Transactions on*, vol. 9, no. 2, pp. 697–707, 2013.

[61] S. Muller, U. Ammann, and S. Rees, "New time-discrete modulation scheme for matrix converters," *Industrial Electronics, IEEE Transactions on*, vol. 52, no. 6, pp. 1607 – 1615, dec. 2005.

[62] R. Vargas, U. Ammann, B. Hudoffsky, J. Rodriguez, and P. Wheeler, "Predictive torque control of an induction machine fed by a matrix converter with reactive input power control," *Power Electronics, IEEE Transactions on*, vol. 25, no. 6, pp. 1426 –1438, june 2010.

[63] R. Vargas, U. Ammann, and J. Rodriguez, "Predictive approach to increase efficiency and reduce switching losses on matrix converters," *Power Electronics, IEEE Transactions on*, vol. 24, no. 4, pp. 894 –902, april 2009.

[64] P. Correa, J. Rodriguez, I. Lizama, and D. Andler, "A predictive control scheme for current-source rectifiers," *Industrial Electronics, IEEE Transactions on*, vol. 56, no. 5, pp. 1813 –1815, may 2009.

[65] M. Perez, J. Rodriguez, E. Fuentes, and F. Kammerer, "Predictive control of AC/AC modular multilevel converters," *Industrial Electronics, IEEE Transactions on*, vol. 59, no. 7, pp. 2832 –2839, july 2012.

[66] J. Riveros, F. Barrero, E. Levi, M. Duran, S. Toral, and M. Jones, "Variable-speed five-phase induction motor drive based on predictive torque control," *Industrial Electronics, IEEE Transactions on*, vol. 60, no. 8, pp. 2957–2968, 2013.

[67] F. Barrero, J. Prieto, E. Levi, R. Gregor, S. Toral, M. Duran, and M. Jones, "An enhanced predictive current control method for asymmetrical six-phase motor drives," *Industrial Electronics, IEEE Transactions on*, vol. 58, no. 8, pp. 3242–3252, 2011.

[68] P. Kakosimos and A. Kladas, "Implementation of photovoltaic array mppt through fixed step predictive control technique," *Renewable energy*, vol. 36, no. 9, pp. 2508–2514, 2011.

[69] S. Larrinaga, M. Vidal, E. Oyarbide, and J. Apraiz, "Predictive control strategy for DC/AC converters based on direct power control," *Industrial Electronics, IEEE Transactions on*, vol. 54, no. 3, pp. 1261 –1271, june 2007.

[70] H. Nakai, H. Ohtani, E. Satoh, and Y. Inaguma, "Development and testing of the torque control for the permanent-magnet synchronous motor," *Industrial Electronics, IEEE Transactions on*, vol. 52, no. 3, pp. 800–806, 2005.

[71] M. Preindl and S. Bolognani, "Model predictive direct speed control with finite control set of pmsm drive systems," *Power Electronics, IEEE Transactions on*, vol. 28, no. 2, pp. 1007–1015, 2013.

[72] M. Preindl, S. Bolognani, and C. Danielson, "Model predictive torque control with pwm using fast gradient method," in *Applied Power Electronics Conference and Exposition (APEC), 2013 Twenty-Eighth Annual IEEE*, 2013, pp. 2590–2597.

[73] J. Rodriguez, R. Kennel, J. Espinoza, M. Trincado, C. Silva, and C. Rojas, "High-performance control strategies for electrical drives: An experimental assessment," *Industrial Electronics, IEEE Transactions on*, vol. 59, no. 2, pp. 812 –820, feb. 2012.

[74] J. Rodriguez, J. Pontt, C. A. Silva, P. Correa, P. Lezana, P. Cortes, and U. Ammann, "Predictive current control of a voltage source inverter," *Industrial Electronics, IEEE Transactions on*, vol. 54, no. 1, pp. 495 –503, feb. 2007.

[75] E. Fuentes, C. Silva, and J. Yuz, "Predictive speed control of a two-mass system driven by a permanent magnet synchronous motor," *Industrial Electronics, IEEE Transactions on*, vol. 59, no. 7, pp. 2840–2848, 2012.

[76] M. Nemec, D. Nedeljkovic, and V. Ambrozic, "Predictive torque control of induction machines using immediate flux control," *Industrial Electronics, IEEE Transactions on*, vol. 54, no. 4, pp. 2009–2017, 2007.

[77] F. Wang, P. Stolze, R. Kennel, S. Davari, and D. Khaburi, "Speed-independent fcs-model predictive torque control for im based on smo," in *Power Electronics and Motion Control Conference (EPE/PEMC), 2012 15th International*, 2012, pp. LS7b–1.1–1–LS7b–1.1–5.

[78] T. Geyer, "Computationally efficient model predictive direct torque control," *Power Electronics, IEEE Transactions on*, vol. 26, no. 10, pp. 2804–2816, 2011.

[79] P. Stolze, M. Tomlinson, R. Kennel, and T. Mouton, "Heuristic finite-set model predictive current control for induction machines," in *ECCE Asia Downunder (ECCE Asia), 2013 IEEE*, 2013, pp. 1221–1226.

[80] M. Preindl, E. Schaltz, and P. Thogersen, "Switching frequency reduction using model predictive direct current control for high-power voltage source inverters," *Industrial Electronics, IEEE Transactions on*, vol. 58, no. 7, pp. 2826–2835, 2011.

[81] R. Lorenz, "The emerging role of dead-beat, direct torque and flux control in the future of induction machine drives," in *Optimization of Electrical and*

Electronic Equipment, 2008. OPTIM 2008. 11th International Conference on, 2008, pp. XIX–XXVII.

[82] J. Holtz and J. Quan, "Sensorless vector control of induction motors at very low speed using a nonlinear inverter model and parameter identification," *Industry Applications, IEEE Transactions on*, vol. 38, no. 4, pp. 1087 – 1095, jul/aug 2002.

[83] J. Maes and J. Melkebeek, "Speed-sensorless direct torque control of induction motors using an adaptive flux observer," *Industry Applications, IEEE Transactions on*, vol. 36, no. 3, pp. 778–785, 2000.

[84] N. Salvatore, A. Caponio, F. Neri, S. Stasi, and G. Cascella, "Optimization of delayed-state kalman-filter-based algorithm via differential evolution for sensorless control of induction motors," *Industrial Electronics, IEEE Transactions on*, vol. 57, no. 1, pp. 385–394, 2010.

[85] M. Cuibus, V. Bostan, S. Ambrosii, C. Ilas, and R. Magureanu, "Luenberger, kalman and neural network observers for sensorless induction motor control," in *Power Electronics and Motion Control Conference, 2000. Proceedings. IPEMC 2000. The Third International*, vol. 3, 2000, pp. 1256 –1261 vol.3.

[86] P. Liu, C.-Y. Hung, C.-S. Chiu, and K.-Y. Lian, "Sensorless linear induction motor speed tracking using fuzzy observers," *Electric Power Applications, IET*, vol. 5, no. 4, pp. 325 –334, april 2011.

[87] T. Ohtani, N. Takada, and K. Tanaka, "Vector control of induction motor without shaft encoder," *Industry Applications, IEEE Transactions on*, vol. 28, no. 1, pp. 157 –164, jan/feb 1992.

[88] M. Dybkowski and T. Orlowska-Kowalska, "Performance of the speed sensorless induction motor drive for traction application with mras type speed and flux estimator," in *Optimization of Electrical and Electronic Equipment (OPTIM), 2012 13th International Conference on*, may 2012, pp. 477 –481.

[89] F. Wang, P. Stolze, R. Kennel, S. Davari, and D. Khaburi, "Speed-independent fcs-model predictive torque control for im based on smo," in *Power Electronics and Motion Control Conference (EPE/PEMC), 2012 15th International*, 2012, pp. LS7b–1.1–1–LS7b–1.1–5.

[90] V. Vasic, S. Vukosavic, and E. Levi, "A stator resistance estimation scheme for speed sensorless rotor flux oriented induction motor drives," *Energy Conversion, IEEE Transactions on*, vol. 18, no. 4, pp. 476–483, 2003.

[91] C. Lascu, I. Boldea, and F. Blaabjerg, "Direct torque control of sensorless induction motor drives: a sliding-mode approach," *Industry Applications, IEEE Transactions on*, vol. 40, no. 2, pp. 582 – 590, march-april 2004.

[92] C. Lascu and G.-D. Andreescu, "Sliding-mode observer and improved integrator with dc-offset compensation for flux estimation in sensorless-controlled induction motors," *Industrial Electronics, IEEE Transactions on*, vol. 53, no. 3, pp. 785 – 794, june 2006.

[93] J. Rodriguez, R. Kennel, J. Espinoza, M. Trincado, C. Silva, and C. Rojas, "High-performance control strategies for electrical drives: An experimental assessment," *Industrial Electronics, IEEE Transactions on*, vol. 59, no. 2, pp. 812 –820, feb. 2012.

[94] J. Guzinski and H. Abu-Rub, "Speed sensorless induction motor drive with predictive current controller," *Industrial Electronics, IEEE Transactions on*, vol. 60, no. 2, pp. 699–709, 2013.

[95] H. Abu-Rub, J. GuzinÌski, J. Rodriguez, R. Kennel, and P. Cortes, "Predictive current controller for sensorless induction motor drive," in *Industrial Technology (ICIT), 2010 IEEE International Conference on*, 2010, pp. 1845–1850.

[96] Z. Xu and M. Rahman, "Comparison of a sliding observer and a kalman filter for direct-torque-controlled ipm synchronous motor drives," *Industrial Electronics, IEEE Transactions on*, vol. 59, no. 11, pp. 4179 –4188, nov. 2012.

[97] Z. Yan, C. Jin, and V. Utkin, "Sensorless sliding-mode control of induction motors," *Industrial Electronics, IEEE Transactions on*, vol. 47, no. 6, pp. 1286–1297, 2000.

[98] F. Wang, P. Stolze, R. Kennel, S. Alireza Davari, and D. Khaburi, "Inherent fcs-model predictive torque control for induction machine without encoder," in *Power Electronics, Electrical Drives, Automation and Motion (SPEEDAM), 2012 International Symposium on*, 2012, pp. 1069–1072.

[99] R. Kennel, J. Rodriguez, J. Espinoza, and M. Trincado, "High performance speed control methods for electrical machines: An assessment," in *Industrial Technology (ICIT), 2010 IEEE International Conference on*, march 2010, pp. 1793 –1799.

[100] F. Wang, Z. Zhang, A. Davari, R. Fotouhi, J. Rodriguez, and R. Kennel, "An encoderless predictive torque control for an induction machine with a revised prediction model and efosmo," *Industrial Electronics, IEEE Transactions on*, 2014,accepted.